2009

Optimization and characterization of lab-on-a-chip elements: Microfluidic chambers and microneedles

Puneet Khanna
University of South Florida

Optimization and Characterization of Lab-on-a-Chip Elements:

Microfluidic Chambers and Microneedles

by

Puneet Khanna

A dissertation submitted in partial fulfillment
of the requirements for the degree of
Doctor of Philosophy
Department of Electrical Engineering
College of Engineering
University of South Florida

Major Professor: Shekhar Bhansali, Ph.D.
Joel A. Strom, M.D.
Mark Jaroszeski, Ph.D.
Sanjukta Bhanja, Ph.D.
Andrew M. Hoff, Ph.D.

Date of Approval:
March 11, 2009

Keywords: Microfabrication, Bio-MEMS, MEMS, DRIE

DEDICATION

This dissertation is dedicated to my family who has patiently supported and encouraged me through this journey.

ACKNOWLEDGEMENTS

I would like to express my sincere gratitude to Dr. Shekhar Bhansali for providing me this wonderful opportunity to work in the Bio-MEMS and Microsystems laboratory. His encouragement, guidance, and direction during my entire stay at University of South Florida (USF) have been invaluable. In addition, his timely motivations have been vital to the success of this research. Next, I would like to thank Dr. Mark Jaroszeski and Dr. Joel A. Strom for co-advising on my research at various times. Their suggestions and critique were critical to the success of this work. Also, I thank Dr. Sanjuktha Bhanja and Dr. Andrew M. Hoff for serving on the defense committee. I really appreciate their time and consideration in reviewing my dissertation providing valuable feedback.

TABLE OF CONTENTS

LIST OF FIGURES

LIST OF TABLES

OPTIMIZATION AND CHARACTERIZATION OF LAB-ON-A-CHIP ELEMENTS: MICROFLUIDIC CHAMBERS AND MICRONEEDLES

Puneet Khanna

ABSTRACT

In this work, MEMS based fabrication is used to engineer multifaceted enhancements to microfluidic systems such as lab-on-a-chip devices. Two specific elements of microfluidic systems are the focus of this study: *microfluidic chambers* and *microneedles*. Microfluidic chambers, which are back-end passive elements, via proposed material and structural modifications, are shown to exhibit reduced non-specific DNA binding and enable increased cell lysis efficiency. Microneedles, which are front-end interfacing elements, have been fabricated in silicon and in silicon dioxide varieties. The geometry of silicon microneedles has been varied via DRIE processing to yield sharpened tips. Sharpening of microneedle tips provides reduced skin insertion force without compromising structural strength. Variation of skin insertion force of microneedles with change in tip sharpness has been studied, and toughness of human skin derived to be approximately 26 kJ/m^2. The axial and shear fracture limits of the microneedles have also been studied. Axial fracture of 36 gauge silicon needles takes place at an average force of 740gf. Shear fracture force of silicon needles varies from 275gf (33 gauge needles) to 35.6gf (36 gauge needles). Fracture limits of circular and square shaped silicon dioxide needles show reduced strength of square needles; which is pronounced in the case of shear fracture.

CHAPTER 1

INTRODUCTION

Recent advances in genetic and tissue engineering, molecular biology, biochemistry, embryology and cell biology have triggered a need for increased customization of ancillary technologies. Specifically, Bio-MEMS/micromachining technology is playing a proactive role in assisting explorations into uncharted research territory, and at the same time enabling the surge to miniaturize and mobilize established protocols. In this work, MEMS based fabrication is used to engineer multifaceted enhancements to microfluidic systems such as ‘Lab-on-a-chip’ (LOC) devices.

1.1 Lab-on-a-Chip Devices

A lab-on-a-chip (LOC) is a device that integrates one or several laboratory functions on a single chip that may be millimeters to a few square centimeters in size. These devices are capable of handling extremely small fluid volumes - down to less than picoliters. Lab-on-a-chip devices are a subset of Micro-Electro-Mechanical Systems (MEMS) devices and often also called "Micro Total Analysis Systems" (μTAS). However, the term ‘Lab-on-a-chip’ is more generic as these microfluidic systems are capable of performing much more than just analytical functions.

The first LOC analysis system was a gas chromatograph, developed in 1975 [1]. During the next two decades, LOC research started to gain ground as scientists developed concepts for microfluidic systems [2, 3]. Specific functional elements such as flow sensors [4, 5], micro-pumps [6, 7] and micro-valves [8, 9] were developed.

Researchers started to construct highly integrated compact devices. Systems demonstrated the inclusion of pre-treatment steps, usually done at lab-scale, thus elevating their utility from simple sensory functions to complete laboratory analysis.

These devices have a wide range of applications. Chemists are using such tools to synthesize new molecules and materials (rapid screening [10, 11], microreactors for pharmaceutics [12]), and biologists are using them to study complex cellular processes (e.g. biochemical analysis [13, 14], environmental monitoring [15, 16], medical diagnostics [17, 18], cellomics [19, 20]). LOC devices are slowly becoming enabling devices for research in fields such as genomics [21], proteomics [22], pharmacogenomics [23] etc. These systems can offer point-of-care diagnostic abilities [24, 25] that could revolutionize medicine.

The ability to perform laboratory operations on a small scale using miniaturized devices is highly attractive [26]. Small volumes reduce the time taken to synthesize or analyze a product. The unique behavior of liquids at the microscale allows greater control of molecular concentrations and interactions. Reagent costs and the amount of chemical waste can be much reduced. The compact size of units is a benefit in itself; increasing deployment possibilities. Samples can be analyzed at the point of need rather than a centralized laboratory. Massive parallelization due to compactness, allows high-throughput analysis. Also they offer a safer platform for chemical, radioactive or biological studies because of integration of functionality and smaller fluid volumes/stored energies. Furthermore, benefits typical to MEMS systems also apply to these devices, i.e. they have low fabrication and disposal costs, and are conducive to mass production.

1.2 Elements of Lab-on-a-Chip System

A typical LOC system contains multiple elements, active or passive. The incorporation of most elements is application dependent, though some passive elements

are almost always required. Active elements may be micropumps [6, 7], microvalves [8, 9], heaters [27, 28], micro-sonicators [29], flow sensors [13, 14] among various others. Passive elements may be microfluidic chambers [30-32], microfluidic channels [33, 34] or other external interface elements.

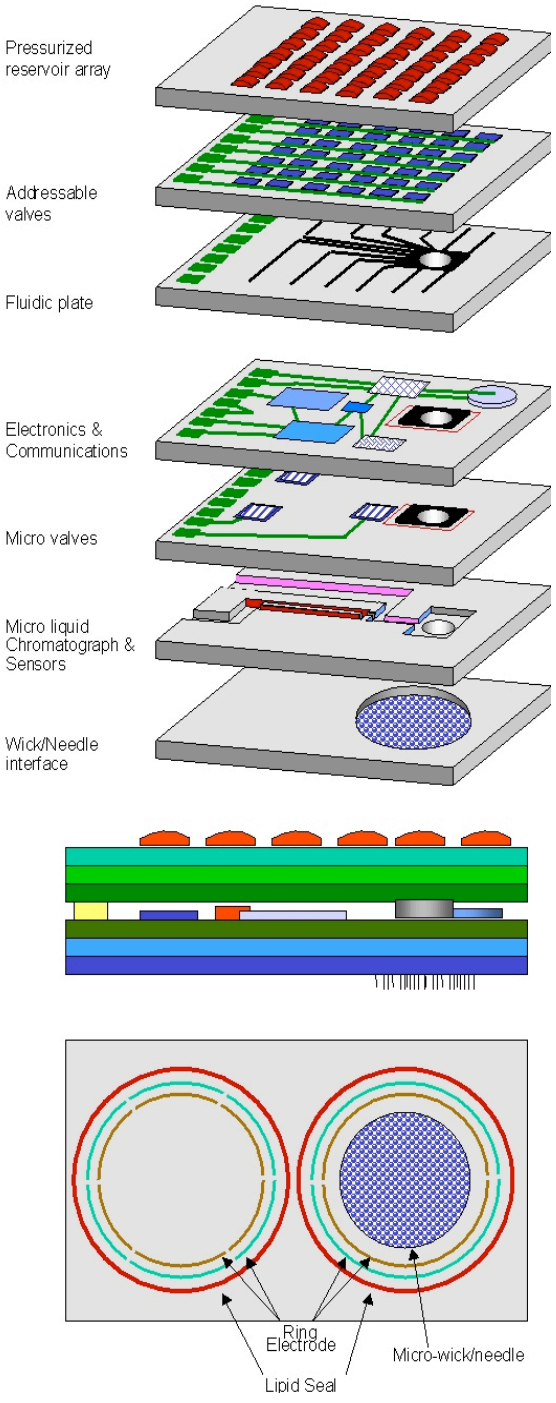

Figure 1: Sketch of a prototypical LOC system [35]

Figure 1 shows a sketch of a typical LOC system. The system depicted consists of multi-level functional layers integrated together. The development of such a system is usually highly complex. There are numerous parametric dependencies at each design level. An efficient system level layout and effective integration protocol is crucial, and so is design optimization of each constituent element. Every element of the system needs to be design as per the specific application requirements. Enhancement of any particular element can lead to profound gains in various output specifications.

1.3 Systems for Biofluid Transport and Manipulation

In this research, LOC systems that specifically transport analytes through skin and manipulate biofluids have been investigated. Examples of such systems include LOC's for heath monitoring or disease detection via biomarker analysis [36, 37], DNA extraction [38, 39] etc. Different LOC systems might need to interact with skin directly to perform varying tasks, such as, extract analytes, deliver therapeutic entities or extract physiological signals. For example, an LOC might be a system for medical diagnosis; analyzing biological entities, such as blood [40-42], extracted through skin. Other possible applications may be recording and analysis of bioimpedance [43-45], or drug delivery [46, 47]. Such devices would employ an external biotic interface. The specific type and design of the interface would application dependant. They may be active elements (microelectrodes for electroporation) or passive elements (microneedles for biofluid extraction). Such systems promise to bridge the biotic (organism/skin) and abiotic (environment) realms in unanticipated ways.

Currently accepted approaches to collect samples through skin include disruption in skin structure through needle puncture, removal of the stratum corneum through gels [48] or tapes [49, 50], or laser ablation followed by vacuum assisted extraction [51]. Micromachined electrodes and needles (microelectrodes or microneedles) can enable

collection of the same information, with significantly less trauma to the tissue, and have the potential of even eliminating it [52, 53].

The microneedles, when incorporated into the LOC, will enable the development of a generic front end to the micro-system. Such an interface can take care of most applications involving skin interaction, whether diagnostic or therapeutic in nature. The LOC sub-systems can be broadly classified by the type of entity transferred: physical (fluid transfer) or electrical (charge transfer), and the system may incorporate any or both types of interactions.

The LOC system may be either a stand-alone diagnostic or therapeutic system, or have both capabilities. An active feedback controlled system in which the therapy depends upon the diagnosis constitutes a 'smart' system. The data collected may either be used locally or be relayed further; in which case the system would incorporate an on-board data communication capability; to transmit raw or significant data. Advanced sensor systems would follow a node-based approach for a global level monitoring. They shall include low power wireless communication protocols within multiple nodes, distributed computing algorithms and protocols at these nodes.

The MEMS devices that interact with the skin would depend upon the application and will generally be microfluidics based (for fluid transfer systems), or IC based (for charge transfer systems). Fluid transfer systems can be expected to be more complex and will have multiple component levels.

1.4 Lab-on-a-Chip Elements Under Investigation

This research aims to enhance the state of the art of LOC systems via optimization and characterization of specific constituent elements. The first element is the microfluidic chamber, which forms the most prevalent back-end element of a LOC system. There are multiple design considerations that go into optimizing the microfluidic

chamber, such as material, functional and architectural. Common variables might be: compatibility of building material with the application; deployment scenarios; number of chambers required for desired reliability; type of fluid being handled (blood, ISF, suspension of cells, specific chemical); etc.

The second specific element that has been studied is a typical external interface – microneedles. As the term implies, these are similar to regular hypodermic needles, except that they are much smaller. In the case of microneedle design all the material, functional and architectural considerations that were there for microfluidic chambers still apply. But there get added many more parametric interdependencies; the geometry of the individual needle, the structural strength of the needles, biocompatibility, toughness of the biotic layer being punctured, etc.

1.5 Manipulation of Biofluids in Lab-on-a-Chip Systems

Most LOC systems need to handle biofluids within microfluidic chambers. Typically these chambers have no functionality other than being passive containers. However, even this task needs careful design of the element. Material, functional and architectural considerations exist. A major issue while handling biological fluidics is biocompatibility.

'Biocompatibility' requirements vary as per specific applications. Generally, the microfluidic chamber material should act as an appropriate host to the biological entities for the application. There should not be any toxic or detrimental effects on the biofluids, that might affect system efficiency. Continuous research is required to gain insight into how biomaterials interact with the chamber body and eventually how those interactions determine the success of the LOC device.

1.6 Interfacing Lab-on-a-chip Systems With Skin

The iterative development of noninvasive, bio-engineered lab-on-a-chip systems should not ignore the body's own exquisite material solution to biotic/abiotic interface design. Seamless coupling to the body surface requires a better understanding of the molecular architecture of the SC as a polymer film and the functional unit organization of the epidermis. This challenge amounts to nothing less than a beginning understanding of the boundary conditions of the human body. This will necessitate integration of broad advances in a wide variety of fields viz. microsystems, clinical medicine, cell and molecular biology, and information technology. Such extended interface systems would be typically freestanding, multifunctional, multimode, microfluidics-based sensor systems coupled to human skin for real time monitoring at global (physiological) and local (molecular) levels.

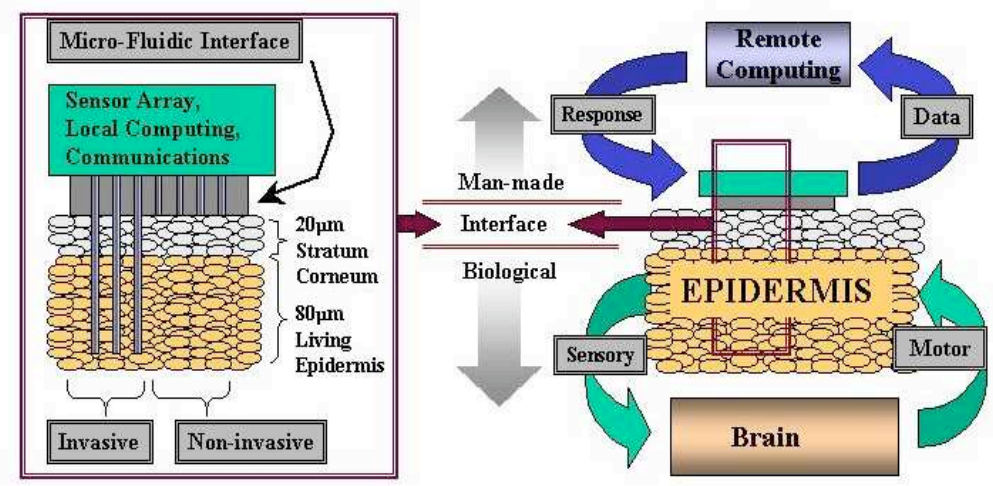

Figure 2: Bioengineered interface between analogous biological and LOC systems *[35]*

The scope of systems containing bio-engineered micro-interfaces goes beyond sampling and extraction of high-quality distributed physiological data. Advanced systems hold the potential to incorporate both diagnostic as well as therapeutic functionality.

Such systems would utilize information in the same manner as the body uses the skin surface for sensorimotor feedback control [54-60].

Development of bio-engineered skin-interfacing LOC systems require interdisciplinary research combining such diverse fields as tissue engineering, molecular biology, anatomy, physiology, medical physics, biology, mechanical engineering, microfluidics, chemical processes, microfabrication, nanotechnology, and signal processing.

When a foreign object is introduced in the body, the body rejects it by forming scar tissue around it, thus isolating it from the rest of the body. An interface between the sensing system and the skin needs to 'ensure that the body does not initiate this defense mechanism. Such ability would make it possible for the interface material to act as a seamless bridge that performs transfer of signals and samples to the sensing system. Systems with such interfaces would have the potential to integrate detection, diagnostics, and treatment of adverse medical and physiological states affecting the human body. An example of major drivers for such systems is diabetes. There are numerous active efforts underway to develop a seamless glucose sensing and insulin delivery systems that can function over extended durations. Other systems could enable diagnosis of adverse states like heat prostration, exhaustion, dehydration, hemorrhagic shock, and anxiety. This approach can potentially result in physiologically and clinically relevant information far in advance of changes in central measures like blood pressure, arterial blood gases or acid-base status.

Positioning sensors strategically on the body surface and incorporating developments in Computer Science and Engineering viz distributed computing algorithms, and low power wireless communication, can allow observation of the target biological processes in the body in real time, similar to electrocardiography and electroencephalography. Essentially, the bio-engineered interfaces will facilitate (a)

characterization of the quantitative boundary conditions of the human body; (b) determination of variation of those conditions with disease and environmental change, and; (c) putting into effect suitable therapeutic response, as needed.

1.7 Anatomy of Skin

The research entails focus on the unique biological boundary of the body manifested by the surface of the human skin. Specifically, attention is drawn to the outermost layer of the skin, the stratum corneum (SC), which, as the terminally differentiated (dead) product of epidermal differentiation forms the ultimate biopolymeric interface with the environment. The SC, viewed through the lens of a materials engineer, is a multifunctional nanocomposite with all the hallmarks of a smart material. The strategic location of this highly organized, thin (~20 μ), bioengineered film place it in an optimal location to mediate biotic/abiotic interactions. Improved sensor systems for noninvasive detection of physiologically relevant mechanical, electrical, or magnetic signatures at the surface of the body (data beyond current electrocardiography or electroencephalography) require bridging to the body via this complex but assessable biological structure.

To develop a long lasting interface, the nuances involved in interfacing with skin, need to be understood. Towards that goal, a brief review of the skin is provided hereunder.

1.7.1 General Structure

Skin is the largest organ of the human body and accounts for approximately 16% of the body weight. It serves multiple purposes which can be broadly classified into four functions – 1) Protection: physical, biological, against UV light, from dehydration; 2) Thermoregulation: control of body temperature 3) Metabolic functions: synthesis of

vitamin D, excretion of waste products, storage of fat; 4) Sensory functions: pressure, heat, cold, contact, pain, as well as integral interaction with vision (pigmentation patterns) and smell (pheromone release). It is evident from its range of functionality that the skin hosts complex physiological, biomechanical and biochemical processes, all occurring simultaneously.

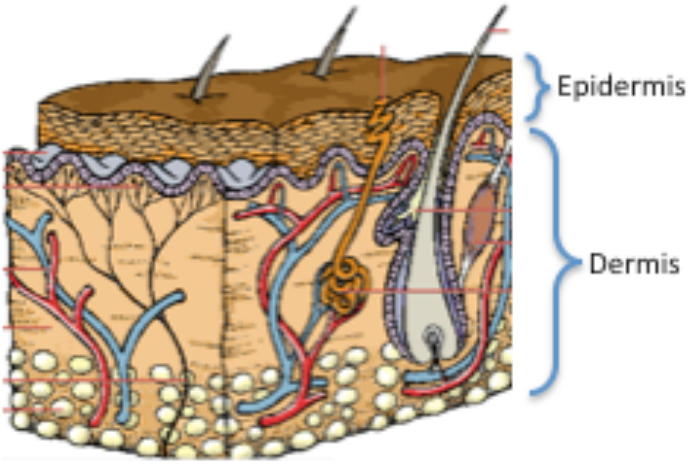

Figure 3: Cross-section of skin [61]

The skin possesses a layered structure comprising of various kinds of tissues. It has two layers, the dermis and the epidermis. The epidermis is the outer layer of the skin. Being a tough and waterproof layer, it protects the inner regions. The underlying dermis is a thicker layer and is responsible for imparting strength and elasticity to the skin. Beneath the dermis is the subcutaneous layer, which is not part of the skin itself. It is a layer of tissue made of protein fibers and adipose tissue (fat). It contains glands, sensory receptors and other skin structures.

The protection provided by the epidermis forms the first barrier against harmful foreign substances. Most of the cells (approximately 90%) in the epidermis are “keratinocytes”. They produce a tough, fibrous, intracellular protein called keratin; hence the name. The keratinocytes are stacked in layers. The youngest cells occupy the lower

layers while older cells are present in the upper ones. The lower layer cells multiply continually, while the older upper layer keratinocytes constantly slough off. By the time the cells move up to the uppermost layer of the epidermis, they are dead and completely filled with the keratin. From bottom to top the layers are named stratum basale, stratum spinosum, stratum granulosum, and stratum corneum.

Figure 4: Cross-section of epidermis [62]

Various skin properties are routinely measured at the broadest classification level whereby considering the entire epidermis as a single functional entity. Such information, though essential, is incomprehensive in that it does not account for the heterogeneity of the epidermis. It is imperative to possess precise knowledge of the distinct properties of each cutaneous component to design interfaces that interact individually with the cuticle layers. The stratum corneum in particular dominates various design considerations and is often times the principal cause for development of micromachined interfaces.

1.7.2 Stratum Corneum

The outermost layer of the epidermis, the stratum corneum (SC), is a thin, flexible, high impedance biopolymer composed of interconnected ‘dead’ cells called

corneocytes. This complexly organized, anucleate, 15-20 μm thick, biopolymeric structure is essential to life and serves to couple the organism to the environment. This structure is particularly well developed in humans who lack a protective mantle of fur. It is the major barrier to all environmental insults (climatic, toxic from xenobiotics or microbial) [63]. Despite its resilience it can bind a certain amount of water to stay soft, smooth and pliable even in a dry environment, thus allowing free body movement without cracking or scaling of the skin surface.

The underlying hypothesis in the development of bio-engineered systems is that the stratum corneum can be a portal to the biological and physiological processes. It plays a major role in modulating sensory signals for visual and tactile perception. Also, the hydration status of the stratum corneum is a key determinant of the mechanical, electrical, optical, and chemical properties of the skin. The properties of this layer serve as a health status indicator and valuable insights into the human biosystem can be attained by characterizing the quantitative boundary conditions of the human body and determining variation of those conditions with disease and environmental change.

As a secondary consideration, the condition of this layer serves vital social and cultural functions as it is a major determinant of our appearance and is thus of central interest to the cosmetic industry. The multifaceted significance of the stratum corneum necessitates a multidisciplinary approach towards its analyses. Current researchers include dermatologists, cosmetic scientists, physiologists, neonatologists, pharmaceutical scientists and bioengineers.

1.8 Designing a Lab-on-a-Chip System

Despite architectural differences, the tasks involved in designing the LOC systems have certain standard objectives. These objectives establish the foundation of knowledge and capabilities required to build the specific system. They include: (a)

understanding the cellular and molecular biology of the biofluid being handled; and (b) developing tools, techniques and protocols to non-intrusively or semi-intrusively collect relevant physiological information using an array of micro/nano probes, sensors and analysis protocols. For a global level system it includes: (c) using distributed computing, imaging and wireless communication to analyze, correlate and understand the response of the skin at various body sites to a single controlled stimulus and across a group of sensors at a population level. Fluid transfer systems entail: (d) developing models to understand microfluidic coupling between the stratum corneum and MEMS-based tools and on-chip immunoassays and sensors. Therapeutic systems include: (e) developing therapeutic application methodologies and protocols to deliver required medication based upon computational algorithms.

Each of the objectives mentioned above encompasses numerous tasks, which involve of varied undertakings in biology, medicine, chemistry, information technology and microtechnology. The first task includes interface testing on various microfluidic chamber surfaces. Relevant target measurements on skin such as bio-impedance, immunoassay and analyte detection would have to be conducted. This would assist in identifying key analytes to be monitored, and determining the baseline and deviation standards. Information/models and images would be used to enable extrapolation of data from the tissue level microenvironment, to an understanding of meaningful physiological responses at the level of the organism. For reagent analysis systems, immunoassays and analyte detection protocols have to be developed. Sensor/analyzer designs have to be built accordingly by the MEMS designers. Deciding upon the physical design and establishing fabrication procedures of the individual LOC elements would form the most vital component of system development. The biggest challenge would lie in integration of the various microdevices (such as the passive microfluidic components, sensors, active elements etc.). To ease the development process, the LOC

systems can be expected to have a modular design, i.e. each sub-system would be functionally independent. However sub-system development cannot be independent of other tasks and continuous collaboration between MEMS and biotechnology/information technology groups would have to be a standard feature of the design process.

If an LOC is expected to be autonomous, the information technology tasks could include development of data processing capability and a data transfer interface. Depending upon whether the LOC unit is a stand-alone node or part of a global sensing system, the tasks would include creation of low power wireless communication protocols within multiple nodes, distributed computing algorithms and protocols at these nodes, and transmission of raw or significant data collected from individual nodes. Data management tasks would comprise of signal conditioning, post processing, sensor fusion, and feedback control to manage and optimize the device/skin interface. Data depiction front-ends would have to be created to facilitate easier data interpretation, e.g. providing the data as a 3-D image composite.

1.9 Designing the Lab-on-a-Chip Elements

Element design is a critical part of designing an LOC system. It involves simultaneous consideration of multiple parameters. There is always present some form of trade-off. In case of microfluidic chambers, an example would be non-specific DNA binding vs. ease of fabrication, life span vs. ease of integration etc. For microneedles, such considerations would be ease of skin penetration vs. ease of fluid flow, probe strength vs. biocompatibility etc. There is no specific optimum design; it varies with each application. The combinatorial possibilities are vast and the parametric interdependency highly complex. Every application will have a few structural or functional demands that bear higher priority than others. Fortunately, not every application needs a new needle design. Most applications can be grouped into classes having broadly similar

requirements. Thus generic element arrays can be designed with specifications that provide enough latitude for parametric variations within the class.

1.9.1 Functional Requirements of Microfluidic Chambers

Interface elements in LOC devices have to satisfy diverse functional requirements. Microfluidic chambers don't have to usually satisfy strict mechanical requirements. Their most significant requirement is biocompatibility with the biofluids. Non-specific binding is an inherent problem. Biological entities adhere to surfaces that they are not supposed to, and detach when not supposed to. Thus non-specific binding may interfere with the obtained output, and reduces the overall sensitivity. Efficient cleaning of the microfludic chamber suddenly becomes a top priority is many times not a trivial task.

1.9.2 Functional Requirements of Microneedles

In the case of microneedles, a large majority of requirements are mechanical in nature. Bioengineered interfacing entails insertion of microneedles into the upper epidermal layers of the skin, and thus the probes have to be able to withstand the applied pressure and puncture the skin without fracture. Optimum design demands characterization of various mechanical features such as mechanical strength, buckling characteristics, fracture point, elasticity, angular strength, ease of penetration etc. Microneedles have to be further characterized for their capability to withstand fluidic pressure at the sidewalls and the inlet pressure for a particular flow rate.

. This requirement is imposed on the needles too, with regards to their interaction with skin. Interaction of non-biocompatible needles with cells and tissue is known to trigger "foreign body response" and cause bio-fouling. Biologically, such a system constitutes a breach in the integrity of the organism and would be responded to as a wound. Thus it becomes difficult to determine whether one is sampling "intracellular" fluid from impaled cells or "extracellular" fluid from needles placed between cells. The

most common approach to minimize biofouling is surface passivation of the functional materials.

Microfluidic properties of microneedles are also important design factors. The design has to take into account fluid flow characteristics for the passing fluid and also environmental flow resistance. There should be no clogging of the fluid at orifices or along the needle lumens. Also capillary forces have to be sufficient to ensure fluid delivery or extraction.

Other common parameters affecting microneedle design include adhesive interactions (adhesion of analytes to the needle), life duration, chemical inertness and biodegradability.

1.10 Design Variables for Lab-on-a-Chip Elements

Common variables that control the component characteristics can be broadly classified into: 1) Material selection 2) Geometric considerations 3) Array layout

1.10.1 Material Selection

There is no one best material available for the fabrication of microfluidic chambers or needles. The choice varies according to the application.

In the case of microfluidic chambers, polymers such as polydimethyl siloxane (PDMS) [64], polymethyl methacrylate (PMMA) [65] are highly popular due to their ease of fabrication. Plastics derivatives like polycarbonate [66] and cyclic olefin copolymers [24] are also popular due to the cost benefits.

Metallic needles [67-69] are popular due to strength and biocompatibility; they have lowest probability of causing allergic reactions. However, the minimum size of needles possible is relatively large. They are relatively easy to fabricate; common

methods being micromolding or electroforming, Stainless steel is used quite often due to its high strength, non-corrosive nature and low price.

Non-metallic materials have other advantages. Glass microneedles [70] provide ease of fabrication while silicon dioxide microneedles [71, 72] offer good biocompatibility characteristics. Polymer microneedles [73-75] are of interest since they are biodegradable. These microneedles can be used without danger of infection due to needle tips breaking off. Conductive polymers are often used for microelectrodes due to their selective interaction properties with proteins, enzymes and antibodies thus making them ideal for certain biochemical sensing applications. Furthermore, polymers are highly flexible too. The most common and prevalent material for microneedles is silicon due to high strength, design flexibility and ease of fabrication [76-79].

1.10.2 Geometrical Considerations

Geometric considerations for microfluidic chambers are dependent upon the fluid being handled, its viscosity, Reynolds number and Newtonian characteristics among other things. The specific application and the employed protocol determine the size and arrangement of the chambers.

Geometry of the microprobe affects most of the electrical, mechanical or other characteristics highlighted earlier. Common geometrical considerations are needle length, width, area/perimeter of cross-section, shape, thickness of sidewalls, tip geometry, taper angle, etc.

Each geometrical variable can affect a number of parameters and thus the optimum choice of geometry is often a trade-off between efficiencies. For example, sharper needle tips can be expected to require less force for insertion, but the reduced penetration force comes at the expense of reduced strength near the tip [80].

Needle length determination is particularly critical as the needles must be sufficiently deep to allow reliable test results, and for drug delivery or sample extraction, they have to reach the blood capillaries. The possibility of fracture and buckling increase as probe length increases. Also, in order to be painless, the needles cannot be so long as to touch the nerve endings. Increasing cross-sectional area increases strength but may compromise certain insertion force into skin. Constriction of needle lumen size is limited by the size of species being transferred. Finally, biofouling properties always impose critical constraints, it being less intensive for less invasive geometries.

Microneedle are most often used in an array formation. Thus device functionality depends upon the not only on their individual, but also on their 'team' efficiency. Array size, density and configuration are most important considerations. A very closely packed array can cause unsuccessful penetration due to 'bed of nails' effect [81].

1.11 Technological Merit of Skin Interface Elements

Micromachined needles form the technological foundation for bio-engineered skin interfaces for the LOC devices. The physical characteristics of microneedles provide unique technological advantages to these systems as compared to traditional invasive methodologies. Next generation therapeutic methods using advances in genomics, proteomics, pharmacogenomics etc., have all come into existence due to the capabilities provided by these micro-components.

Tissue interaction is usually done using macroscale components such as hypodermic needles (henceforth referred to as macroneedles). Such components offer immense utilitarian advantages in their being easy to fabricate and handle. They are irreplaceable in appropriate problem identification and drug delivery applications that warrant the use of large sized interface tools. However with the advent new technologies

and discoveries, these conventional tools are being fast replaced with their micromachined counterparts.

1.11.1 Benefits From Microneedles

In typical clinical and biomedical applications, drug injection or biofluid sampling is done using hypodermic needles. Though utilitarian, this method causes undesirable pain and excessive tissue trauma. This is particularly troublesome when frequent administration of drugs is necessary (such as administration of insulin). Furthermore, control of drug delivery is highly approximate using macroneedles.

A painless alternative to macroneedles, which has lately started to become popular, is the transdermal patch. It is simply a piece of plastic with an adhesive on it with the drug being suspended in the adhesive. The patch is stuck on the skin and the drug passively diffuses slowly to lower layers. However, this method of drug delivery poses certain challenges. The effectiveness of the adhesive is directly affected by the concentration of the drug within the adhesive. Thus, if a larger dose of the drug is required, either it has to be reapplied more frequently or a larger patch has to be used. Increasing the concentration of the drug does not help if the adhesive bond with the skin is weak [82]. Furthermore, it is a slow method and not very precise, and is thus not suitable to many applications. The barrier properties of the stratum corneum pose unique obstacles to drug application by providing for a very low topical bioavailability [83]. The “route” taken by the externally applied drug is tortuous – around the dead, dense corneocytes. The permeant diffuses in the intercellular channels, which contain structured lipid bilayers. Thus the problem is compounded, as molecules have to cross, sequentially, lipophilic and hydrophilic domains.

Microneedles are increasingly being sought out as an alternative to the macroneedle and the transdermal patch as it combines their advantages while

eliminating the disadvantages of both. In recent times, numerous types of micro needles have been fabricated and used for transdermal drug delivery [84-88], vaccine delivery [89], fluid analysis and sampling [90], dialysis [91] and cellular DNA delivery [92] among other applications.

Vital technological advantages obtained by using microneedles are:

1.11.1.1 Increased Permeability

The self-sealing properties of the stratum corneum are poorly understood. It is probable that the stratum corneum seals holes spontaneously up to a given magnitude, but beyond that limit it cannot close itself. This property can be used by microneedles to increase the permeability of skin by orders of magnitude, making it is possible to diffuse macromolecules across the skin. Thus in some cases, the microneedles may not themselves deliver the drug. Unmedicated microneedles may simply puncture the skin and then medicines may be smeared on and left to be rapidly absorbed through the holes.

1.11.1.2 Application Customization

Microneedles can be fabricated in various shapes (cylindrical, pyramidal, polyhedral, etc.) or sizes and may be hollow or solid. Such geometrical flexibility allows for fabrication of microneedle arrays customized for the type and volume of drug and the duration of use. This feature also translates to flexibility in method of drug delivery. For example, medicines may be delivered the way a regular hypodermic needle does so, or microneedles may be coated with medication which would be absorbed on contact.

1.11.1.3 Material Flexibility

Microneedles can be fabricated using a variety of materials such as silicon, glass, carbon nanotubes, biodegradable polymers, and metals. The choice of material would

depend on the application. For example, metallic microneedles are the most popular because they have high strength and biocompatibility. Polymer needles have the advantage of being biodegradable and thus if the tips snap off during insertion, the body would simply absorb the remains.

1.11.1.4 Minimal Medical Training Requirements

Microneedles are expected to become a boon for immunization programs in developing countries as they could be applied by people with minimal medical training. Drugs could similarly be administered at home instead of presently compulsory clinical visits. The significance of such capability is further enhanced due to possibility of mass vaccination or antidote administration in bioterrorism incidents. The cause is further helped by the fact that microneedle fabrication promises to be less expensive than any other reported technology.

1.11.1.5 Site Specific Therapy

Highly targeted drug administration to individual cells is possible using microneedles. A potential application is to modulate the immune system by administering drugs precisely into the area where special immune cells reside. Langerhans cells, for example, are the major immunomodulatory cells which modify delivery of HIV particles from the epidermis to the lymph nodes - these cells are located only 40-50 microns deep in the epidermis. Vaccine delivery directly to these cells provides a target of mass vaccination strategies.

1.11.1.6 Precise Control of Drug Quantities

The small volumes of drug passing through the microneedles, either through diffusion or through auxiliary pumping systems make the delivery process highly controllable.

Microneedles are presently at various stages of development though they are yet to be introduced clinically. They will surely revolutionize drug delivery systems and

provide more options and possibilities to patients. The day is not far when administering of polypeptides and even proteins will not be via injection or infusion.

1.12 Microneedle Design for Autonomous Therapy Systems

As mentioned earlier, an application-independent optimum design for microneedles does not exist. Design selection is highly application specific and involves simultaneous consideration of multiple parameters. Common design variables include geometric features (length, diameter, shape), choice of material, array layout, physical architecture (beveled tip, conical, side-opened) etc. There is always a trade-off among the various output characteristics such as fragility, biocompatibility, penetration force, fluid flow rates, ease of fabrication, cost etc. Application specific requirements of diabetes therapy systems necessitate that certain microneedle characteristics have higher priority. Key design issues and related parametric interdependencies specific to diabetes therapy systems are discussed below.

1.12.1 Microneedles for the Sensing Component

Glucose sensing can be done by sampling either blood or interstitial fluid (ISF). The choice of the biofluid sampled is the primary factor determining microneedle design. In order to understand design variations between blood extracting microneedles and ISF extracting microneedles, it is important to understand physiological differences between blood and ISF.

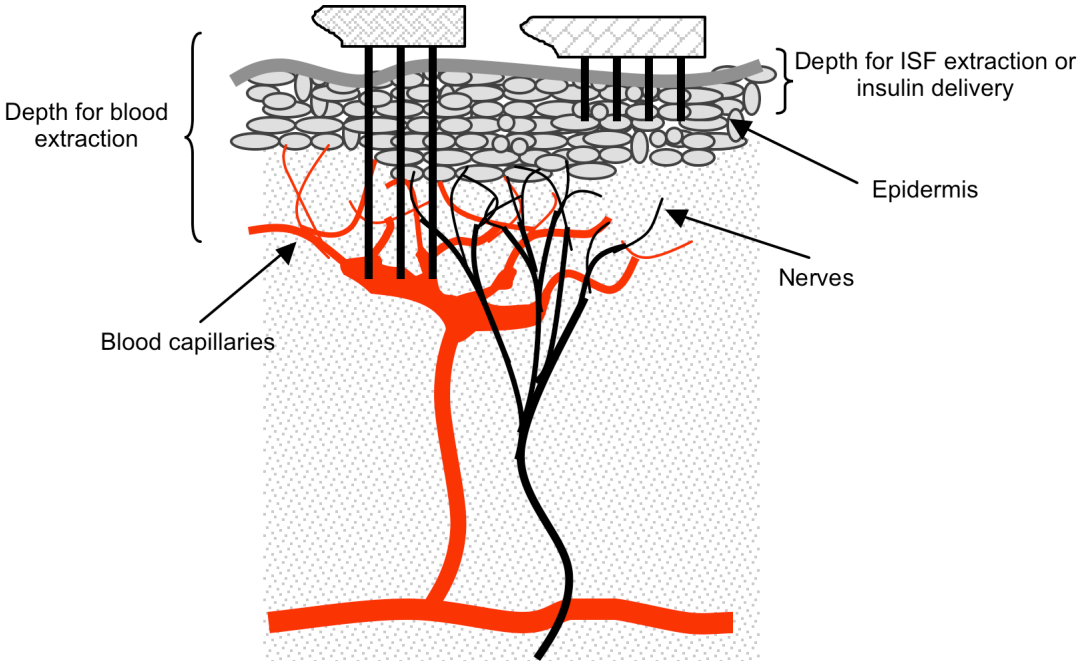

Figure 5: Relative insertion depths of microneedles [46]

1.12.1.1 Microneedles for Interstitial Fluid Sampling

The depth of microneedle penetration needs to be in the approximate range of 50–150 μm to extract ISF. Such low microneedle height requirement translates to higher latitude in design variations. Microneedles have two possible failure scenarios - fracture or buckling. In general, shorter needles, of the same diameter and material, can withstand higher pressures without failing. Thus, needles composed of relatively lower strength material, e.g. silicon dioxide, can be used for ISF sampling. Silicon dioxide is also highly biocompatible, an additional advantage. Reduced height allows for smaller needle diameters without inducing buckling [93]. A smaller tip diameter results in a much higher ratio of fracture force vs. insertion force into skin [94]. This increases the margin of safety for employing microneedles without failure. Microneedle lumen diameters for ISF sampling can typically be as low as 10 μm.

A small microneedle diameter coupled with the low density of ISF induces extremely high capillary forces. Capillary forces also increase with higher hydrophilicity of the microneedle material. This facilitates extraction of the fluid even without a pumping mechanism. Unfortunately, the flow rate through microneedle declines with decreasing diameter [95]. Thus, an initial latent time exists before the microneedles are filled with ISF [96].

Glucose sensing is a good example of ISF extraction, can serve as a model for general volumetric analysis. Most commercial ISF glucose sensors require around 0.5µl – 2µl of fluid [97], and this figure is continuously decreasing. In order to increase flow rates, an array of microneedles is used to achieve the required flow. Vacuum pump assisted ISF sampling using microneedles in humans has been demonstrated and shown to successfully track changing glucose levels following insulin injection with a time lag of less than 20 minutes [98].

1.12.1.2 Microneedles for Blood Sampling

Blood capillaries are present just below the epidermis. Generally blood microcapillaries are found at penetration depths of about 400 µm. The nerve tips are also present in the same depth vicinity. Thus some microneedles within the array might just graze the topmost nerve cells. However the extremely small diameters and controlled shank length reduce the odds of encountering a nerve or of stimulating it enough to induce pain [99, 100]. Figure 5 depicts the relative insertion depths of microneedles used for blood or ISF sampling.

In order to extract blood without significant pain, microneedle shank lengths need to be around 400–900 µm. At these lengths the microneedle needs to be built using higher strength materials such as metal or silicon. A common model used by researchers is the dimension of the female mosquito proboscis [40, 42]. The

microneedle diameter needs to be large enough to allow convenient passage to the largest blood cells. Also, the larger length necessitates larger diameters to preclude needle failure via buckling. Typical microneedle diameters have to be at least 50 μm wide. Even though capillary action alone can be enough to extract blood, factors such as higher fluid density, larger conduit diameter, and the material of choice can mitigate the effect. In such a case, a microfluidic pumping device is needed to generate negative pressure [42].

1.12.2 Microneedles for Drug Delivery

For fluid infusion, flow rates of greater than 1ml/hour for a single microneedle have been demonstrated [101]. Even with modest rates, and employing a needle array, requisite amount of dosage can be easily transferred via microneedles.

1.12.3 Fluid Flow Through Microneedles

Deciding the microneedle array specifications (pitch, size of array) is as important as design of the individual microneedle. Microneedles can sometimes get clogged by tissue being trapped in a needle lumen during insertion (beveled-tip [102] or side-opened [103, 104] needle designs minimize these effects). Employing numerous needles minimizes the influence of individual needle failures or passage blockages. Also, as mentioned earlier, use of an array formation increases fluid flow rates. The flow rate increases linearly with the number of microneedles in the array. However, care has be taken not to place needles too close to each other, otherwise a ‘bed-of-nails’ effect can result in the skin being pushed down uniformly without penetration [81]. Generally microneedles are placed more than 200 microns apart and array size can be as small as a few microneedles to hundreds.

Fluid flow through a microneedle is generally assumed to be laminar. It largely depends upon the pressure difference across the needle and is set by the microfluidic

pump and the capillary forces. Unfortunately, a fluid-mechanical description of the skin has not been established yet, and thus modeling flow through a microneedle is a complex task; complicated further by the fact that biofluids generally exhibit non-newtonian behavior. Various non-linear in-vivo effects such as liquid absorption in the epidermis, hindrance to fluid motion due to presence of cells and saturation play a role in fluid dynamics. Furthermore, there are present pressure losses due to flow down a microneedle. These can be attributed to entrance losses, drag on the duct walls, and losses due to specific microneedle geometry (expansions, bends, etc.) [105].

Basic modified Bernoulli equation is often used as an approximation to model fluid flow.

1) $$\Delta p = \mu \frac{128}{\pi} \frac{qL}{D^4} + \rho \frac{8(K_1 + K_2)}{\pi^2} \frac{q^2}{D^4}$$

Δp is the pressure drop, q is the flow rate, K_1 and K_2 are macroscopic values that represent inertial minor losses in piping systems, ρ is the density of liquid, μ is the viscosity, D is the diameter of needle and L is the length.

The Hagen-Poiseuille Equation, which describes slow viscous incompressible flow through a constant circular cross-section, is generally used to establish rough estimates.

2) $$Q = \Delta p \left(\frac{\pi r^4}{8 \mu L} \right)$$

For n microneedles the net flow rate gets multiplied by a factor of n.

1.13 Contribution to State-of-the-Art

This research intends to make the following contributions to the state-of-the-art in lab-on-a-chip devices:

1) First study on DNA binding analysis on microfluidic chamber materials.

2) Novel use of microfluidic chamber as an active element within a lab-on-a-chip device.
3) First reported fabrication of hollow microneedles with sharpened tips.
4) First reported study on shear fracture of microneedles.
5) First reported study on strength testing of silicon dioxide microneedles.

CHAPTER 2

BACKGROUND

Advanced lab-on-a chip systems have the potential to close the loop between diagnostic and therapeutic elements of diabetes treatment, thus constituting a 'smart' system [106]. A microfluidic device consists of various passive and active components. Active elements may be micropumps [6, 7], microvalves [8, 9], heaters [27, 28], micro-sonicators [29], flow sensors [13, 14] among various others. Passive elements may be microfluidic chambers [30-32], microfluidic channels [33, 34] or other external interface elements such as microneedles. Each of the components of a microfluidic device needs special attention to enhance their individual properties. In this research, microfluidic chambers as well as microneedles have been studied as components for a typical lab-on-a-chip device.

2.1 Enhancement of the Microfluidic Chamber: Material Considerations

2.1.1 State-of-the-Art in Microfluidic Chamber Material Research

Various chamber materials have been studied individually in research literature. Most commonly 'soft' materials such as PDMS and PMMA are used to form microfluidic chambers, and their properties have been extensively studied [30-32]. Recently there have been studies on large scale integration of materials to form lab-on-a-chip device [107, 108].

However, there hasn't been any comprehensive study on the relative properties of materials with respect to microfluidic chambers. This research aims to fill this gap in scientific literature.

2.1.2 Lab-on-a-Chip Systems for DNA Extraction

LOC systems are routinely used for applications involving DNA extraction from biological cells [38, 39]. A popular application of this type is chromatin immunoprecipitation (ChIP) [109]. ChIP is a recently developed laboratory method that is useful for analyzing modifications to chromatin, investigating gene expression, identifying transcription factor binding, and identifying unknown genes of transcription factors. All of these have relevance to understanding the biology of cancer. This type of immunoprecipitation has been used with increasing frequency in research applications over the past 10 years. Chromatin immunoprecipitation protocols (ChIP) also have potential for use as an early detection method for cancer.

The ChIP process is essentially a protein-DNA binding protocol. The process involves formaldehyde crosslinking of proteins to DNA in intact cells, followed by extraction of protein-DNA complexes via cell lysis. Subsequent biochemistry steps such as antibody binding, reverse cross-linking and protein digestion result in extraction of the target DNA. It is imperative that the surfaces on which the reaction is performed are thoroughly cleaned after each step because the presence of any DNA impurity in the final product is amplified during analysis. This necessitates that the microfluidic chip be made of materials that show the lowest non-specific binding of DNA through the entire processing cycle. When not bound (or loosely bound) to the chamber surface, the DNA impurities can be easily washed away to a waste chamber. Desirable washing characteristics like these make the whole process faster, more efficient, and result in higher purity output.

A material with attractive properties for use as a base material in microfluidic devices is nanocrystalline diamond. Its chemical inertness, optical transparency [110], and high thermal conductivity make it suitable for incorporation with both active and passive devices, such as channels, mixers, reaction chambers, pumps, heaters, and sensors for measuring temperature, flow, impedance, pH, etc [111]. Various microfluidic structures have been built using crystalline diamond [112-114]. Researchers have functionalized diamond films for various kinds of biological sensing applications [115-120]. However its value towards specifically biological lab-on-a-chip devices hasn't been fully exploited. Nanocrystalline diamond's surface smoothness correlates to it being an excellent chamber base material for biological entities such as proteins, DNA, cells, etc. Nanocrystalline diamond when terminated with hydrogen is a highly hydrophobic material, and its hydrophobicity can be controlled by post-deposition processes [121]. Consequently, it resists non-specific DNA surface binding. This property is significant to biological lab-on-a-chip applications such as chromatin immunoprecipitation. Researchers have shown favorable DNA preservation or DNA attachment properties of functionalized crystalline diamond [122-124]. These properties coupled with low non-specific DNA binding demonstrated here enhance nanocrystalline diamond's potential in DNA handling applications.

2.2 Microfluidic Chamber as an Active Element: Enhancement of Cell Lysis

2.2.1 State-of-the-Art in Cell Lysis on Chip

Microfluidic chambers usually behave as passive fluid "containers", with little or no active role in device performance. However, for an application such as cell lysis within a lab-on-a-chip, the microfluidic chamber can be modified to act as a "mechanical catalyst".

Cell lysis is a common procedure in microbiology protocols that requires specific implementation in a microfluidic lab-on-a-chip application. Cell lysis in a traditional laboratory is typically done mechanically via ultrasonic vibration. This physical method has the advantage that it does not require the use of chemical agents which reduces the washing in the chip. Ultrasonication has also proven to be highly effective for fragmenting DNA and is thus a more efficient lysis method for PCR [125] as opposed to electroporation which is another commonly used lysis method. Nevertheless, microfluidic lab-on-a-chip applications use chemical lysis [126] or electric fields [127, 128] for cell lysis in most cases rather than a micro-sonicator [29]. This in part is due to the inherent power limitations of an ultrasonic microresonator which limits the efficiency of cell lysis. One solution is to employ disruption microbeads that are introduced in the cell suspension to assist mechanical cell lysis [129]. These beads physical pound the cells during sonication rupturing cell membranes. Unfortunately, having loose mechanical entities in the microfluidic chamber results in complications. The beads may block the microfluidic channels, and their introduction into the chamber is a cumbersome task.

This research explores the use of micro-spikes on the microfluidic chamber walls to enhance cell disruption. During ultrasonication the cells collide against the chamber walls. During this collision, the array of spikes physically puncture the cell walls increasing the efficiency of cell lysis.

2.3 Microneedle Based Skin Interface Systems

2.3.1 State-of-the-Art in Microneedle Design

A critical design parameter in the fabrication of microneedles is the compromise between structural rigidity and ease of penetration. Due to elasticity of skin, a considerable amount of deformation takes place around the insertion site, significantly

reducing the insertion depth of microneedles [130]. The outermost layer of the epidermis, stratum corneum, is a thin, flexible, high impedance biopolymer composed of interconnected dead cells. This layer is the major barrier to various environmental insults (climatic, toxic from xenobiotics, or microbial), and needs to be punctured for fluid transfer. Below the stratum corneum lies the viable epidermal layer that is devoid of blood vessels and contains very few nerve endings. The thickness of stratum corneum and viable epidermis of typical human skin are 10-40 μm and 50-100μm respectively [131, 132]. These layers tend to deform rather than puncture upon needle incidence.

To mitigate the undesirable effects of skin deformation, the pressure applied by the needle tips needs to be increased. Insertion pressure can be increased by raising the applied force, or, by increasing the needle sharpness. An increase in applied force intensifies the strain on the microneedles and may cause undue breakage. Furthermore, it may also magnify the patient's discomfort. Vibratory actuation has been suggested to decrease the force required for insertion [133]. However, this requires the use of a vibratory actuator, which may not be possible for all applications, or might complicate the design requirements.

Permeation of microneedles can also be improved by increasing their sharpness. However, this is quite often achieved at the expense of structural rigidity. The needles must be capable of tolerating stresses related to the non-uniformity of skin contour, inadvertent slippage during insertion or removal, and reasonable human movements during period of penetration. Microneedles with extremely sharp tips, but thin needle bodies have been employed with successful penetration into skin [134]. However, structural damage after insertion was reported, as can be expected due to compromised sidewall thickness.

2.3.2 State-of-the-Art in Silicon Dioxide Needle Fabrication

Silicon dioxide being highly biocompatible is a potentially desirable material for microneedle fabrication. Silicon dioxide allows for the smallest size of needles possible, as compared to any other material. These needles are fabricated by etching silicon followed by wet oxidation [71, 72].

Traditional fabrication methodologies employ lapping of bulk silicon, which dramatically reducing the obtainable length of microneedles. Also, lapping is a harsh process, and usually results in an uneven or sloping surface. This research involved fabrication of silicon dioxide microneedles using silicon nitride as an etch–stop layer for DRIE. The same nitride layer acts as an oxide barrier. This novel use of silicon nitride results in no loss of the bulk silicon.

CHAPTER 3

DNA BINDING STUDIES ON MICROFLUIDIC CHAMBER

The goal of this task is to analyze DNA binding to nanocrystalline diamond films. Binding experiments were tailored specifically for chromatin immunoprecipitation protocol. However results are universally pertinent for other biological microfluidic applications. DNA binding tests were performed on nanocrystalline diamond samples and compared with common building materials. These materials were silicon, silicon dioxide, Polydimethylsiloxane (PDMS), Poly methylmethacrylate (PMMA), SU-8, and glass.

3.1 Materials and Methods

3.1.1 Substrate Sample Preparation

In this study, DNA binding was tested on seven materials. Substrate materials such as silicon (250 micron, (100), n-type, 10-30 ohm-cm, double side polished) and glass (250 micron, Corning 7740) were used as is. Other materials were prepared on similar silicon substrates. All materials were deposited on both sides of a silicon wafer to ensure similar DNA binding on either side. The following parameters were used – PMMA: 3000 rpm, 30 second spin, cure at 180 °C for 5 minutes; PDMS (Sylgard 184): 3000 rpm, 30 second spin, cure at 150 °C for 30 minutes; SiO_2: dry oxidation at 1100 °C for 6 hours to give 3000 Å oxide; SU-8 (Series 50): 4000 rpm, 30 second spin, soft bake at 65 °C for 6 minutes followed by cure at 95°C for 20 minutes. Nanocrystalline diamond

was grown in presence of Ar (371 sccm), CH_4 (4 sccm) and H_2 (25 sccm) for 6 hours (750 °C, 95 torr, 800W RF power). It is well known that nanocrystalline diamond grown in high percentage of hydrogen results in a natively hydrogen terminated surface. The hydrogen termination results in negative electron affinity at the diamond surface, imparting hydrophobic properties.

All seven types of samples were finally diced into equal sized squares of 6mm x 6mm to ensure equal area of exposure to DNA.

3.1.2 DNA Binding Protocol

The source of DNA for all experimentation was HeLa S3 (human cervical carcinoma) cells. All tests to expose the substrates to DNA were carried out in polypropylene tubes. Substrate material samples were separated into batches; each batch containing one piece of each type of substrate. Then, a chromatin immunoprecipitation protocol was performed in the presence of each substrate material (approximately $2x10^6$ cells for each ChIP) in order expose them to DNA. Nonspecific DNA binding was tested after each of the three major steps of ChIP (cross-linking, sonication, and immunoprecipitation).

The first few experiments were simultaneously performed in the presence of extra DNA from a plasmid carrying the specific DNA sequence to be analyzed. This extra DNA was used to amplify the response and provided verification of the results. The following protocol was performed for each of the ChIP steps.

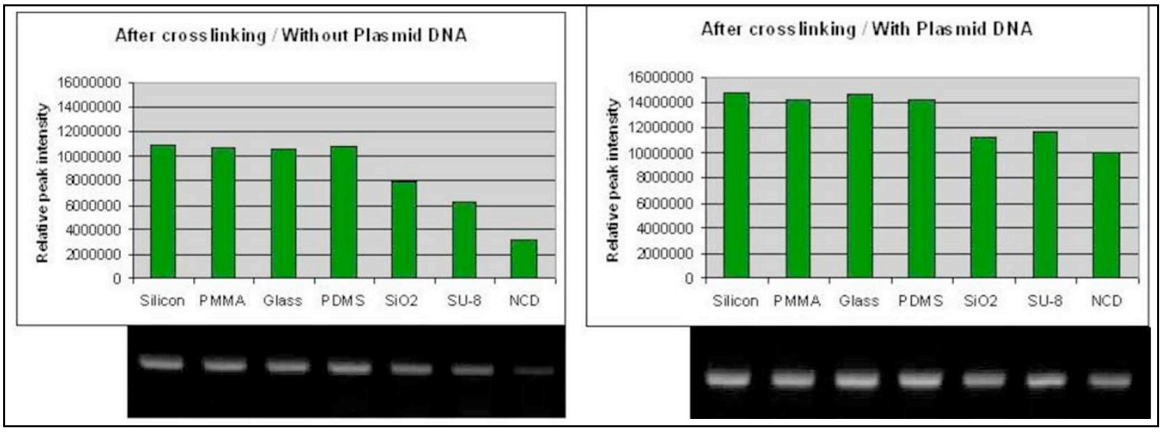

Figure 6: DNA binding after crosslinking

3.1.2.1 Crosslinking

Seven identical tubes were prepared. Each contained two samples of a particular substrate along with a suspension of cells. Crosslinking was performed by adding 1% formaldehyde (in phosphate buffered saline (PBS), pH 7.4) at room temperature. The samples were incubated for ten minutes while being rotated simultaneously in a mixer. This ensured uniform distribution of DNA on the surfaces. Crosslinking was stopped using glycine (0.125 M). The substrate samples were removed and washed in a fresh tube containing 200 μl of PBS and vortexing for 10 seconds. One of the two substrate samples was removed for analysis. The other sample underwent a second wash in a buffered detergent solution (PBS + 1% Triton X-100). This sample was also removed and placed into a fresh tube for analysis.

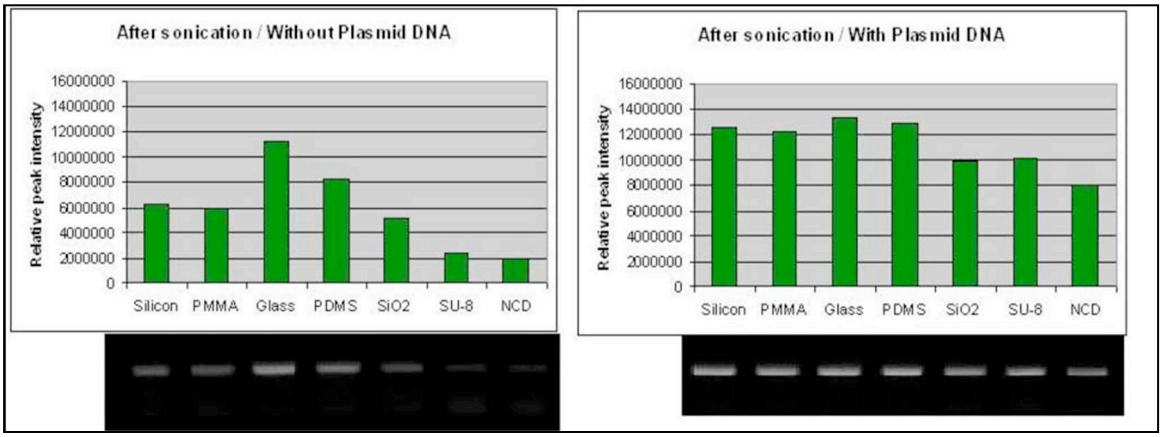

Figure 7: DNA binding after sonication

3.1.2.2 Sonication

The cells remaining from the crosslinking step were centrifuged at 4 x g for 5 minutes. The supernatant was removed. Then, 1 ml of sonication buffer (50 mM HEPES, pH 7.8, 140 mM NaCl, 1 mM EDTA, 1% Triton X-100) was added and the cells were resuspended. Two unused samples of the each substrate material were added to seven different tubes. All tubes were kept on ice from this point forward. Sonication was performed three times for 10 seconds at 5 watt power output. The two samples were removed, one was subjected to a single wash and the other was washed twice as described in the crosslinking step. Both samples were then kept in fresh tubes for analysis.

3.1.2.3 Immunoprecipitation

Two new samples of the each substrate material were added to seven different tubes. The solution remaining from the sonication step was centrifuged at 10 x g for 10 minutes. Due to fragmentation of cells and DNA in the sonication step, the DNA was present in the supernatant. 500 μl of this supernatant was added to each of the seven

tubes along with 100 μl of an immunoglobulin (IgG) specific to the target DNA which was lanosterol synthase gene. This gene was chosen because it is present as a single copy in the human genome. This IgG was conjugated to agarose beads. The samples were incubated for 3 hours with continuous mixing at 4 °C. Both the samples in each tube were washed and removed for analysis as described above.

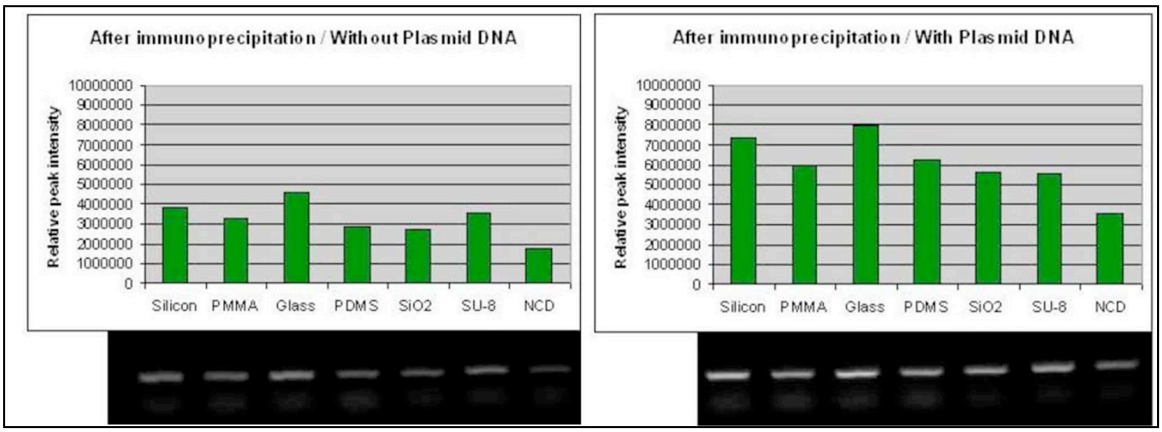

Figure 8: DNA binding after immunoprecipitation

3.1.3 Residual DNA Binding Analysis

All samples for analysis were heated to 95 °C in fresh tubes containing water for 10 minutes. Heating released the residual DNA from the sample surface into the water. Polymerase chain reactions (PCR) was performed using this solution (95°C 15 seconds, 55°C 30 seconds, 45°C 72 seconds for 34 cycles) in order to amplify the DNA. For the PCR reaction the following oligonucleotides were used. Sense: AGT GCT TGG TGA GGC AGTTT; Antisense: CCT ACC CCC AGC CTA ACT TC. Visualization of amount of DNA in the PCR output was done using an ultraviolet transilluminator. The output intensity from the transilluminator was translated into the amount of DNA in each sample. It should be noted that the output obtained from the transilluminator sometimes

contains ‘smeared’ bands, instead of a single sharp one. This is a common result due to overamplification of the PCR product, insufficient prior dilution, or too much genomic DNA [135]. However, since all samples within a particular graph undergo PCR amplification simultaneously, the results are still valid. The center sharp band is used for comparison in these cases.

As previously mentioned, the first set of experiments was also performed along with plasmid carrying the target DNA. Non-plasmid carrying samples were also tested simultaneously for control. All samples in this set of experiment underwent only one wash.

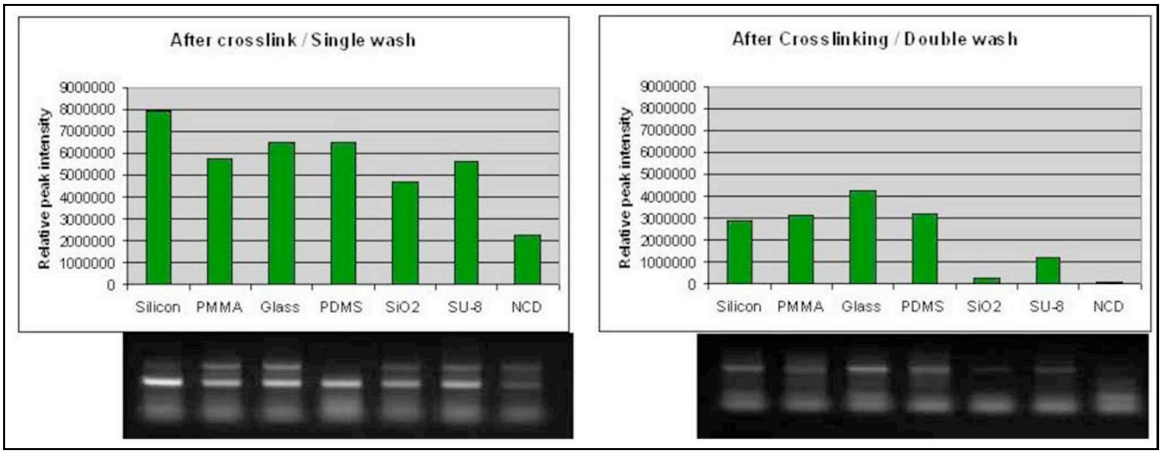

Figure 9: Single and double wash DNA binding after crosslinking

3.2 DNA Binding Analysis

Figure 6 compares the quantity of DNA removed from each substrate surface for the crosslinking protocol done without the plasmid DNA with same experiment done in the presence of plasmid DNA. The intensities obtained from the transilluminator are shown below each corresponding bar. Lower bar height depicts lower non-specific binding. Figure 7 and Figure 8 depict the results from the sonication and

immunoprecipitation steps, with and without the plasmid DNA. These results also depict similar trends. It is clear from the results that DNA exhibited the least binding to nano-crystalline diamond. These results are corroborated by the fact that they correspond very well with the set containing the plasmid DNA. Since it was evident that good amplification was obtained even without the plasmid DNA, this approach was discarded in further experiments.

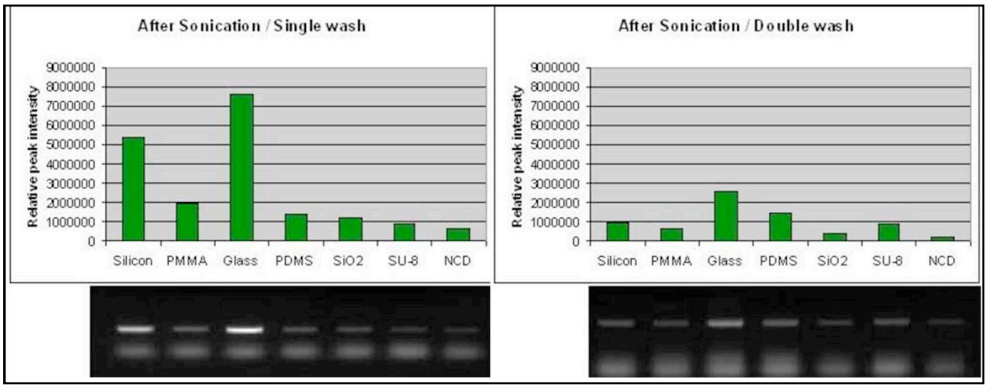

Figure 10: Single and double wash DNA binding after crosslinking

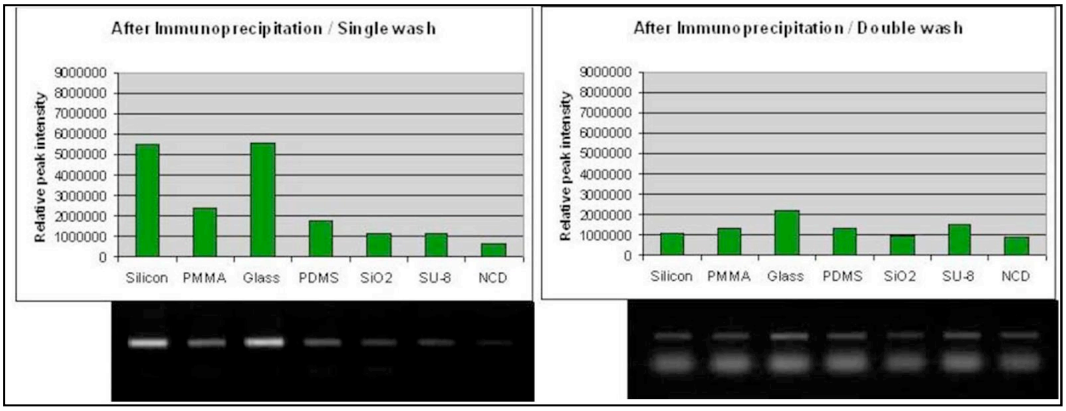

Figure 11: Single and double wash DNA binding after immunoprecipitation

Figure 9, Figure 10 and Figure 11 show outputs from double wash experiments. There was an evident drastic decrease in the amount of DNA bound in all samples, due

to the extra wash. However, note that all analyses were performed on separate samples. Also, PCR on the one wash samples was done separately from the two wash samples. Thus we cannot accurately quantify the percentage decrease in binding due to a wash. Nevertheless, all results indicate nanocrystalline diamond consistently resulted in the lowest quantity of non-specific DNA binding. Thus, it is potentially capable of offering high sensitivity / high throughput when used in lab-on-chip devices.

However, nanocrystalline diamond has non-trivial overheads in form of integration complexity and cost. The results show that SU-8 exhibited relatively on low non-specific binding as well. This material is highly conducive to fabrication of microfluidic devices, and may be a better option as a material, it might offer the best compromise between sensititivity and ease of fabrication. Even though glass is widely used, it consistently showed the worst non-specific binding, and thus can be concluded to be an undesirable material when sensitivity and throughput are of importance.

CHAPTER 4

CELL LYSIS ENHANCEMENT VIA NCD MICROSPIKES

4.1 Introduction

This research explores the use of micro-spikes on the microfluidic chamber walls to enhance cell disruption. During ultrasonication the cells collide against the chamber walls. During this collision, the array of spikes physically puncture the cell walls increasing the efficiency of cell lysis.

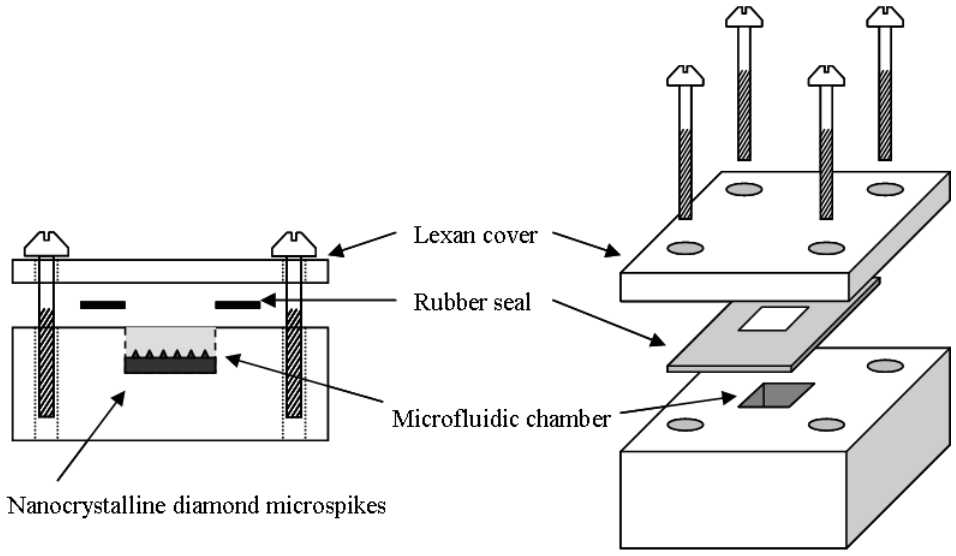

Figure 12: Sketch of cell lysis unit

For this study, the material of choice for the micro-spikes was nanocrystalline diamond (NCD). This research builds on the DNA binding research [136] which explores the use of nanocrystalline diamond for microfluidic lab-on-a-chip, and establishes that NCD exhibits the most resistance to non-specific DNA binding when compared to

commonly used lab-on-a-chip building materials such as silicon, silicon dioxide, PDMS, PMMA, glass and SU-8.

NCD is uniquely suited for cell lysis applications as its mechanical properties [137] ensures that the micro-spikes would be the most robust to survive the vigorous mechanical collisions they would be subjected to. Furthermore, NCD being a crystalline material with a small grain size, a pyramidal spike-like structure made with it results in an extremely sharp nanocrystalline tip. An increased efficiency of cell lysis via ultrasonication would greatly increase the possibility of using mechanical lysis techniques in lab-on-a-chip applications.

4.2 Fabrication of Microfluidic Chamber

The focus of this study was to evaluate the effect of using micro-spikes on cell lysis via ultrasonication. The method of sonication was not the focus of this study because different implementations might use a preferred type or design of sonicator. The underlying physics behind cell lysis via ultrasonication would remain the same, irrespective of the design of the sonicator. For this study a horn type ultrasonicator was used for cell disruption.

Custom designed cell lysis units were built using polycarbonate (Lexan from GE). Figure 12 schematically illustrates the chamber design, which included a microfluidic chamber of 200 µl volume machined into a Lexan sheet. A similar sized thinner piece of Lexan sheet was used to fabricate cover pieces for each microfluidic chamber. Identical holes for screws were drilled through the cover pieces and into the chambers. A thin rubber seal was placed in between each chamber and the cover piece to prevent leakage, and screws were used to secure the pieces together, after loading the cells. The rubber seal contained a rectangular cutout of exact dimensions of the chamber

cross-section. The cutout was made to prevent the cells within the chamber from coming in contact with the rubber seal.

Cell suspension of B16-F10 (ATCC CRL-6475) murine melanoma cells was introduced into each microfluidic chamber via a micropipette. The rubber seal was then aligned and placed over the chamber. The Lexan cover piece was placed on top of the rubber seal, and the entire stack was tightened together with four screws, resulting in a watertight seal.

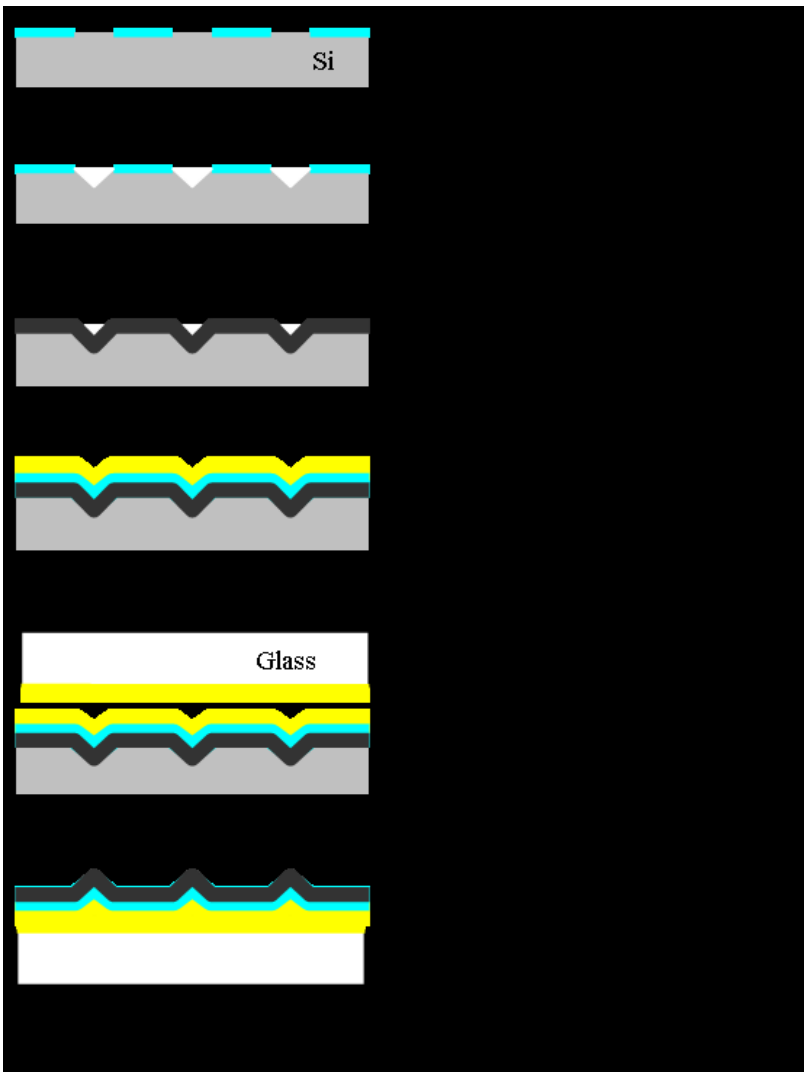

Figure 13: Fabrication process flow of nanocrystalline diamond microspikes (enhanced chamber flooring)

Two types of cell lysis units were built for the purpose of this study. The first type of unit) had a planar floor within the microfluidic chamber (henceforth referred to as a 'plain unit'. The other had nanocrystalline diamond microspikes at the bottom of its microfluidic chamber (henceforth referred to as an 'enhanced unit'). Figure 12 depicts an enhanced cell lysis unit. Several identical cell lysis units of both types were built to perform simultaneous or subsequent experimental runs with varying conditions. All units were identical in every respect except for the surface of the flooring. MEMS processing techniques were used to fabricate the 'enhanced' flooring. Bare glass was used as the flooring for the plain units. The glass substrates were permanently fixed into the Lexan cavities using cyano-acrylate adhesive, thus forming the microfluidic chamber.

4.3 Fabrication of NCD Microspikes

Figure 13 schematically illustrates the process for fabrication of the microspikes. Standard MEMS fabrication processes were used to make the flooring for the enhanced cell lysis unit. A (100) n-type silicon wafer was used for fabrication. Wet oxidation of silicon was performed to produce a 3000 Å silicon dioxide layer. Silicon dioxide was patterned using lithography and wet etching via buffered oxide etch (BOE). The mask used was comprised of an array of squares of 5 micron edge length having a pitch of 20 microns. Wet anisotropic etching was then performed using 25% KOH at 90ºC for about 10 minutes. This resulted in micropyramidal pits being formed on the silicon substrate which were used as a template for the microspikes. This size of spikes' base was chosen because it is approximately same as the diameter of the cells.

The oxide mask was then removed using BOE. The patterned sample is then ultrasonically pretreated in a mixture of nanodiamond and acetone slurry for 20 minutes followed by a sequence of ultrasonic rinse and clean steps.

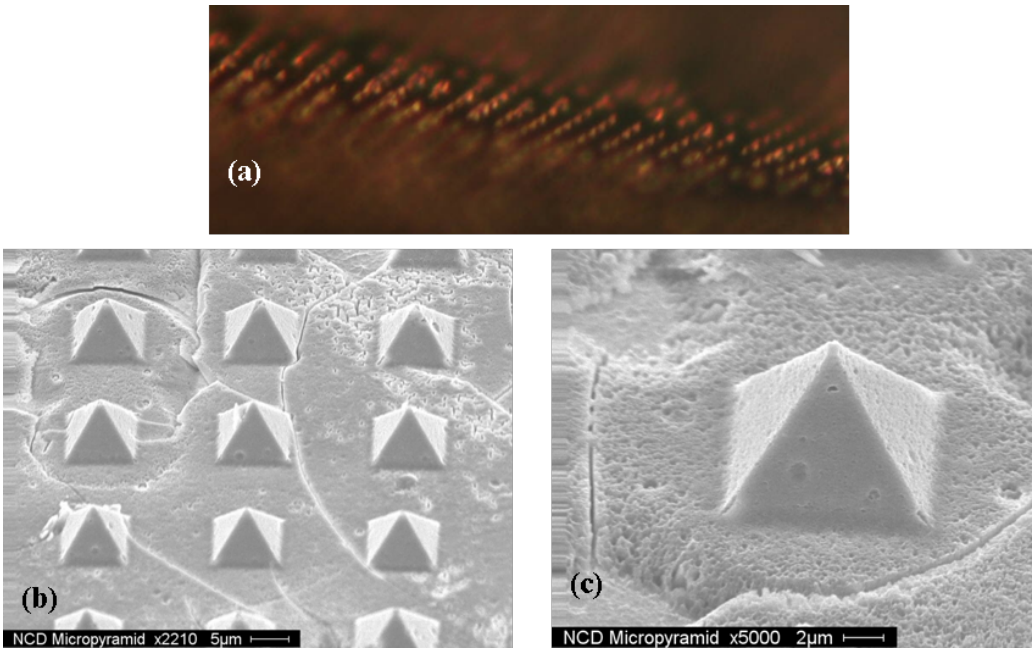

Figure 14: a) Optical image of NCD microspikes on glass substrate showing spike-like structures b) SEM images of an array of microspikes c) SEM image of a single NCD microspike.

The nucleation density achieved by this method of seeding is on the order of $10^{10}cm^{-2}$. The nanocrystalline diamond (NCD) films were grown in a Cyrannus I Iplas microwave-plasma enhanced chemical vapor deposition (MPECVD) reactor using 0.5 % methane, 1 % hydrogen and remaining balanced with argon. The process parameters were: Pressure - 135 Torr, Substrate temperature - 725°C, and a microwave power of 1.8 KW. The thickness of the NCD film was estimated to be ~ 1.5 micron. A 2 micron layer of PECVD silicon dioxide was then deposited over the nanocrystalline diamond. This layer served as an adhesion layer between the NCD layer and the subsequently deposited gold layer. It also serves to fill up most of the pyramidal cavity, planarizing the surface to some degree. This is followed by evaporation of 3000 Å of gold (over 300 Å of chrome adhesion layer). Electroplating of gold is then performed to produce a 1.8-2 micron layer. The thick layer of gold completely planarizes the surface of the wafer. The

electroplating was done at a high current density to result in a softer gold layer and thus more conducive to thermocompression bonding.

A glass wafer (Corning 7740) was taken separately and similar evaporation and electroplating processes were performed on it. The two wafers were then bonded via thermocompression bonding of gold at 400N force for 20 minutes using an EVG 501 universal bonder. This results in a glass-gold-SiO2-NCD-Si stack. The entire stack was then subjected to a 25% TMAH etch at 95ºC until all the silicon was dissolved (about 8 hours). This resulted in upright nanocrystalline diamond spikes over a glass substrate. Figure 14 shows an image of the spike like microspikes taken through a high magnification optical microscope. The image was taken at an angle to show the microspikes, and thus only part of the image is in focus.

The glass wafer was then diced to required dimensions in order to precisely fit the Lexan cavity. Bare glass wafers were also diced to the same dimensions forming floorings for the plain cell lysis units.

4.4 Experimental Protocol

This study was conducted using B16-F10 (ATCC CRL-6475) murine melanoma cells. The adherent B16 cells were grown in standard tissue culture flasks (Costar 3000; Corning Inc., Corning, NY) in McCoy's 5A medium (MediaTech Inc., Herndon, VA) supplemented with 10% (v/v) fetal bovine serum (MediaTech Inc., Herndon, VA) in a 37 °C humidified atmosphere that contained 5% CO2. Cells were prepared for experiments by trypsinization and then washing the harvested cells by centrifugation (225 x g) 3 times in phosphate buffered saline. The resulting washed cell suspension was further prepared by determining viability using the trypan blue dye exclusion test. Cell cultures that were >95% viable were used for experimentation. Before each

experiment, the suspension of harvested cells was adjusted to a concentration of 1 million cell per ml based upon enumeration in a standard hemacytometer.

Each experimental set employed three cell lysis units. The first unit was a control unit, which did not undergo any sonication (a plain cell lysis unit was used). The other two units were a plain and an enhanced cell lysis unit, both of which underwent sonication. 75 µl of cell suspension was introduced at the same time into all three microfluidic chambers. The plain and enhanced units were immersed in water (inside a beaker), and an ultrasonic horn was used for lysis (Misonix – Sonicator 3000, ½" probe – misonix part #200, operating amplitude 120 µm, operating frequency 20kHz). The sonication was carried out for 2 minutes at 69W. After sonication, cell lysis units were opened and 50 µl of SYTOX green dye was mixed with all three cell suspensions. SYTOX Green dye is an unsymmetrical cyanine stain with three positive charges and has a high-affinity for nucleic acids. The dye cannot penetrate the intact membranes of live cells, but easily penetrates cells with compromised plasma membranes. The dye exhibits a 100 to 500-fold increase in fluorescence when it is bound to any kind of nucleic acid that is present inside cells. Hence the dye fluoresces when it penetrates lysed cells and binds to nucleic acids, or when it binds to nucleic acids that are outside the cell. Therefore, it is an indicator of lysed cells. Spectrafluorometric analysis was performed on all three samples. Comparison of fluorescence data from the cell suspensions was a measure of the relative amount of lysed cells. Thus, by comparing the fluorescence the relative efficiency of the cell lysis can be evaluated.

4.5 Results

Multiple sets of experiments were carried out using the above protocol. Each set contained a control unit (no sonication), a plain cell lysis unit and an enhanced cell lysis unit. Within each set, cells from the same harvested crop of B16 cell were used to

ensure equal number of cells is present in each unit. Care was taken that the cells are introduced into the microfluidic chambers at the same time, to ensure equal viability of cells. Every separate set of experiment was performed with a different crop of cells to establish a definitive trend. Half of the sets employed cell suspensions without any cell-disruption beads. The other sets used 0.5 mm diameter glass cell-disruption beads. Ten glass beads were introduced into each chamber along with the cell suspension, and the cell-lysis protocol was carried out. Figure 15 depicts the results obtained from different sets of experiments that did not use the disruption beads. Figure 16 depicts results with sets using glass beads.

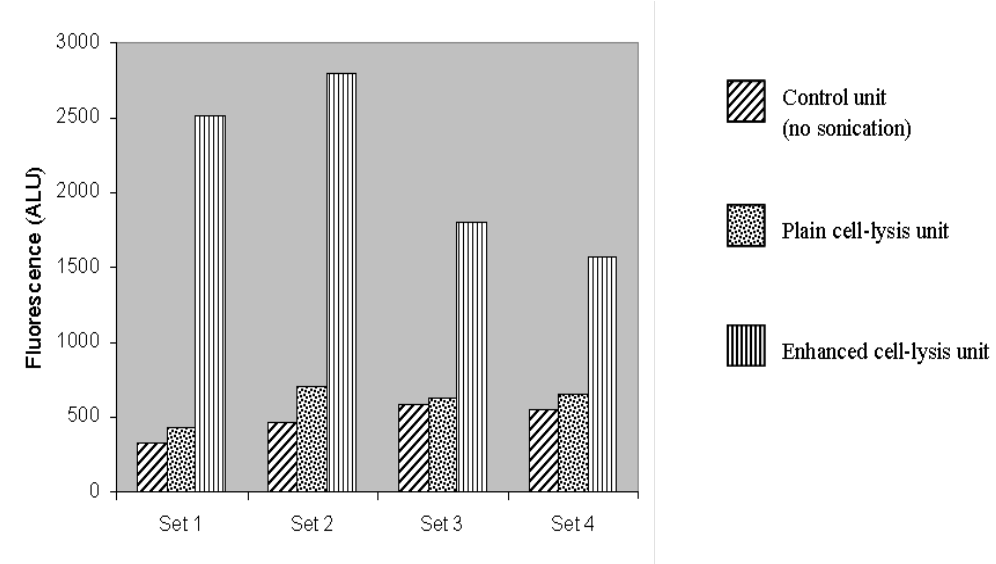

Figure 15: Ultrasonic cell lysis (without disruption beads).

Typically, there were a few nonviable cells in any prepared batch of B16 cells. These cells represent the normal quantity of dead cells in any culture, losses in viability due to repeated centrifugation, pipetting, and other manipulations that were necessary to have an enumerated cell suspension to load into the chambers. As noted above, all cells use for these experiments were >95% viable. Since a single cell suspension was used for all units within a set, and the units were employed concurrently. Therefore, the

fluorescence data for control samples represents the minimum number of nonviable cells. This number was also present in the ultrasonically treated samples; therefore, increases in fluorescence in these samples could be attributed to ultrasonic lysis.

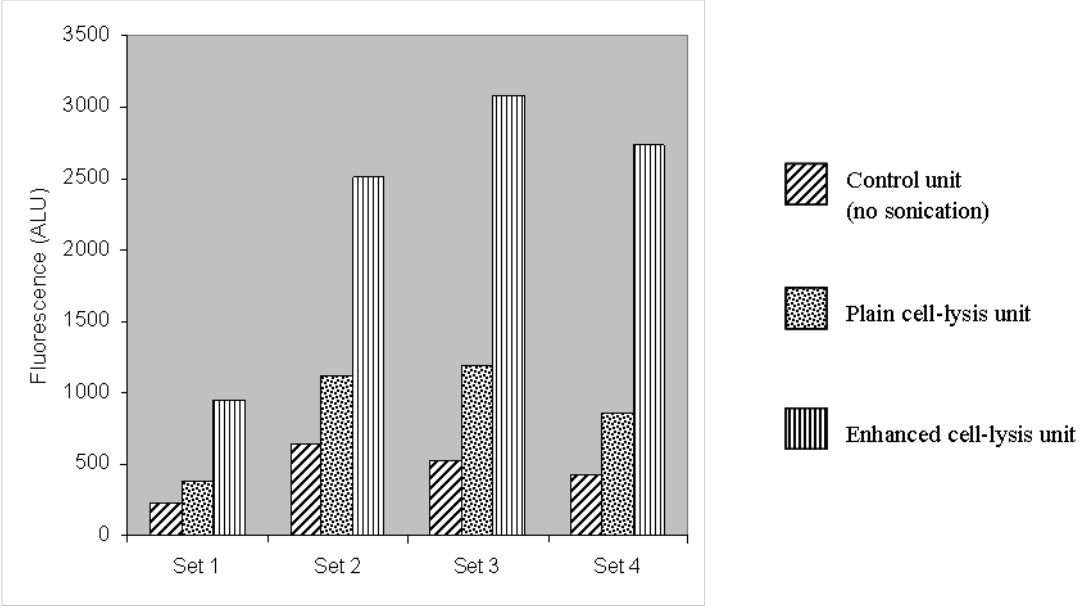

Figure 16: Ultrasonic cell lysis (with glass disruption beads)

Three sets of lysis experiments (without beads) were repeated and the numbers of alive cells were counted in the control, plain and enhanced cell lysis unit using a standard hemacytometer. Figure 17 depicts the concentration of viable cells after completion of the sonication. The starting viable cell concentration was 1 million/ml. Time required for experimental run was about an hour and the loss in viable cell concentration of the control is typical for this period. It is evident from the results that the efficiency of cell lysis via ultrasonication was greatly enhanced when micro-spikes were present on the chamber walls. The increase in cell-lysis efficiency was consistent across all sets of experiments. It should be noted that each set of experiment was performed with a different cell crop; thus the total number and viability of cells varied slightly from set to set. It can be seen in Figure 15, that plain sonication resulted in a very small

increase in fluorescence that averaged about 28%. However under the same conditions, the presence of spikes at a chamber wall resulted in 392% increase in fluorescence relative to the controls.

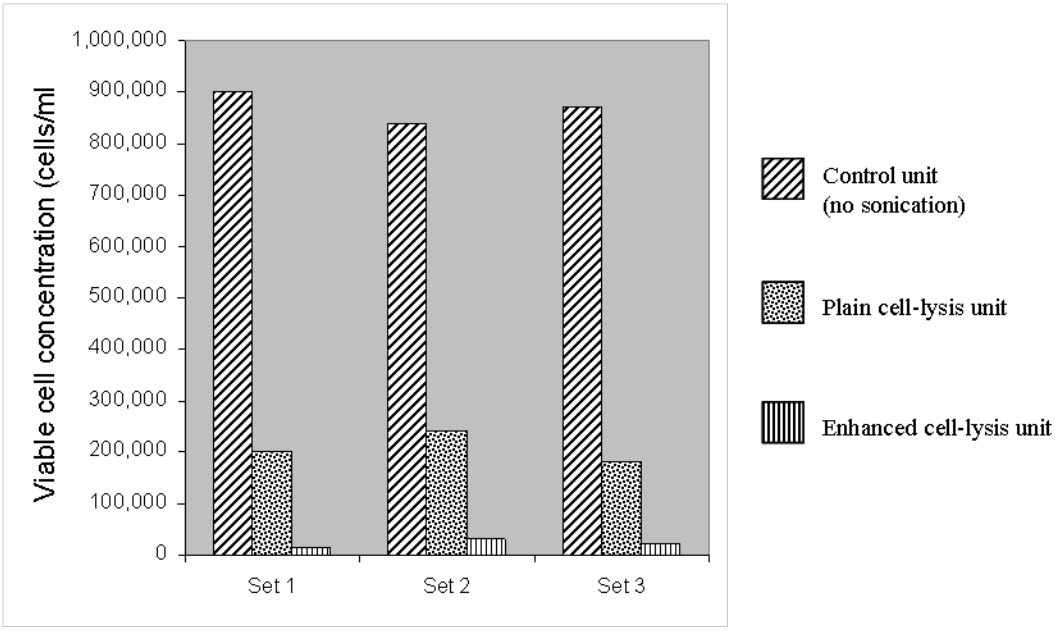

Figure 17: Concentration of viable cells after sonication

In the experiments where glass beads were present, the efficiency of cell lysis was found to be greater than that without beads. As seen in Figure 16, with beads present the fluorescence increased by an average of 93%. Thus the beads assist to a certain degree in cell lysis via ultrasonication when compared to the control and the same treatment that did not use beads. However, the fluorescence of samples in the enhanced unit recorded a 414% increase with beads being present. In the cell count experiments, the concentration of viable cells remaining in the enhanced chamber is nine times less that those in the plain chamber.

4.6 Conclusion

The results verify that a substantial increase in cell lysis efficiency can be obtained by using micro-spikes along the microfluidic chamber walls. Even when spikes were present only on one chamber wall, the increase in dead cell count was about 400% - substantially more than without spikes. The efficiency of cell lysis should increase even further if similar micro-spikes are used on multiple walls.

Even though use of glass disruption beads increased the cell lysis efficiency, this increase was not as pronounced as that with use of micro-spikes. It is interesting to note that with use of microspikes, the efficiency benefits of using disruption beads become minimal (414% vs. 392%). For a typical microfluidic application, the inherent disadvantages and inconvenience of handling glass beads in a lab-on-a-chip would greatly overshadow the performance benefits.

It was seen that even after repeated use for ultrasonication and intermediate wash cycles, performance of the nanocrystalline diamond microspikes did not decrease. Thus, NCD proved to be a robust material for such an application. Upon visual inspection, the microspikes survived multiple experiments without any discernable damage. The authors envision that portable lab-on-a-chip applications that use MEMS based ultrasonicator for cell lysis would greatly benefit from such a microfluidic chamber construction due to their inherent power limitations.

CHAPTER 5

SILICON MICRONEEDLES

5.1 Introduction

Advanced bioengineered systems have the potential to close the loop between diagnostic and therapeutic elements employed in modern treatment techniques, thus constituting a “smart” system. Many such systems will involve the transfer of physical entities through the skin. Traditional approaches used to collect biofluids or deliver drugs through the skin include needle puncture, electroporation or removal of the stratum corneum through gels or tapes; all being reasonably intrusive. A minimally invasive method for sampling or delivering biological fluids is essential to autonomous therapy systems. Microneedles can achieve this task with significantly less trauma since their sharp tips and short lengths reduce the odds of encountering a nerve.

The outermost layer of the epidermis, stratum corneum, is a thin, flexible, high impedance biopolymer composed of interconnected dead cells. This layer is the major barrier to various environmental insults (climatic, toxic from xenobiotics, or microbial), and needs to be punctured for fluid transfer. Below the stratum corneum lies the viable epidermal layer that is devoid of blood vessels and contains very few nerve endings. The thickness of stratum corneum and viable epidermis of typical human skin are 10-40 μm and 50-100μm respectively [131, 132].

A critical design parameter in the fabrication of microneedles is the compromise between structural rigidity and ease of penetration. Due to elasticity of skin, a considerable amount of deformation takes place around the insertion site, significantly

reducing the insertion depth of microneedles [130]. To mitigate the undesirable effects of skin deformation, the pressure applied by the needle tips needs to be increased. Insertion pressure can be increased by raising the applied force, or, by increasing the needle sharpness. An increase in applied force intensifies the strain on the microneedles and may cause undue breakage. Furthermore, it may also magnify the patient's discomfort. Vibratory actuation has been suggested to decrease the force required for insertion [133]. However, this requires the use of a vibratory actuator, which may not be possible for all applications, or might complicate the design requirements.

Permeation of microneedles can also be improved by increasing their sharpness. However, this is quite often achieved at the expense of structural rigidity. The needles must be capable of tolerating stresses related to the non-uniformity of skin contour, inadvertent slippage during insertion or removal, and reasonable human movements during period of penetration. Microneedles with extremely sharp tips, but thin needle bodies have been employed with successful penetration into skin [134]. However, structural damage after insertion was reported, as can be expected due to compromised sidewall thickness.

In this study, hollow microneedles with sharpened sidewall tips have been fabricated without any reduction to the needle shaft diameter. Since the microneedle sidewalls are sharpened only at the tip and not over the entire length of the needle, the mechanical stiffness is maintained, while reducing the insertion force. The outlined process achieves needle formation and tip sharpening in a continuous single-step process, greatly reducing the complexity of fabrication. Using this process, extremely sharp sidewalls can be obtained greatly reducing the penetration force. Furthermore, since the process uses dry etching, a simple change in etch recipe can result in different sidewall tip angles.

5.2 Fabrication of Silicon Microneedles

The silicon microneedles were fabricated using a 4 inch, 400 μm thick, <100> oriented, double side polished silicon wafer. The lithographic mask set contained various microneedle arrays with sizes ranging from 33 gauge to 36 gauge. First, lithography was performed on the backside of the wafer using photoresist AZ P4620. This step patterned the wafer with circular holes outlining the through-wafer microfluidic channels for fluid delivery. Next, DRIE was performed on the backside of the wafer, forming approximately 200 μm deep holes. Lithography was then performed on the front side of the wafer, again using photoresist AZ P4620. The corresponding mask used was a bright field mask, which patterned annular rings on the front side of the wafer. This step outlined the microneedle sidewalls. Next, DRIE of silicon was done to form the microneedles. This step was precisely timed to obtain the desired length of the needles.

It is important to note that no hard mask is used for etching the microneedles. This is because the sharpening of the microneedle tips depends upon controlled depletion of the photoresist. Depending on the duration of the second DRIE step, the etching at this step might cease before the desired needle lengths are obtained. This is because due to loading effects in DRIE the needle bores etch faster than the exposed bulk region of the wafer. As soon as a through-hole is formed at any part of the wafer, helium present at the backside of the wafer (for cooling) escapes into the main chamber, breaking the plasma. At this stage, the wafer needs to be mounted on an aluminum chuck to proceed with further etching. A thermal grease (Cool-Grease^{TM}) is used at the backside of the wafer to dissipate heat. DRIE of silicon is continued for the requisite time remaining. The wafer is then solvent-cleaned to remove the photoresist and the thermal grease.

5.2.1 Sharpening of Microneedle Tips

The sharpening of microneedle tips is based on precise timing of the second DRIE step and controlled depletion of the photoresist. In the Alcatel DRIE system at USF, the photoresist gets depleted at approximately 0.16 to 0.20 μm/minute during silicon DRIE via Bosch process. Thus, the maximum length of microneedles that can be obtained is limited by the thickness of photoresist used. When most of the photoresist has been depleted (less than 1.5 μm thick), the resist loses its resolution, and starts getting etched from the sides as well. Thus, it is observed that for the last few minutes before complete depletion, the feature width of the resist reduces resist gradually. This reduction of resist feature width corresponds to reduction of the annular ring area forming the protective mask. The outer diameter of the annular ring gets reduced while the inner diameter increases.

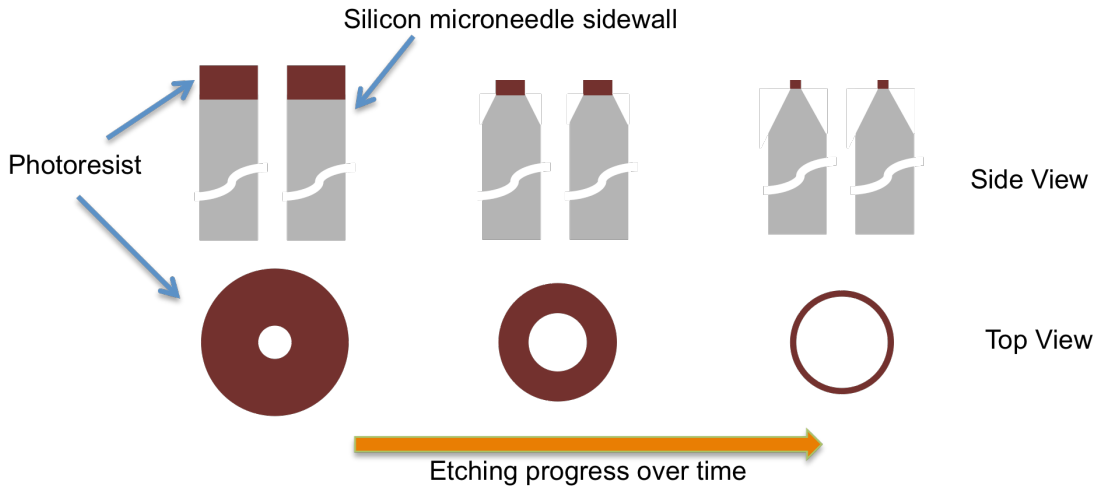

Figure 18: Sharpening of microneedle needle tips via gradual reduction of photoresist mask

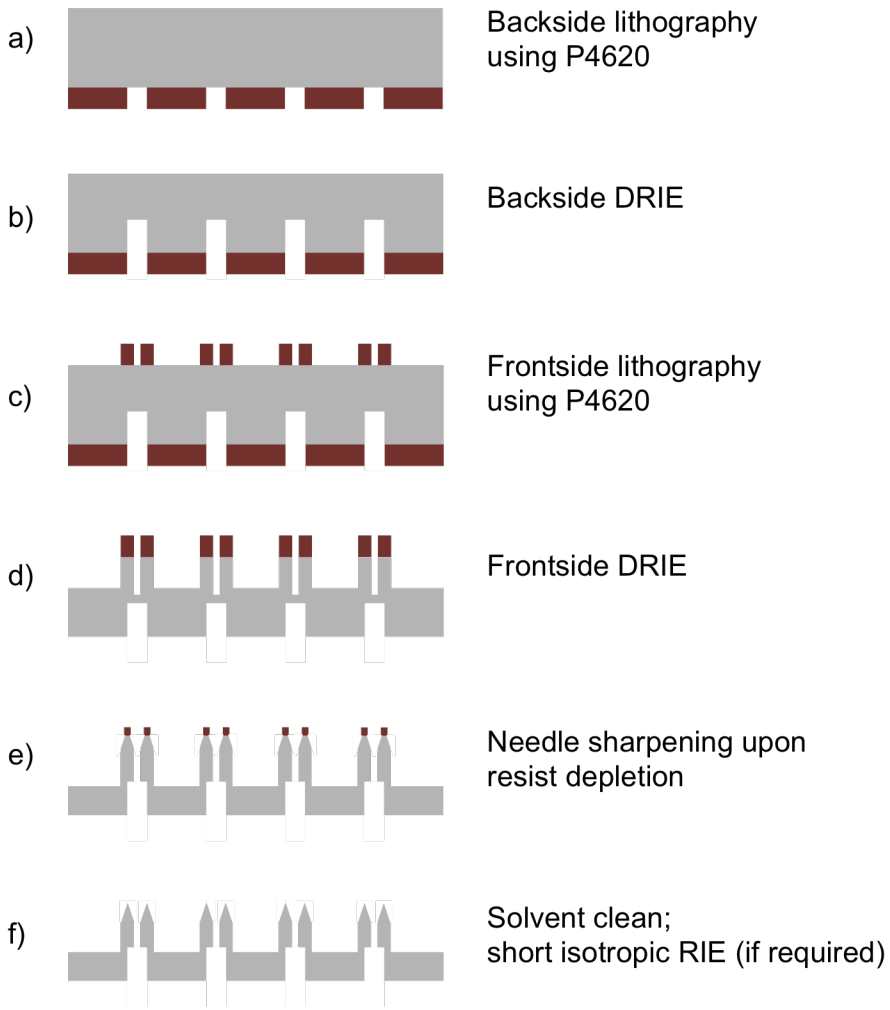

Figure 19: Fabrication process of sharpened silicon microneedles

The gradual change in photoresist mask size during the DRIE causes a tapered etch profile to be created. This has been depicted in Table 1. The taper angle depends upon the etch rate of silicon as well as the depletion rate of photoresist, i.e. the etch selectivity. By reducing the selectivity between photoresist and silicon, a higher taper angle can be obtained.

A reduction in selectivity can be brought about by appropriate changes in the DRIE recipe. In general, anisotropic etch processes depend heavily on ion-driven chemical interactions between adsorbed fluorine-containing species and the silicon

surface. Maximum etch rate conditions are achieved when the residence time of reactive species is increased by using a lower total gas-flow rate or when the partial pressure of the reactive precursor gas is increased. The plasma-generated neutral chemical species do not readily etch the silicon surface, but do play a role in the photoresist etching. By changing the interactive physical and chemical etching of photoresist and silicon the selectivity can be varied. This is usually implemented in plasma etch systems by independently controlling the power input to the plasma and the bias voltage applied to the wafer. The relative numbers of neutral species and reactive ions depend on the specific plasma operating parameters such as RF power input, gas residence time in the plasma zone, total reactor pressure, and partial pressure of the individual precursor gases [138]. In general, an increase in selectivity is brought about at the expense of a reduced etch rate.

The vertical length of the taper profile was observed to vary from approximate 30 μm to 40 μm. It is important to precisely time the etch duration. As soon as the entire resist is depleted, the microneedles are completely exposed to DRIE etching. The etch rate observed in the Alcatel DRIE system ranges from 4 μm/minute to 10 μm/minute, depending on the loading effect due the particular mask design. Thus, even a few minutes of over etch can result in complete loss of the needle tip. At this stage, the needle tip etches at about the same rate as the wafer base, thus limiting the maximum length of the needle. The microneedle, very quickly becomes blunt during the over etch phase. Table shows the thickness of the photoresist along with the corresponding maximum length of microneedles obtained.

Table 1: Dependence of maximum microneedle length on photoresist thickness

Photoresist mask thickness (AZ P4620)	Maximum length of microneedles
6.2 μm	120 μm
7.6 μm	150 μm
10.3 μm	200 μm

Figure 20 shows SEM images of a partially tapered silicon microneedle. The top view shows the tapering of a 45 μm sidewall down to 25 μm.

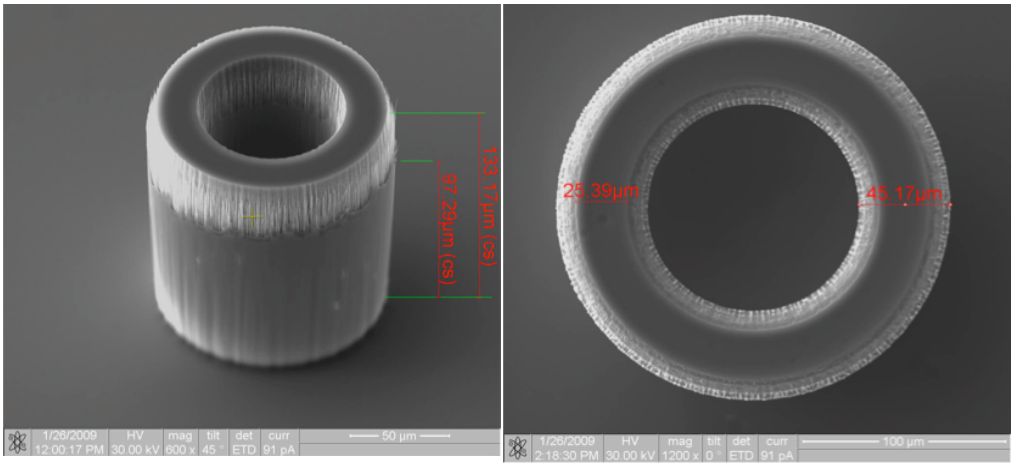

Figure 20: Partially tapered silicon microneedle

As etching proceeds, further sharpening of the microneedle takes place. Figure 21 shows SEM images of microneedles with further sharpened tips. Figure 22 shows the top view of a silicon microneedle clearly depicting sharpening of the needle sidewall from about 43 μm to less than 8 μm.

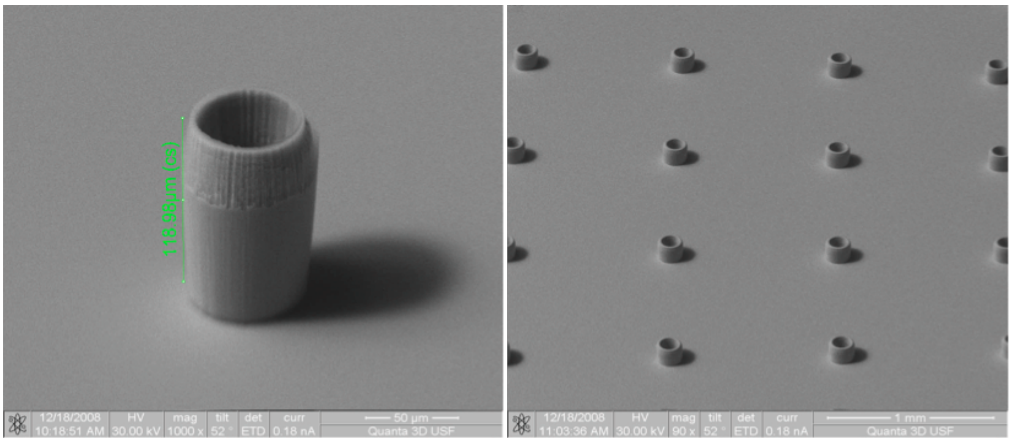

Figure 21: Silicon microneedles with sharpened tips

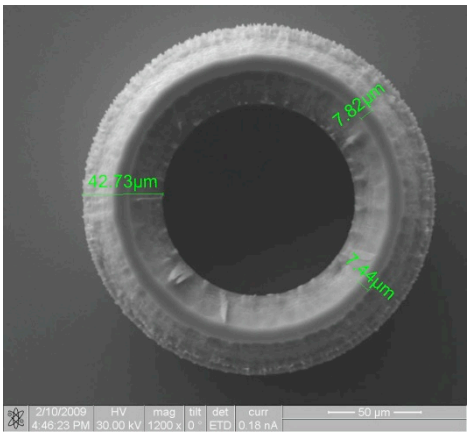

Figure 22: Top view of silicon microneedle showing extent of tip tapering

At the precise point of the complete resist depletion extremely sharp needle tips can be obtained. This is seen in Figure 23. The tip of these needles is in the sub-micron range.

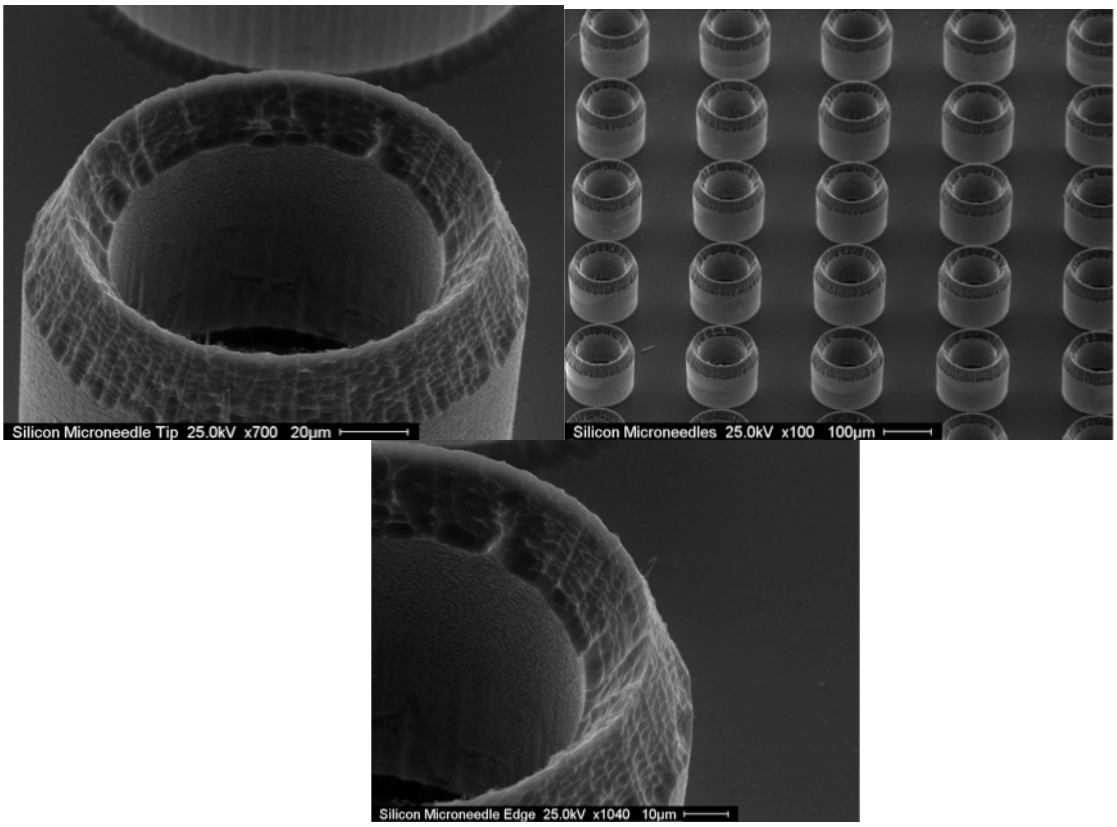

Figure 23: Silicon microneedles with extremely sharp tips

It is essential to note that the tapering process takes place particularly fast as compared to the preceding etching process. To obtain 200 µm long microneedles, a 55 minute DRIE etch is required. However, even a few minutes of over-etch beyond that resisted depletion causes the needle tip to be compromised; resulting in blunt needles as shown in Figure 24. Thus, extremely tight control of obtained photoresist thickness, lithography and DRIE are required for successful fabrication.

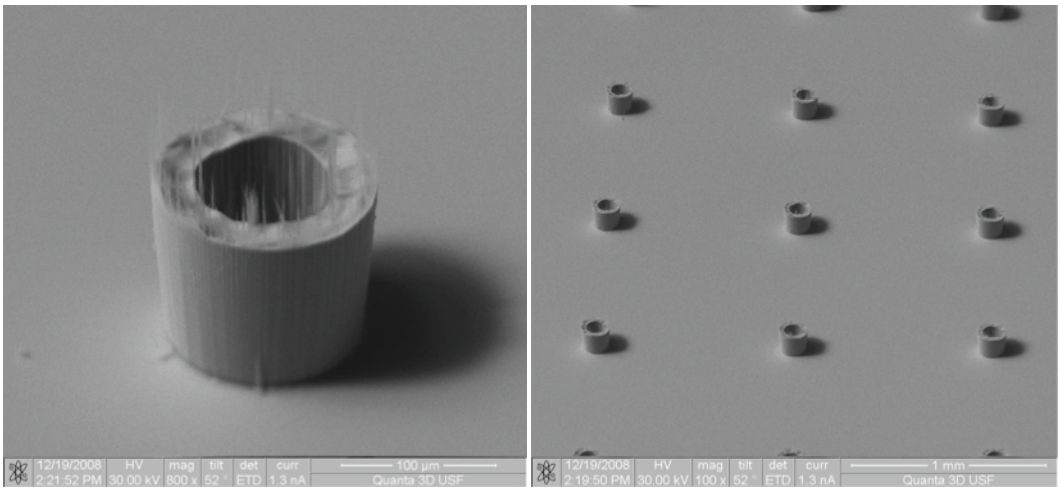

Figure 24: Over-etched silicon microneedles with blunt tips

5.2.2 Electron Shading and Micromasking Effect

It was observed that, when wafers of higher resistivity (100 to 200 ohm-cm) were used, spike-like projections were formed at the inner and outer edge of the microneedle sidewalls, as seen in Figure 25. This effect can be attributed to pattern dependent charging in plasmas. In plasma processing, there exists a significant difference in directionality between ions and electrons bombarding surfaces. This is a fundamental consequence of 'plasma sheath' dynamics. Most of the ions impinge onto a wafer surface at directions closer to the surface normal while most of the electrons arrive at oblique angles of incidence. Thus, the electron flux is isotropic and the ion flux is anisotropic along the surface normal. Current balance is accomplished when equal fluxes of ions and electrons impinge onto each surface segment. The directionality difference has no important repercussions for flat surfaces. However, it can significantly perturb the current balance when the surface is patterned as a result of geometric shading from the oblique electrons by the features that constitute the pattern [139]. The phenomenon, termed "electron shading" [140]. In the case of microneedles, due to

electron shading, there is a lack of ion flux impinging on the microneedle sidewalls. This results in local negative charge build-up at the entrance of the trenches [141].

Due to the negative charge accumulation, positively charged reactive ions get deflected away during DRIE etching. The greatest charge accumulation occurs at the edges of the features. Thus the polymer deposited at the edges of the features during the passivation step of the Bosch process, does not get completely etched away. This remaining polymer acts like a small mask, resulting in 'micromasking'. Due to the micro-masking effect silicon spikes are formed at the edges of the microneedle sidewalls. These spikes are also sometimes known as 'black silicon' or 'silicon grass' [142, 143].

The spikes formed due to electron shading and micromasking were removed by a 45 second isotropic etch in an SF_6/O_2 plasma.

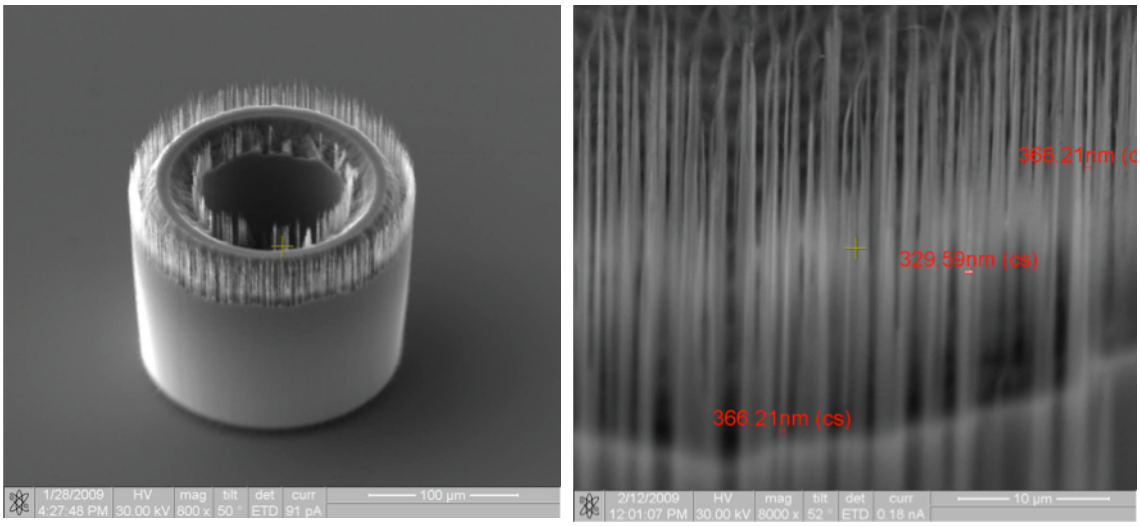

Figure 25: Silicon spike formation due to electron shading and micromasking effects

5.3 Skin Penetration Testing of Microneedles

In order to ascertain the advantage of microneedle tip sharpening, the variation of skin penetration force with tip geometry was studied. 34 gauge needles etched to

different levels of needle tip sharpness were fabricated, and the corresponding penetration force was tested. Tests were carried out on human cadaver skin preserved at -80°C.

The experimental setup consisted of a skin loading block and a needle attachment block. The skin was mounted on in the 0.5 inch x 0.5 inch aluminum block using double sided adhesive tape. The aluminum block, in turn, was attached to a pension-compression load cell (LCFA-500gF sensing capacity, Omega Co.). The internal construction of these load cells consists of a full four-arm Wheatstone bridge, capable of producing repeatable measurements. The load cell was interfaced to one channel load cell input, 16-Bit, RS-485 Data Acquisition Module (Superlogics-8016) to obtain real time results. The load cell was supported on a steel block, mounted on a XY stage with two 1 μm resolution manual micrometers screws (SM-13, Newport Co.).

A 4x4 array of 34 gauge silicon microneedles with 1000 μm pitch was mounted on the needle attachment block using double-sided adhesive tape. This block was supported on an XYZ stage with motorized micrometers (Z600 series Thorlabs Motorized Actuators) with 1 μm resolution. The motorized actuators were controlled by a custom-built LabVIEW program, which also displayed the real-time output from the load cell. Real-time visual monitoring of the needle insertion was done by a long-distance high magnification microscope. Video capturing was done via a camera mounted on the microscope.

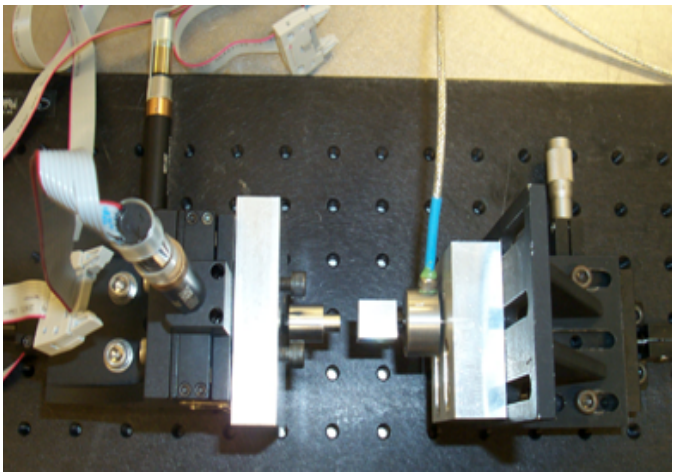

Figure 26: Skin penetration testing setup using motorized actuators

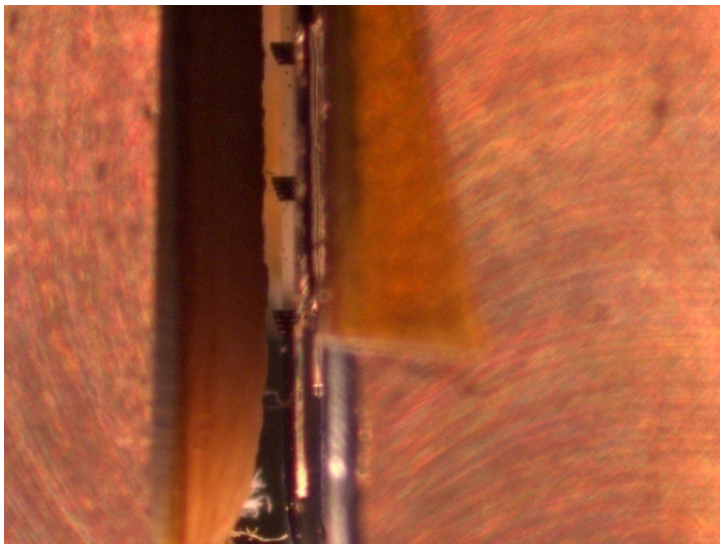

Figure 27: Visual monitoring of microneedles insertion into skin

The skin was loaded on the load cell immediately after bringing it to room temperature. At this point, and the reading from the load cell was allowed to settle down for a few minutes. The micrometer actuators allow for precise control of the needle and skin position. Through careful monitoring via the microscope, the needles were brought extremely close to the skin surface as seen in Figure 27. In order to obtain reliable force data, the microneedles were inserted at a slow rate off 50 μm/minute into the skin. The

force output from the load cell and the distance travelled by the micrometer actuator were recorded via the data acquisition system.

During microneedle insertion, the skin initially resists the penetration of the needles. This is observed as a rise in the force output from the load cell. At the point of microneedle insertion, the stratum corneum is ruptured and the needles undergo a sudden movement into the skin. This sudden movement is translated by the load cell as a corresponding drop in the measured force. All microneedles were observed to remain intact after removal from skin.

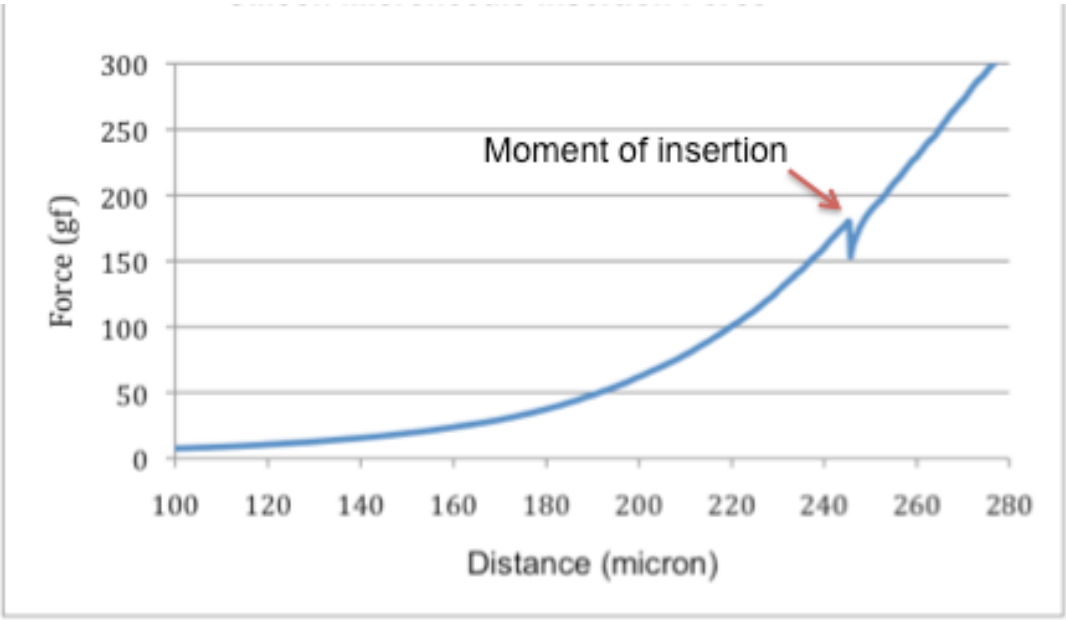

Figure 28: Insertion force of silicon microneedles

Figure 28 depicts a graph of monitored force versus distance travelled by the microneedles. From the graph, the particular set of microneedles used required a force of about 180 gf to penetrate into skin.

In order to confirm that the force drop observed was indeed due to presence of needles, a control experiment was carried out. In this case, a square piece of silicon

wafer of the same size as the microneedle array was used instead, and pressed against the skin. Figure 29 shows a typical result obtained from the control experiment. The graphs obtained from the control experiments overlap with high degree of agreement with the microneedle insertion tests. This shows that the skin deformation dynamics remain similar in both cases.

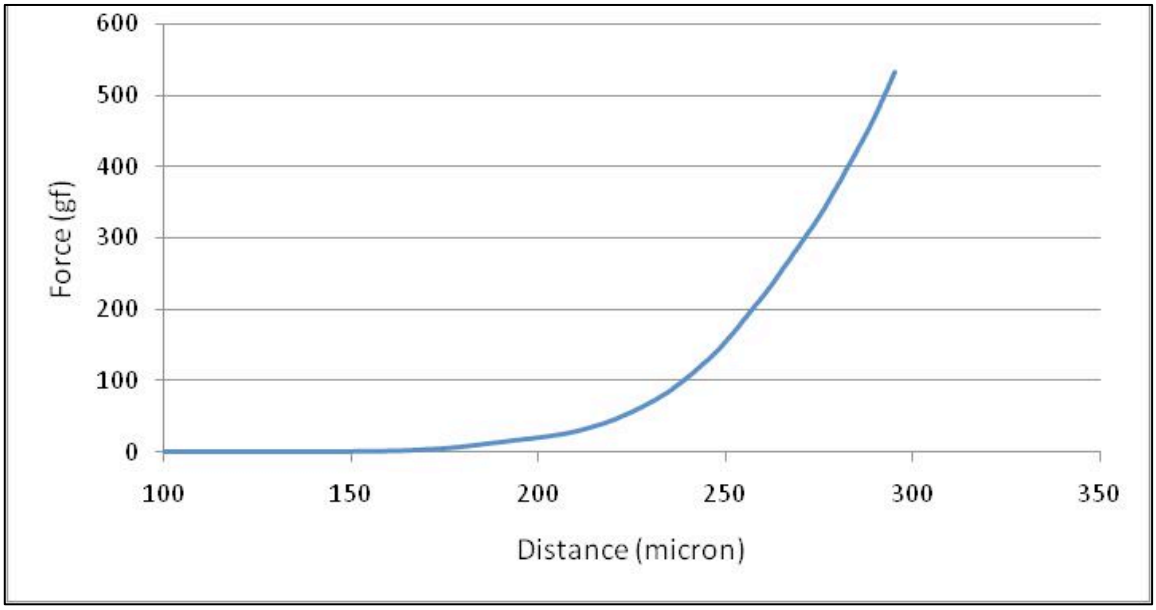

Figure 29: Skin insertion control test without microneedles

5.3.1 Analysis of Microneedle Insertion Into Skin

Initial indentation into skin is accompanied by deformation of the skin surface. Such deformation is typical of microneedle insertion into skin. For the purpose of rudimentary analysis, the force transducer can be assumed to be a spring gauge. The force measured by the gauge is translated from the compression of the spring. The measured force gets compromised due to deformation of the skin.

Let C_N be the compression of the spring at various intervals (N=1, 2, 3 etc.). Let M_N be the corresponding movement of the microneedles, and let S_N be the deformation

of the skin. The actual compression of the spring is mitigated by the skin deformation. Therefore,

1) $C_N = M_N – S_N$

By Hooke's law (for spring constant K and Force F_N):

2) $F_N = - K \times C_N$

3) $F_N = - K \times (M_N - S_N)$

4) $M_N = - F_N/K + S_N$

For the lower range of movement, the skin deformation is comparable to the microneedle movement, i.e. S_N is in the same magnitude range as M_N.

The graph plots F_N vs. M_N. From equation 3, it is clear that due to S_N the graph can be expected to be non-linear in the low range of needle movement. This is indeed observed in Figure 28. As the needles continue further movement, the incident force on the skin increases. This is accompanied by an increase in spring compression. However, as the skin reaches its deformation limit, the value of S_N starts becoming negligible as compared to the microneedle movement M_N. From equation 3 it is clear that as M_N and F_N increase, and S_N becomes comparatively negligible, the graph should start to become linear. This again is observed in Figure 28.

The stratum corneum is the hardest layer of the skin. As soon as the stratum corneum is ruptured, the lower layers of the epidermis provide much lower resistance to the microneedle insertion. Thus it is expected that as soon as the insertion occurs, most of the entire length of the needles get inserted into skin. It has been reported in literature that due to skin deformation, the length of the needle penetrating into skin gets limited and the entire length of needle does not penetrate [130].

The proposed insertion mechanism of microneedles into skin has been depicted in Figure 30. Initially, the microneedle forms a slight indentation on the top surface of skin as shown in Figure 30-a. As the microneedle moves further, the skin deformation

increases, as shown in Figure 30-b. The skin gets deformed before rupturing due inherent resistance to penetration. The amount of resistance ability of skin can be thought of as a potential energy stored within it. When the energy incident via the needles surpasses the potential energy within the skin, penetration occurs. At this point, the penetration is relatively instantaneous, especially at high insertion forces. Figure 30-c shows a post-insertion sketch of the microneedle. At the instant of penetration, the skin (which is being pushed by the spring gauge at its back), moves slightly towards the needle array, thus registering a force drop. As shown in the figure, as soon as the stratum corneum ruptures, the microneedle travels as deep as possible into the skin. The base of the array now touches the skin surface.

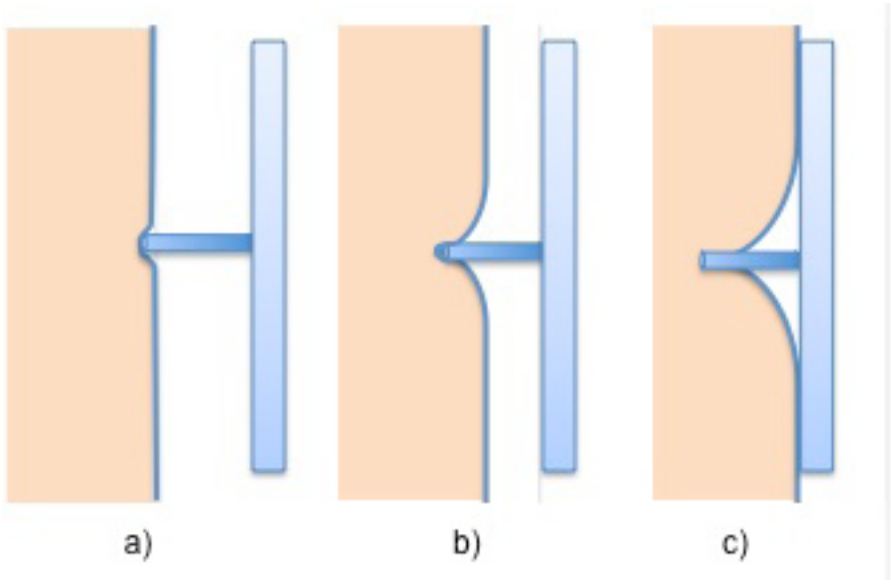

Figure 30: Microneedle insertion mechanism into skin

As seen from Figure 27, the thickness of the skin was much a higher (couple of millimeters), as opposed to the 200 micron long needles. Thus, the needles are not expected to touch the aluminum back-plate behind the skin. After the instant of insertion, the silicon base continues to push against the skin, and the force registered continues to rise in a similar fashion to the control experiment.

5.4 Insertion Force Variation With Tip Geometry

To ascertain the variation of skin insertion force with variation in microneedle tip geometry, microneedle arrays of the different tip sharpness were fabricated. A 4x4 array of 200 micron long, 33 gauge needles were used for this analysis. Arrays with four different sharpness levels were compared; completely blunt tip, partially sharpened tip and very sharp tip. Fresh piece of cadaver skin was used for each of these tests. Care was taken to perform the experiments immediately after the skin thawed out. This ensured that drying of the skin did not play a role in the penetration measurements. Table 2 shows the different needles used for the skin insertion tests.

Three sets of measurements were taken using each of the microneedle arrays under investigation. The incident force applied by the needles was plotted against the distance moved by the needles. The motorized actuators allowed for very precise control of the distance moved by the needles.

Except for the blunt needles, a sharp drop in force was observed at moment of insertion, for all the tests. Furthermore, all graphs contained only one instant of force drop, as is expected. Figure 31 shows the result of one of the insertion force tests using ‘less sharp’ microneedles.

Figure 32 depicts a typical graph of insertion force measurement using partially ‘sharp’ needles, while Figure 33 depicts one of the results obtained from ‘very sharp’ needles. The results from these tests were tabulated as shown in Table 3.

Table 2: Microneedles tip sizes used for skin insertion tests

Needle type	Tip area (μm^2)	SEM Image
Blunt	18636.43	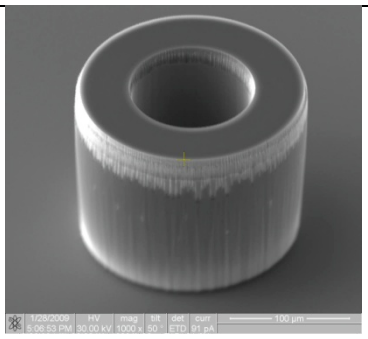
Less Sharp	11083.57	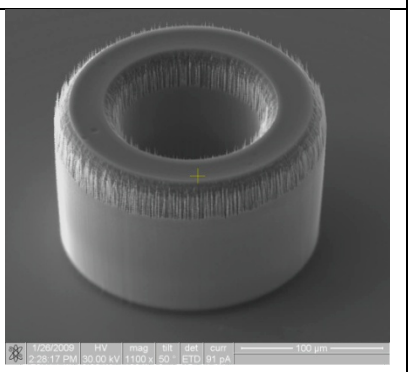
Sharp	3068.04	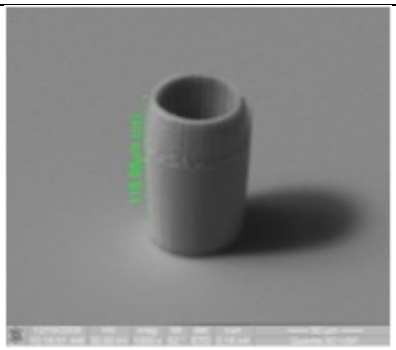
Very Sharp	185.98	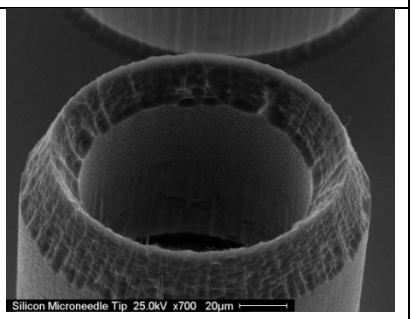

The load cell used for this testing was rated at 500gf. For the blunt microneedle tests, the insertion into skin was not seen within 150% of this range. Since it is not advisable to use the load cell beyond this range, needle insertion of the blunt needles could not be observed.

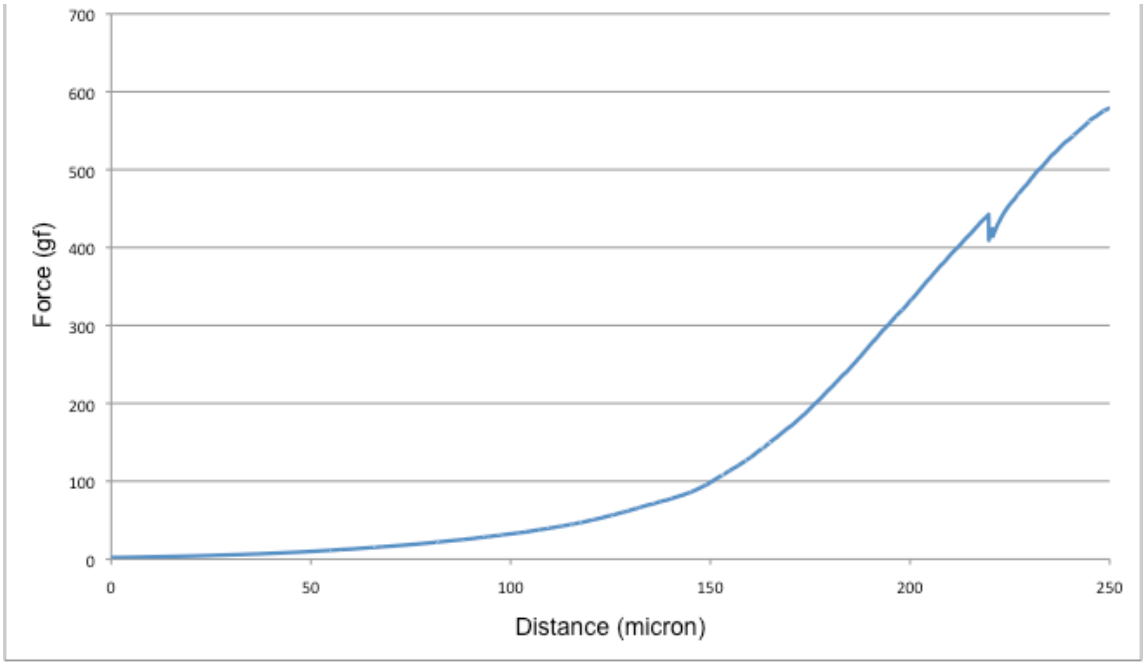

Figure 31: Incident force of 'less sharp' microneedles

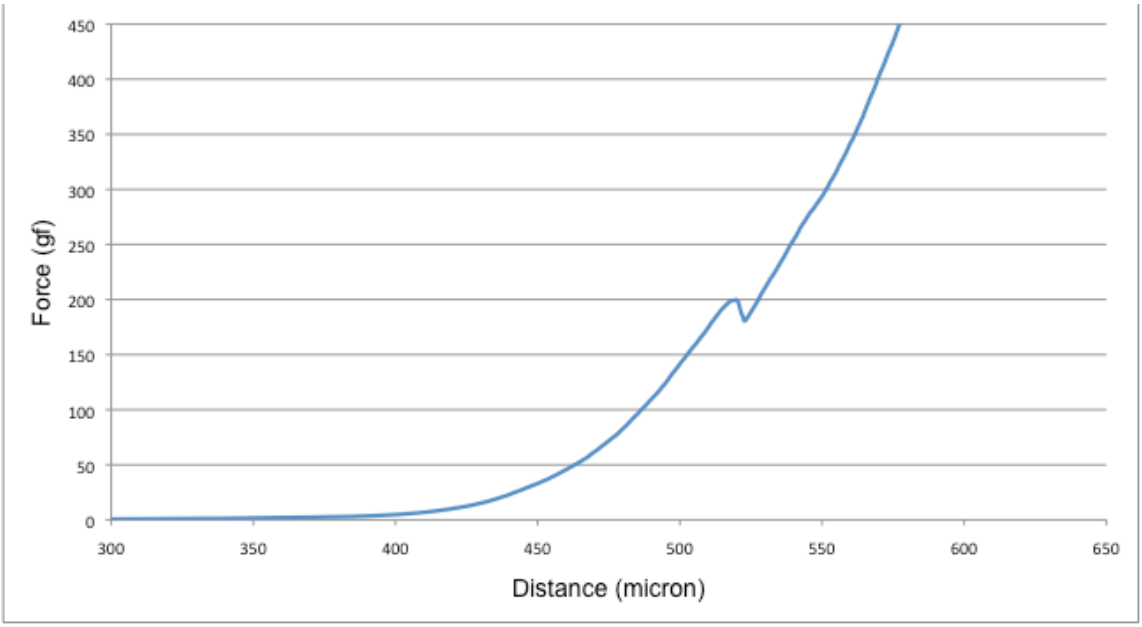

Figure 32: Incident force of 'sharp' needles

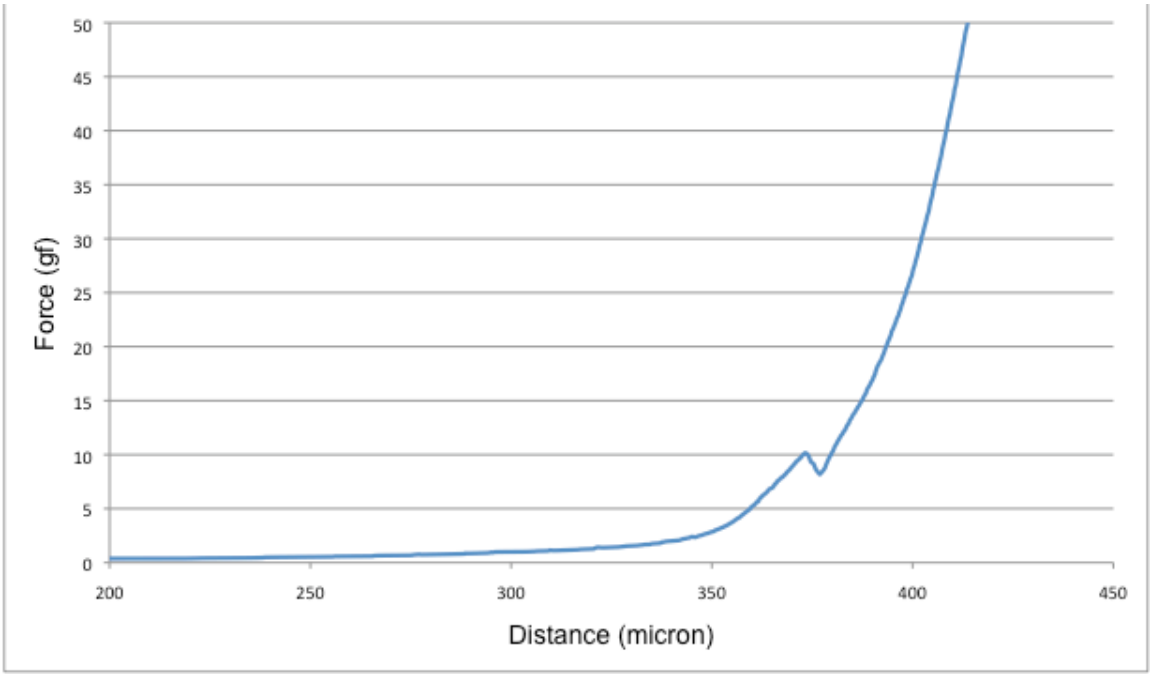

Figure 33: Insertion force of 'very sharp' needles

Table 3: Force of insertion for different microneedle array tips

Test no.	Force of Insertion (gf)			
	Blunt Needles	Less Sharp Needles	Sharp Needles	Very Sharp Needles
1	Not observed	442.4	228.3	11.5
2	Not observed	478.78	199.8	11.3
3	Not observed	504.23	179.27	10.1
Average	N/A	475.14	202.46	10.97

The results of skin insertion tests, as seen from Table 3, clearly reveal a marked decrease of insertion force with sharpening of microneedle tips. In order to ascertain the dependence of tip area on insertion force, tip surface area of the three types of needles was calculated after a visual inspection of the needle tips.

The tip area for the various microneedles was plotted versus the observed insertion force. Figure 34 depicts the dependence of needle insertion force on microneedle tip area. This dependence is seen to have the linear progression. Microneedles penetrate through the skin at the critical puncture pressure. Since the applied pressure is a function of applied force and tip area, the linearity seen in Figure 34 is expected, and, in fact corroborates the validity of the results. From the slope of the graph, the average penetration pressure per needle was found to be 0.0395 gf/μm^2.

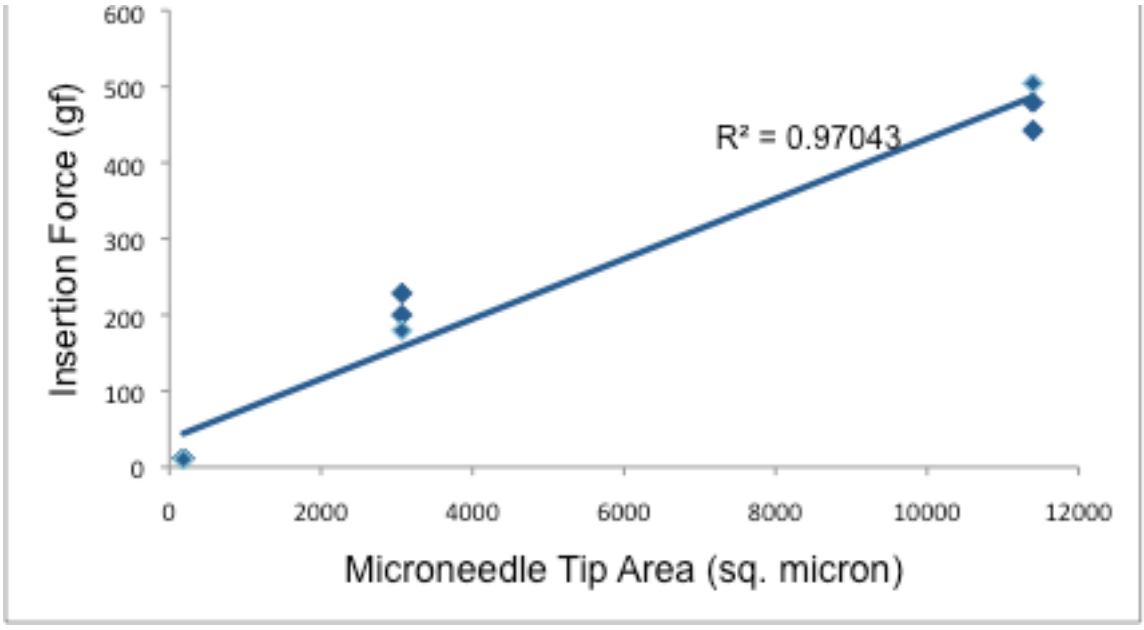

Figure 34: Dependence of insertion force on microneedle tip area

5.4.1 Analysis of Results From Variation of Tip Geometry

It is observed that when insertion force is high, the needles penetrate almost instantly. This is seen as a vertical drop in force at instant of insertion in Figure 30. However, as the insertion force reduces, the force drop becomes more gradual, as seen in Figure 32. The force drop is most gradual when the insertion force is lowest, as in the case of 'very sharp' needles, and is seen in Figure 33. This shows that after the stratum corneum ruptures, the needles penetrate smoothly and relatively slowly into the lower epidermis when the penetration force is low. This is as opposed to a much faster, almost instant penetration when the insertion force is high.

It should also be mentioned that all needles might not be penetrating at the same instant. Although care was taken to align the needles along a plane parallel to the skin surface, there might be slight staggering of the needle tips. Thus, at soon as one needle

enters, the other would follow close behind; a mechanism that might only be quantified with equipment of higher resolution.

5.4.2 Calculation of Skin Toughness

It has been postulated that when the energy delivered to the skin exceeds the energy needed to create a tear in the skin, the needle inserts into skin [94]. A similar approach was used by Pereira et. al. [144] to model tears into skin initiated and propagated with scissors.

The work input, is related to the change in potential energy between unaltered skin and the skin just prior to needle penetration.

Therefore, $\delta W = \int F \, dx$, where F is the force applied by the needle, x is the axial position of the needle, and the boundaries of integration are from the point of needle contact with the skin to the point of needle insertion.

The fracture toughness of the skin (G_p) depends on the interface area between the needles and the skin, and the total work input.

Therefore, $\int_{x=0}^{x=x_i} F dx = G_p A$,

where G_p is the puncture fracture toughness and xi is the displacement where insertion occurs. The left-had side of the equation, i.e. the potential energy, was calculated as the area under the load versus displacement curve before penetration.

From the area under the curve for the ‘less sharp’, ‘sharp’ and ‘very sharp’ needles, the fracture toughness of skin was calculated. The units were converted to the standard skin toughness unit kJ/N^2. The results are shown in Table 4.

Table 4: Skin toughness measured via each microneedle

Type of needle tip	Area under curve before point of penetration (gf μm)	Microneedle tip area	Skin toughness (kJ/m^2)
Very Sharp	489.5809	185.98	26.32
Sharp	8087.01	3068.04	26.35
Less Sharp	22351.18	11083.57	20.16

The value of skin toughness measured from these experiments are very close to the value of 30.1 kJ/m^2 reported by Davis et. al. and even closer to the value of 26.9 kJ/m^2 reported by Purslow et. al. [145].

5.5 Microneedle Fracture Strength Testing

It is imperative to know the fracture strength of microneedles in order to ascertain their physical limits. However, analytical analysis of beams does not translate to the micro-scale, and thus strength assumptions cannot be made. Needle failure due to axial loads may be due to heterogeneous peak stresses within the bulk material. Usually these peak stresses are the cause of needle failure, and fracture or buckling equations based on homogeneity of the material consistently over-estimate the strength of needles [94].

In order to test the microneedle strength, 200 micron tall needles were mounted onto a rigid aluminum block whose movement could be controlled via micromotor

actuators. A 0.5 mm wide stainless steel post was attached to another aluminum block, which was in turn mounted on the load cell.

By visual monitoring, the steel post was aligned axially along individual microneedles, one at a time. The microneedle being tested was pressed against the steel post at a rate of 50 microns/minute. Force and distance data was recorded along with a video of the needle collapse.

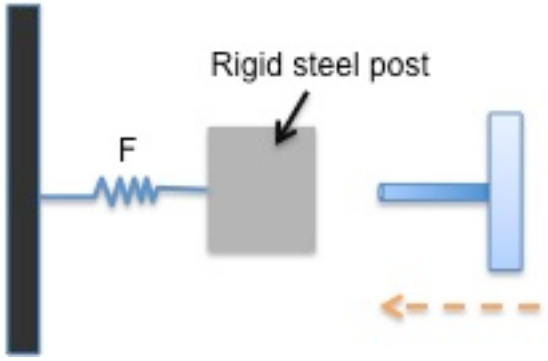

Figure 35: Schematic of axial fracture test setup

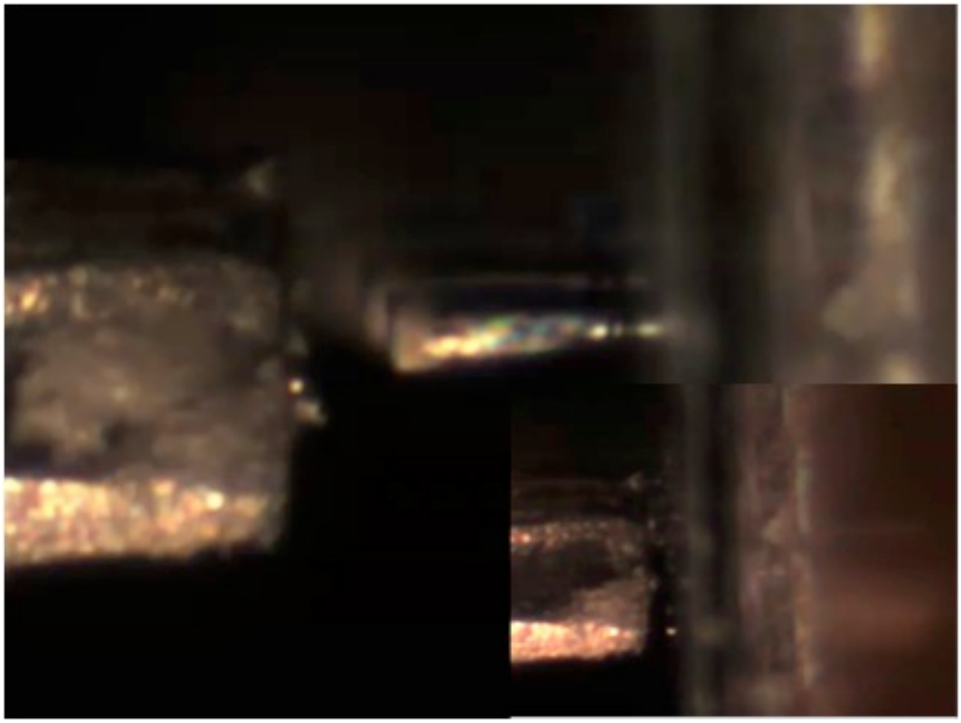

Figure 36: Microneedle aligned with steel post for axial testing. Inset: Microneedle completely collapses with no stub remaining

Axial fracture testing was done on 36 gauge hollow silicon microneedles. The microneedle is seen to collapse completely at its critical load. There was no bending of the needle observed. Also needles collapse completely from the base, with no stub remaining. Figure 36 shows a microneedle aligned axially with the steel post. Figure 37 shows the fracture force obtained, which is the peak incident force. The graph has slight non-linearity seen during rise in the incident force. This is probably due to slight inadvertent slippage of the needle over the steel post, or due to minimal buckling of the needle itself. Due to low precision of the visual monitoring setup, it is not possible to resolve any slippage or buckling of the needle. However, the setup is adequately suitable to ascertain the peak incident force, which is the parameter of interest.

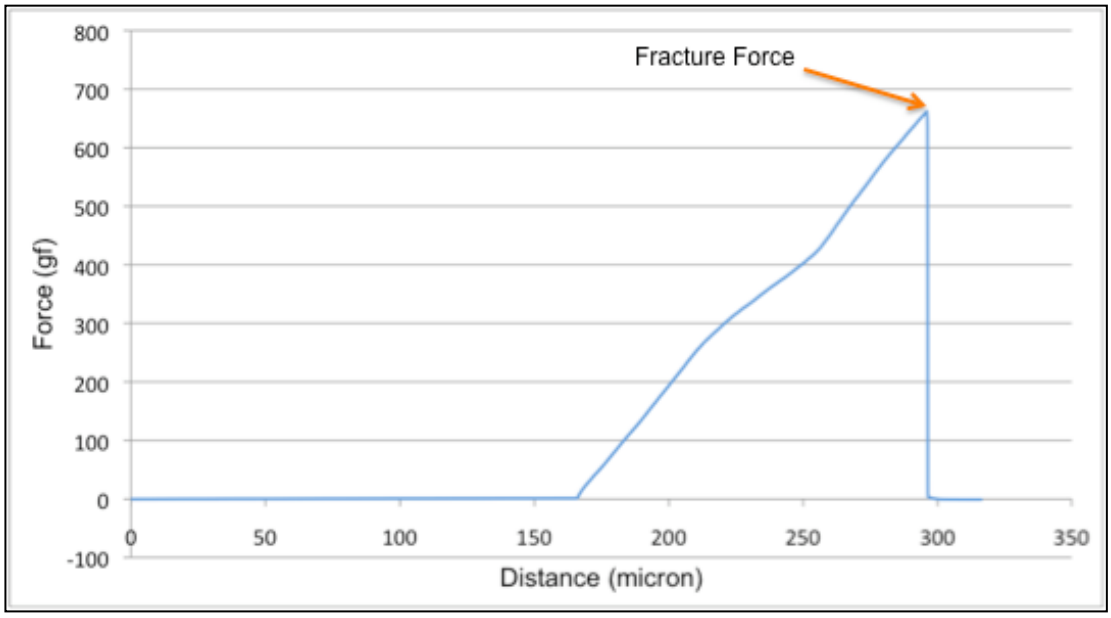

Figure 37: Axial fracture test on 36 gauge microneedle

Table 5 shows the results of the axial fracture tests. The axial strength of the smallest fabricated needles was at the upper range of the load cell failure rating. The 35 gauge needles were also tried, but did not fracture within the load cell usage limit. Strength testing on the 33 and 34 gauge needles was not attempted since their strength rating was expected to be much higher.

Table 5: Axial fracture strength of silicon needles

	Axial Fracture Strength (gf)		
Test no.	36-gauge needle	35 gauge needle	33 and 34 gauge
1	661.85	Out of range	Test not performed
2	874.47	Out of range	
3	682.49	Out of range	
Mean	739.6	N/A	N/A

5.6 Shear Fracture Testing

The shear fracture strength of microneedles has not been reported. Microneedle usage involves stresses related to the non-uniformity of skin contour, inadvertent slippage during insertion or removal, and reasonable human movements during period of penetration. These cause lateral forces to be applied on the needles. Breakage due to shear is a common cause of needle failure. In these tests, shear strength of needles was measured by aligning the needles perpendicular to the steel post used in the axial load testing. The steel post was pushed against the microneedle tips at the speed of 50 microns/minute. Care was taken to align the post as high as possible for successful needle breakage. This is because the measured shear force increases if the point of lateral force is lowered. Tests were done on multiple needles within each array, till reliable results were obtained. All the test needles were 200 micron long with a blunt tip and varied only in their gauge sizes. The experiments were captured on video.

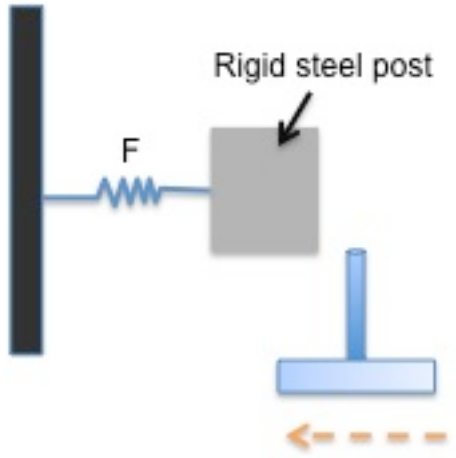

Figure 38: Schematic of shear fracture test setup

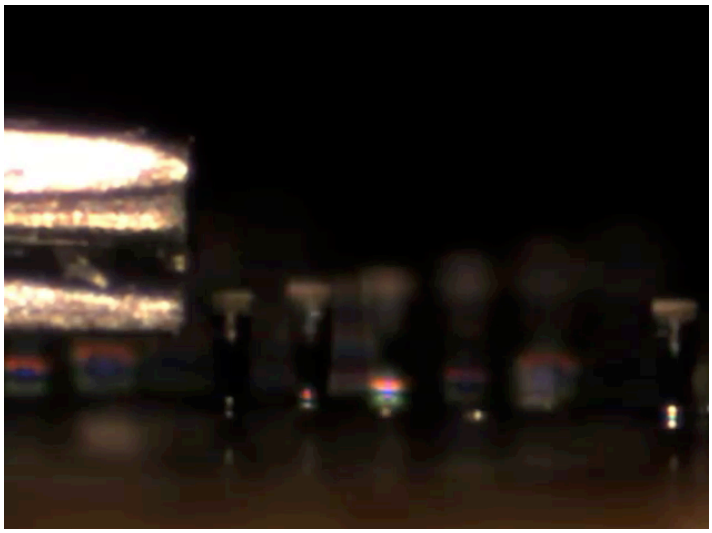

Figure 39: Steel post aligned perpendicular to silicon microneedle for shear strength testing

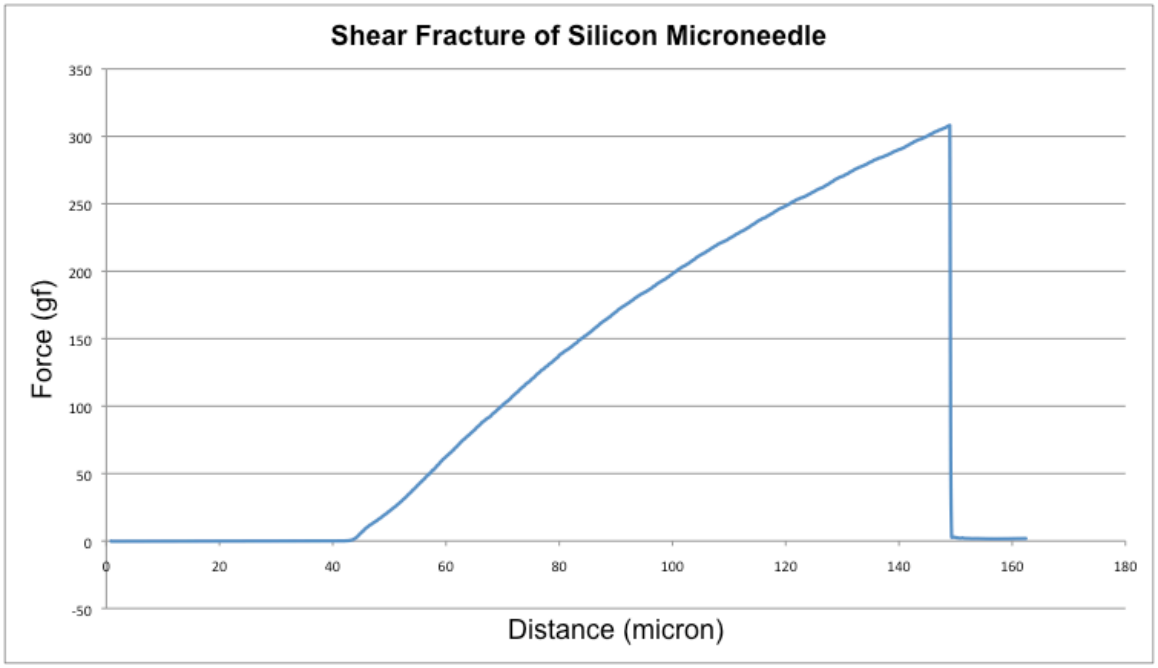

Figure 40: Shear fracture test on 33 gauge microneedle

Graphs were plotted for each of the shear tests. Figure 40 shows a typical plot of shear fracture tests. The point of force drop represents the instant when the needle breaks. The results of shear testing are shown in Table 6.

Table 6: Axial fracture strength of silicon needles

	Shear Fracture Strength (gf)			
Test no.	33 gauge needle	34 gauge needle	35 gauge needle	36 gauge needle
1	262.18	186.9	84.98	36.77
2	255.44	199.68	84.59	38.29
3	308.05	170.42	70.14	31.77
Mean	275.22	185.67	79.9	35.6

The variation of shear force for different needle dimensions is shown in Figure 41.

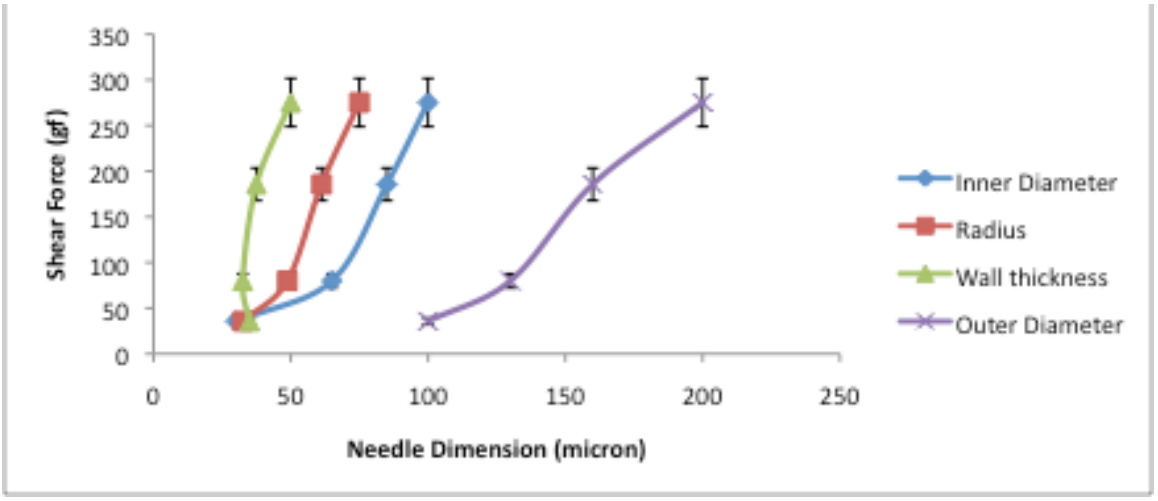

Figure 41: Shear force variation for various needle dimensions

CHAPTER 6

SILICON DIOXIDE MICRONEEDLES

Silicon Dioxide needles were fabricated in order to explore their use for drug delivery or extraction of biofluids. Two types of microneedle lumen shapes were investigated – circular and square. Both types of microneedles were fabricated to have 0.8 to 1 micron sidewall thickness and 100 to 120 micron height. The circular microneedles had 50 micron diameter, while square microneedles had 50 micron edge length.

Traditional fabrication methodologies employ lapping of bulk silicon, which dramatically reduce the obtainable length of microneedles. Also, lapping is a harsh process, and usually results in an uneven or sloping surface. This research involved fabrication of silicon dioxide microneedles using silicon nitride as an etch–stop layer for DRIE. The same nitride layer acts as an oxide barrier. This novel use of silicon nitride results in no loss of the bulk silicon.

6.1 Fabrication of Silicon Dioxide Microneedles

Fabrication of silicon dioxide microneedles was done using 400 micron silicon wafer. The process starts with deposition of PECVD silicon dioxide on top and PECVD silicon nitride on bottom. Patterning of top oxide layer is done to form holes. This is followed by DRIE etching of silicon. The bottom nitride layer acts as a DRIE etch-stop. Thermal oxidation of silicon wafer is done to form microneedle sidewalls. The bottom nitride layer acts as an oxidation barrier for the bottom side of the wafer. Wet etching of

bottom nitride using phosphoric acid (has high selectivity to oxide). Finally wet etching of silicon using TMAH is done to form out of plane silicon dioxide microneedles. Figure 42 depicts the fabrication process of silicon dioxide microneedles.

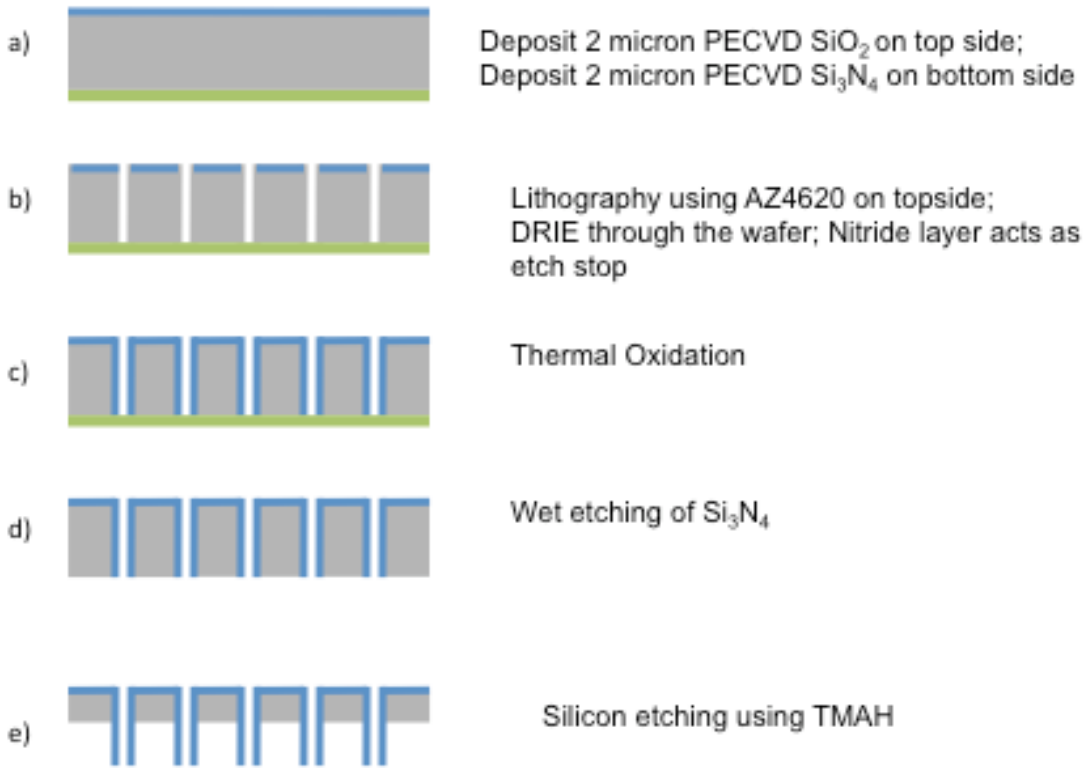

Figure 42: Fabrication process of Silicon Dioxide Microneedle

In this process it is critical for the silicon nitride to maintain integrity, otherwise a backside Helium leak occurs during DRIE, ceasing the process. During fabrication various nitride thickness were tried to achieve the desired result. Figure 43 shows a silicon nitride membrane holding up a silicon alignment marker.

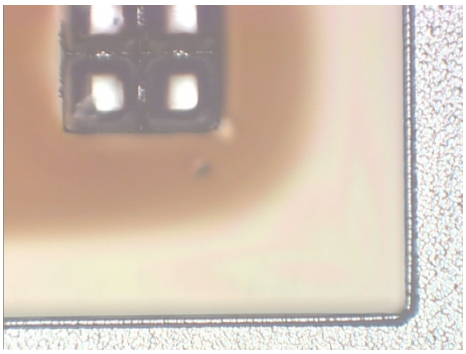

Figure 43: Silicon nitride membrane holding up a silicon alignment marker

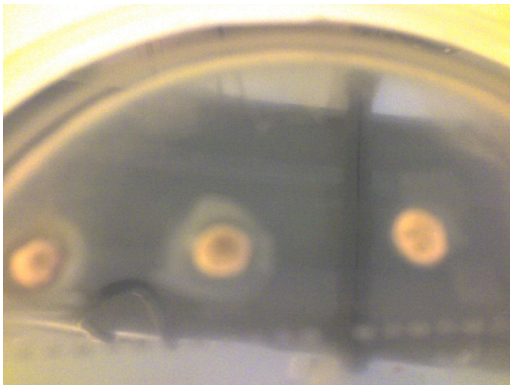

Figure 44: Ashing of photoresist over alignment markers

Due to loading effects in DRIE Bosch process larger areas get etched faster than the smaller holes. This caused the alignment windows to get etched through before the holes. Since this process does not require alignment, and the alignment markers in the alignment windows were superfluous, these areas were covered up by photoresist. However due to thermal effect the resist gets ashed. Finally, a polyimide tape was used to cover these areas. This tape is compatible with DRIE plasma processing, and holds up reliably during the dry etch.

Figure 45: Ashing of photoresist over alignment markers

6.1.1 Flaring of Microneedle Tips

It was found that the fabricated microneedles flared at the tips. This result is due to the 'notching effect' in DRIE. This is a well established undesirable effect in some DRIE machine. When a dielectric etch-stop region is reached during DRIE, charge accumulation takes place locally. This causes the impinging ions to deflect sideways. Thus notching in the end region takes place. This effect has been widely studied, and many modern machines employ special processes that do not result in this effect. The machine used for this fabrication (Alcatel AMS 100 SDE) does not include the company's 'HRM' capability that removes this effect.

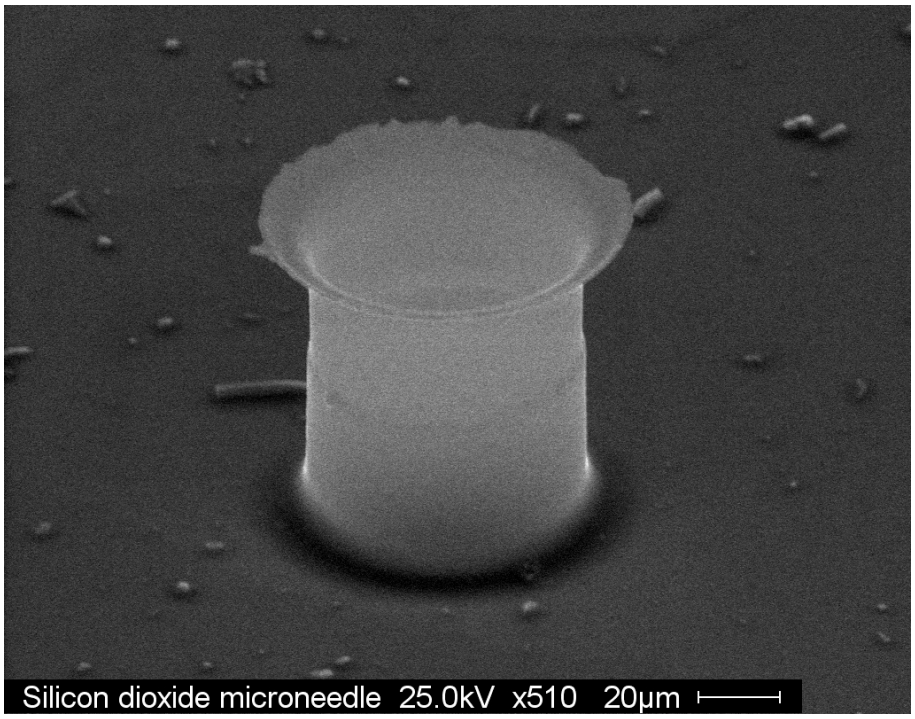

Figure 46: Flaring at the tip of silicon dioxide microneedle

In order to remove the flare, a slight CMP step was employed prior to TMAH based silicon etching. The wafer was etched back to approximately 2-3 micron. After, CMP it was observed that the flares were removed as required.

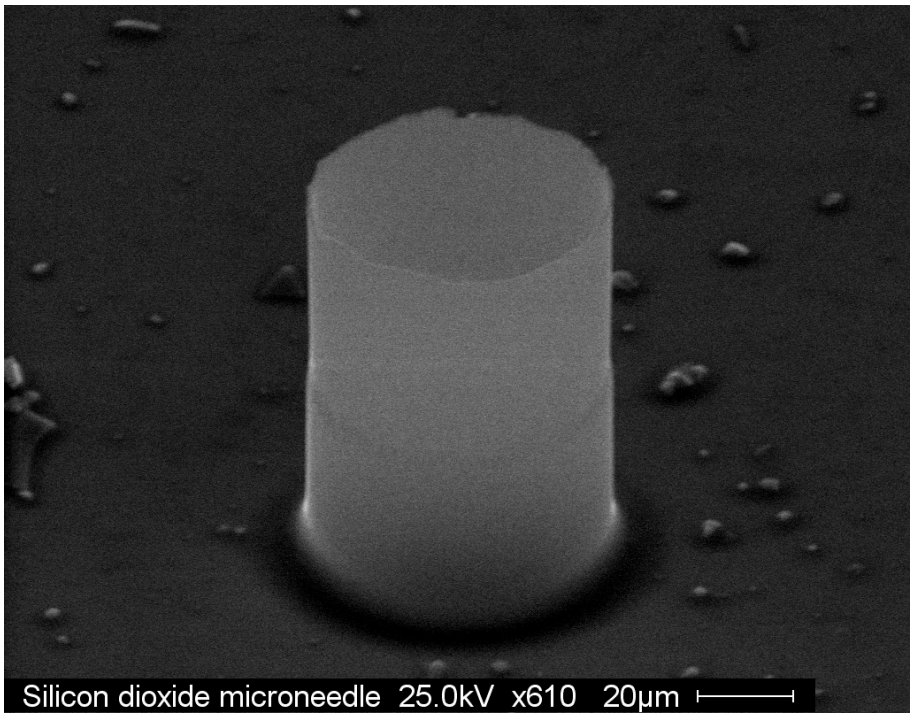

Figure 47: Circular silicon dioxide microneedle

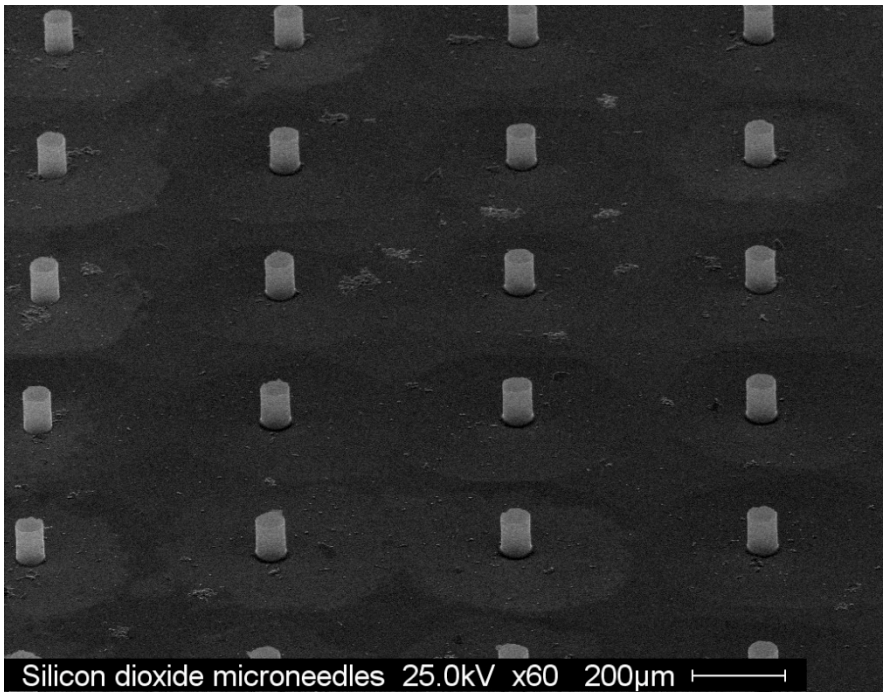

Figure 48: Array of silicon dioxide microneedles

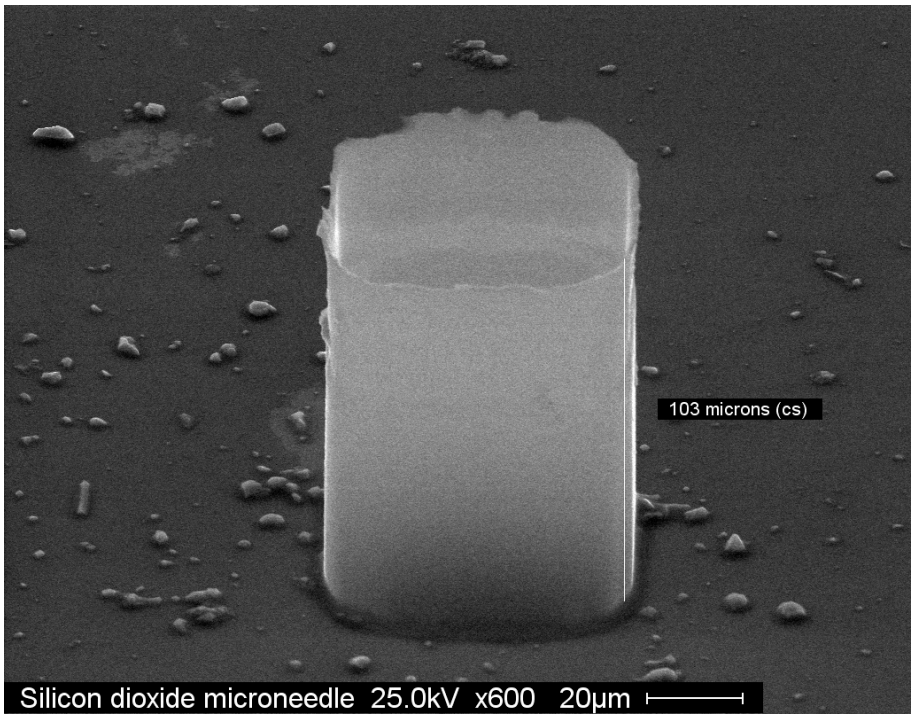

Figure 49: Square silicon dioxide microneedle

6.2 Skin Penetration Testing of Microneedles Into Human Skin

Penetration force testing of microneedles was done on cadaver skin. The setup was same as that used for silicon needle insertion tests. For the oxide needles, a 15 x15 array of the needles was used. No clear drop in force was seen as that observed in silicon needles. This is because the needle tip area for oxide needles is extremely small. Thus the penetration is expected to happen with just a few gram-force. Due to irregularities of the skin surface, the plot of force obtained is a bit noisy at the low end. Even though a few instances can be interpreted as needle insertion, distinguishing them from noise cannot be certain. Thus the insertion force could not be tabulated.

Visual inspection of the needles through a camera showed that the needles were clearly intact during insertion. Multiple insertion and retrieval did not result in breakage of the needles. Faint images of the needles are seen through the microscope are circled in Figure 50.

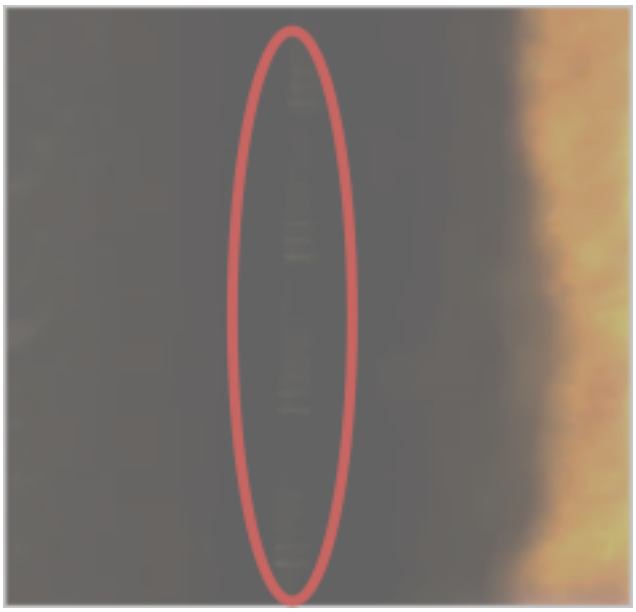

Figure 50: Insertion of oxide microneedles into skin.

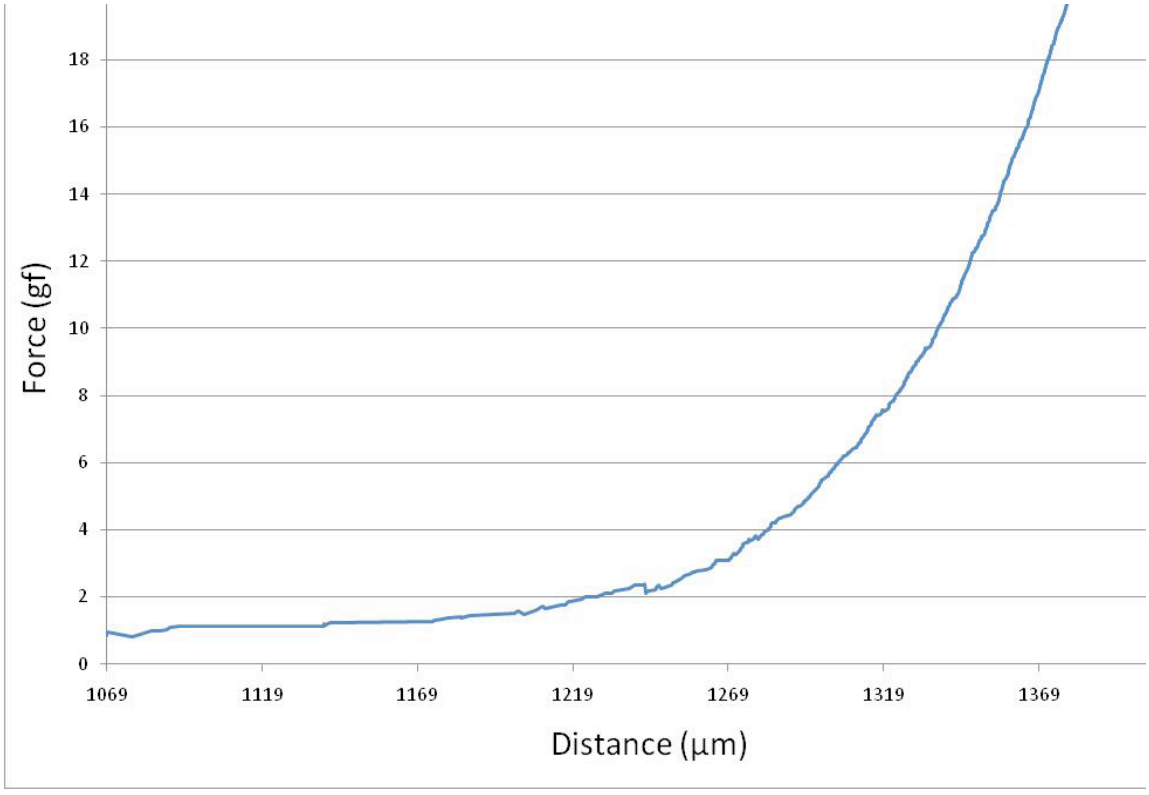

Figure 51: Skin penetration force of oxide needles

Since, no reliable force date was obtained, in order to verify successful insertion; as opposed to mere indentation), the needles were manually inserted into human cadaver skin. Green tattoo dye was smeared at the back end of the needle arrays. The dye gets transported through the needles via capillary forces. Histology of the skin samples was performed to observe for breakages in the Stratum corneum. The skin was fixed in 10% neutral buffered formalin, processed (standard processing) and embedded in paraffin for sectioning and hematoxylin and eosin (H&E) staining. Figure 50 depicts successful penetration of the needles. Green tattoo dye indicates successful penetration of needles through the stratum corneum and part of epidermis.

To depict penetration of the entire array of needles, Photomicrographs were taken of the length of the skin section (overlapping sections), and were merged using PhotoShop Elements 6 (photomerge option) to piece together the entire length of skin.

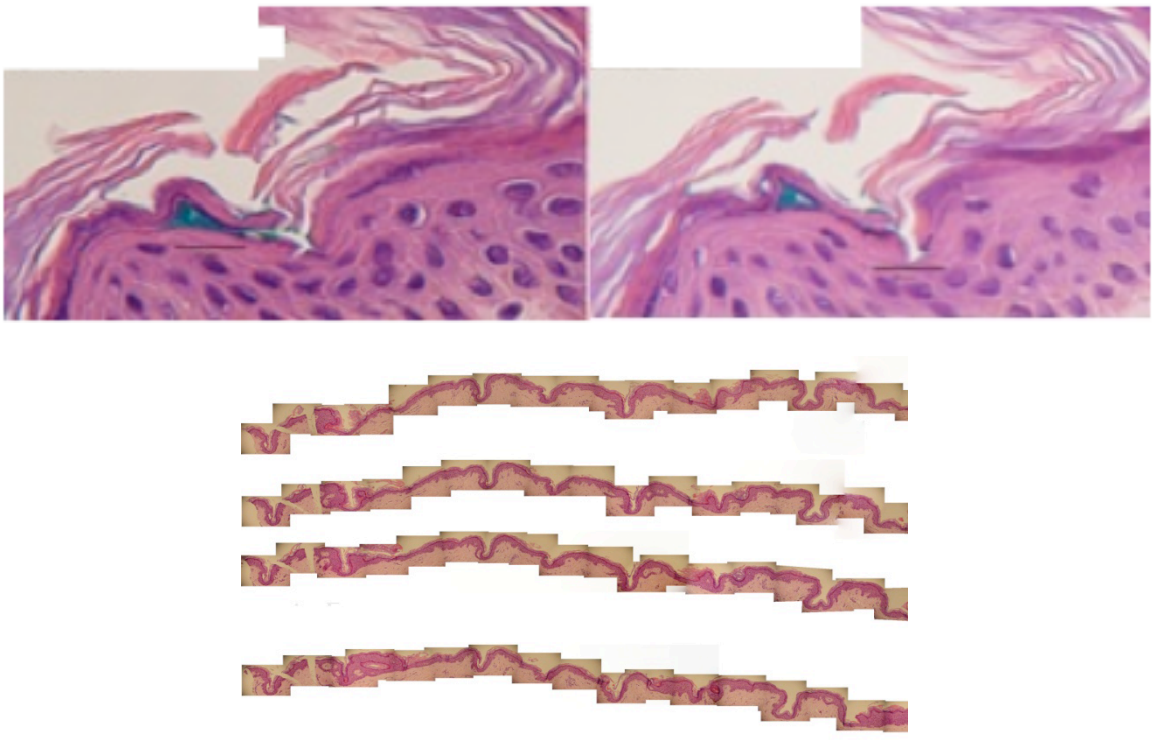

Figure 52: Post penetration histology on human skin

6.3 Fracture Strength Testing

Axial force testing was done using a similar setup for silicon needles. It was observed that as opposed to silicon needles, the oxide needles did not collapse instantly. Rather, in many cases, the needle broke a small part at a time, and in effect was ground slowly to its base. This effect can be observed as multiple spikes in the axial fracture force data.

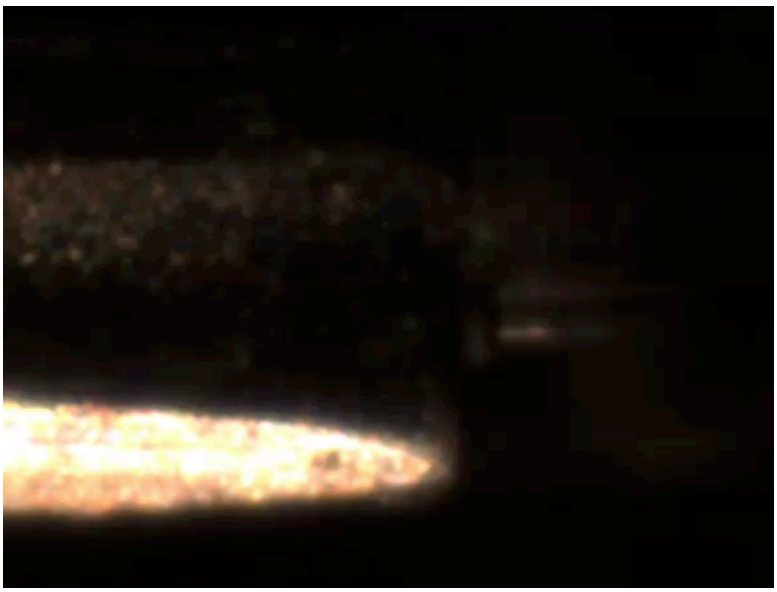

Figure 53: Axial fracture testing of oxide needles

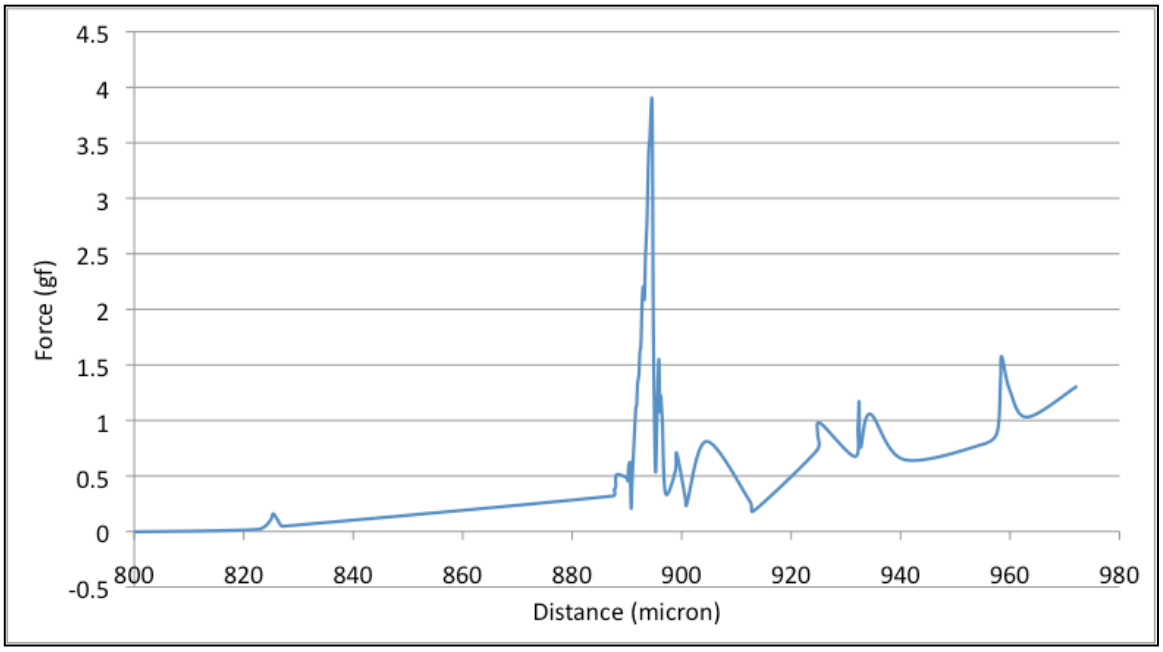

Figure 54: Axial fracture strength of circular needles

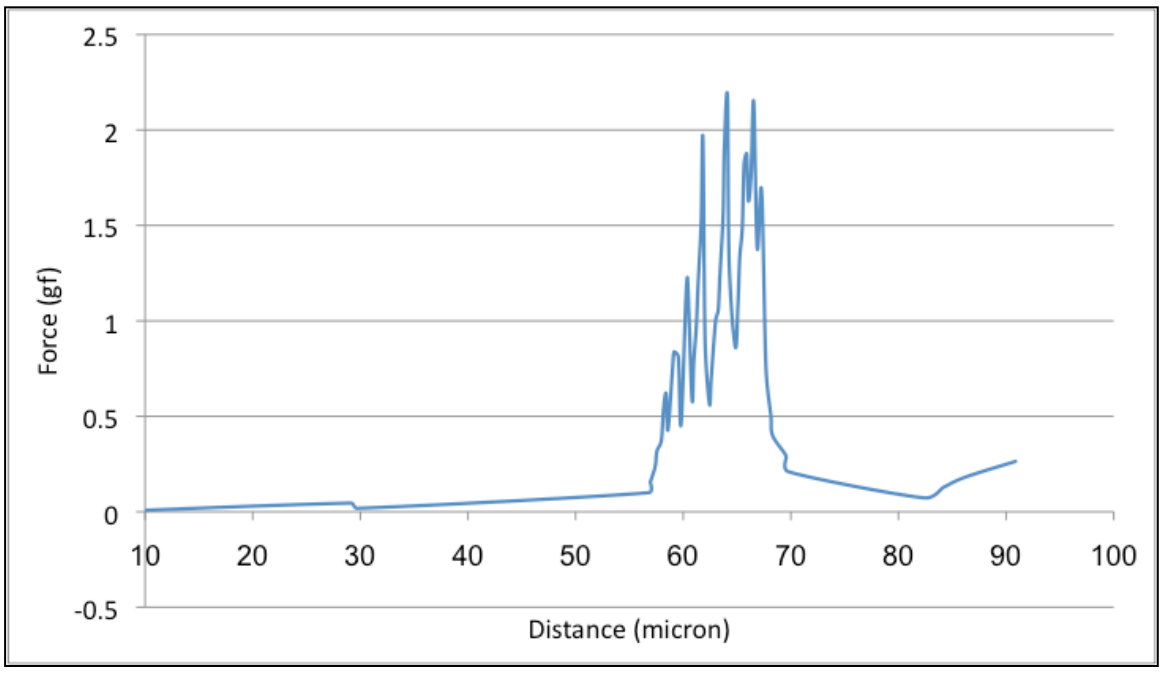

Figure 55: Axial fracture strength of square needles

The axial fracture force of circular needles was found to be slightly higher than the square ones. This is similar to critical loading on circular versus square hollow metallic beams. There too, the circular beams buckle later than the square ones. However, the equations for buckling cannot be translated to microneedles as needles failure is due to fracture because of peak stresses, rather than buckling.

Table 7: Axial fracture strength of silicon dioxide needles

	Axial Fracture Strength (gf)	
Test no.	Circular needles	Square needles
1	2.5	2.17
2	3.86	2.08
3	3.1	2.00
Mean	3.15	2.08

6.4 Shear Fracture Testing

Shear fracture of oxide microneedles was tested. The needles are so small as compared to their silicon counterparts, all force data was seen as spikes rather than a gradual rise in force. In one test it was possible to break multiple needles in a single motion of the steel rod. In that case, spikes could be observed at the interval of 1000 microns, which corresponded to the array pitch.

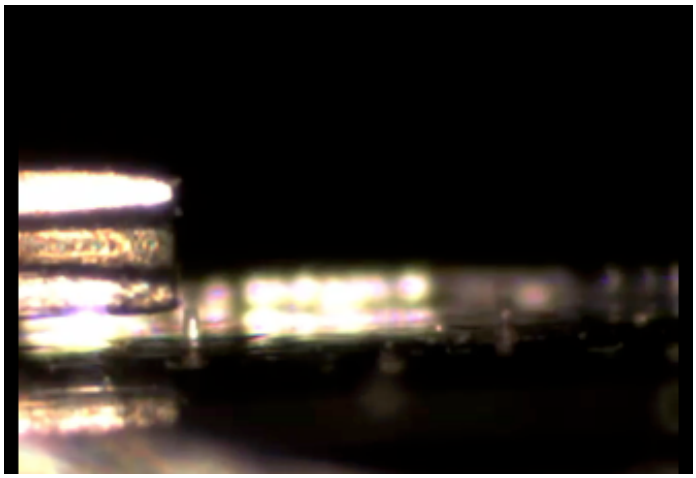

Figure 56: Shear fracture strength of oxide needles

Table 8: Shear fracture strength of silicon dioxide needles

Test no.	Shear Fracture Strength (gf)	
	Circular needles	Square needles
1	2.14	0.5
2	2.25	0.6
3	2.05	0.9
4	2.40	0.6
Mean	2.21	0.65

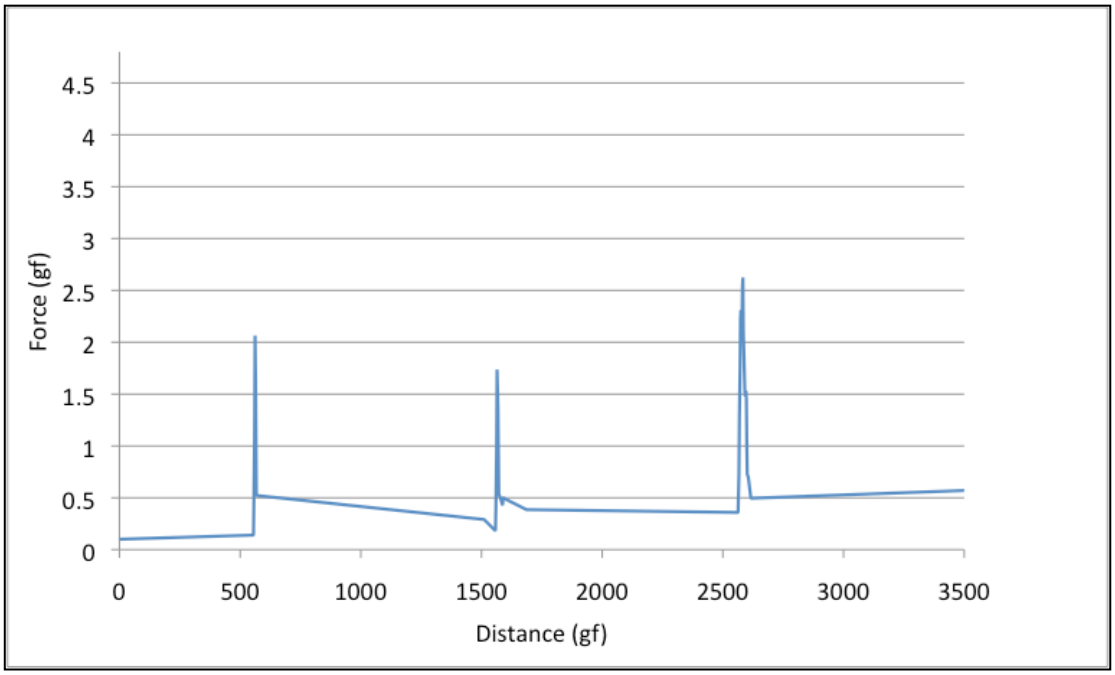

Figure 57: Shear fracture strength of circular needles

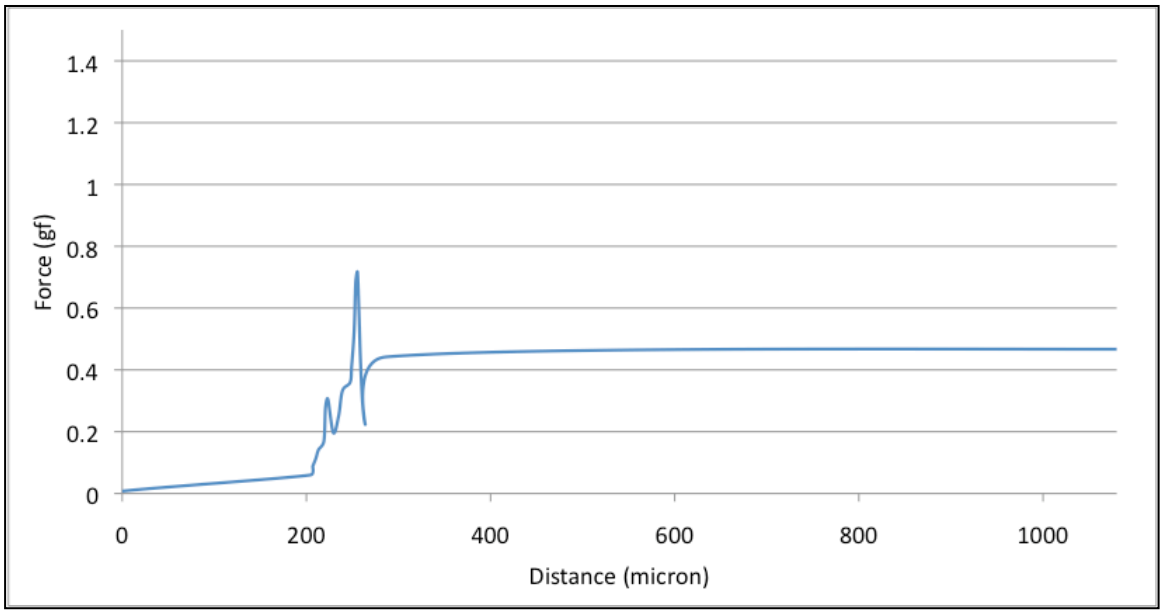

Figure 58: Shear fracture strength of square needles

It was observed that even though square needles had only slightly lower axial fracture strength, their shear fracture strength was a order of magnitude lower.

6.4.1 Analysis of Silicon Dioxide Needle Fracture Results

The results of the axial fracture tests on the oxide needles show that the square needles fracture much more easily as compared to the circular needles. This result is expected as even in the 'macro' domain, the critical loading limits of circular posts is much higher than those of square posts. However, the fabricated structures cannot be assumed to be simple vertical hollow posts with uniform sidewall thicknesses. Retardation of oxidation at sharp corners plays a very important role. Oxidation does not take place uniformly in 2-D structures. The thickness of oxide obtained is much lower around sharp corners, and the effect is even more pronounced in the case of concave corners [146]; as are present in our fabrication process.

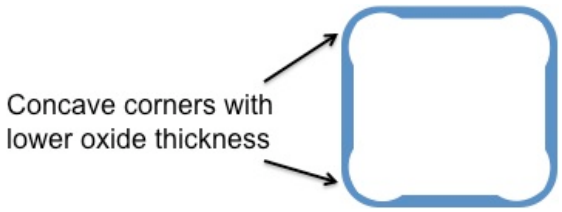

Figure 59: Oxidation retardation in square microneedles

Figure 59 shows a sketch of the oxidation retardation effect, in the case of square microneedles. Due to this effect, the structural integrity of a square microneedle is even lower than what can be expected from a needle having homogeneous sidewall thickness. The much lower shear fracture strength of oxide microneedles can be attributed to this effect.

CHAPTER 7

FUTURE WORK AND CONCLUSION

7.1 Future Work

7.1.1 Extraction of Interstitial Fluid From Human Cadaver Skin

Research needs to be done to fill the gap in scientific literature regarding interstitial fluid withdrawal using microneedle arrays. Microneedle arrays need to be packaged and used in conjunction with a pump to extract biofluids from skin. The setup can employ a Franz cell with cadaver skin as a membrane. Any colored liquid of low viscosity may be used for initial tests.

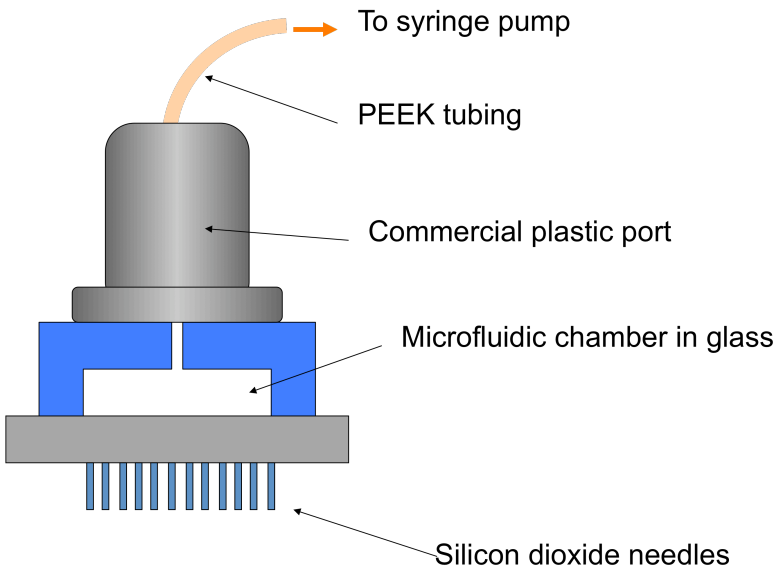

Figure 60: Packaged microneedles for fluid extraction

The needle array will have to be bonded to a glass microfluidic chamber at the back end. The chamber would in turn be connected via PEEK microfluidic tubing to a syringe pump. Interstitial fluid may be withdrawn from human skin using the syringe pump and flow rates can be determined. A study can analyze the effect of microneedle shape, microneedle diameter, array size and array pitch on the flow rates.

7.1.2 Optimization of DRIE Etching to Increase Oxide Needle Strength

DRIE process is essentially an accrual of a small isotropic etch in every Bosch cycle resulting in an overall anisotropic etch. The isotropic etches result in sidewall roughness, also known as scalloping effect. Figure 61 shows the SEM of a DRIE trench clearly showing the scalloping of sidewalls. This feature, in effect, provides fracture points for microneedles. By reducing the sidewall roughness, microneedle robustness can be greatly increased. The research task can focus on changing the Bosch recipe in the DRIE process to achieve greater sidewall smoothness.

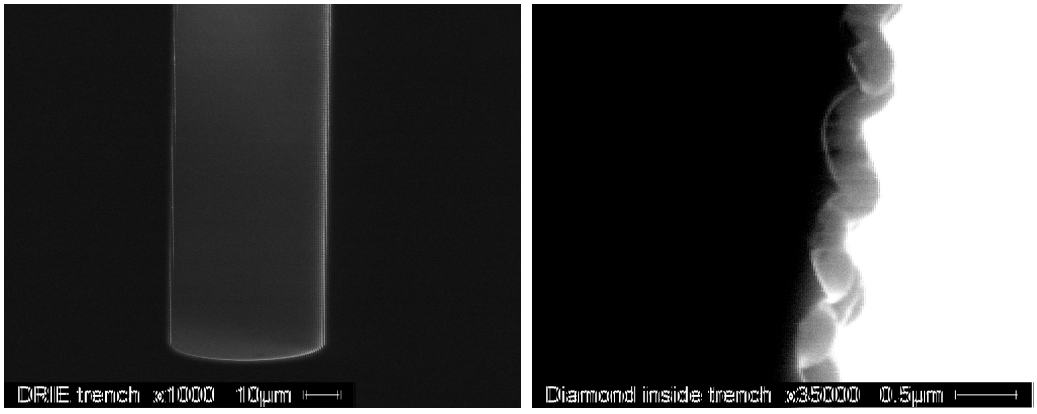

Figure 61: DRIE trench depicting scalloping effect

7.2 Conclusion

In this research, the geometry of silicon microneedles has been varied via DRIE processing to yield sharpened tips. Sharpening of microneedle tips provides reduced skin insertion force without compromising structural strength. Variation of skin insertion force of microneedles with change in tip sharpness has been studied, and toughness of human skin derived to be approximately 26 kJ/m^2. The axial and shear fracture limits of the microneedles have also been studied. Axial fracture of 36 gauge silicon needles takes place at an average force of 740gf. Shear fracture force of silicon needles varies from 275gf (33 gauge needles) to 35.6gf (36 gauge needles). Fracture limits of circular and square shaped silicon dioxide needles show reduced strength of square needles; which is pronounced in the case of shear fracture.

Skin interaction systems containing bio-engineered interfaces will revolutionize the biomedical industry in the coming decades. They promise exceptional capabilities in diverse transdermal diagnostic and therapeutic applications. Next generation therapeutic methods using advances in genomics, proteomics, pharmacogenomics etc., will all benefit from to the capabilities provided by these micro-components. Development of customized instrumentation will enable real-time electrical, mechanical and electrochemical measurements on the skin surface and also provide novel methods of drug delivery. Micromachined needles form the technological foundation for bio-engineered skin interfaces. These enabling components will be a common denominator in design of human interface lab-on-a-chip systems.

It is evident that microfluidic approaches to diagnosis and therapeutics offer multifaceted advantages over their conventional counterparts. However, successful clinical implementation of such systems would entail overcoming numerous challenges in areas of design, fabrication, electronics integration, deployment, testing, and data interpretation among many others. The interdependencies between the various design

variables and the obtained characteristics are highly complex, and warrant multidisciplinary research initiatives. Optimum utilization of this technology depends upon our capacity to identify and resolve, qualitatively and quantitatively, the various parametric entities involved.

REFERENCES

1. Terry, S., *A gas chromatography system fabricated on a silicon wafer using integrated circuit technology.* Ph. D. Thesis Stanford Univ., CA., 1975.

2. Harrison, D., et al., *Micromachining a miniaturized capillary electrophoresis-based chemical analysis system on a chip.* Science, 1993. 261(5123): p. 895-897.

3. Jacobson, S., et al., *High-speed separations on a microchip.* Anal. Chem, 1994. 66(7): p. 1114-1118.

4. Rasmussen, A., et al., *Simulation and optimization of a microfluidic flow sensor.* Sensors & Actuators: A. Physical, 2001. 88(2): p. 121-132.

5. Rasmussen, A. and M. Zaghloul. *The design and fabrication of microfluidic flow sensors*. 1999.

6. Andersson, H., et al., *A valve-less diffuser micropump for microfluidic analytical systems.* Sensors & Actuators: B. Chemical, 2001. 72(3): p. 259-265.

7. Nguyen, N. and T. Truong, *A fully polymeric micropump with piezoelectric actuator.* Sensors & Actuators: B. Chemical, 2004. 97(1): p. 137-143.

8. Liu, R., Q. Yu, and D. Beebe, *Fabrication and characterization of hydrogel-based microvalves.* Microelectromechanical Systems, Journal of, 2002. 11(1): p. 45-53.

9. Young, A., T. Bloomstein, and S. Palmacci, *Contoured elastic-membrane microvalves for microfluidic network integration.* Journal of biomechanical engineering, 1999. 121: p. 2.

10. Burbaum, J. and N. Sigal, *New technologies for high-throughput screening.* Current Opinion in Chemical Biology, 1997. 1(1): p. 72-78.

11. Zheng, B., L. Roach, and R. Ismagilov, *Screening of protein crystallization conditions on a microfluidic chip using nanoliter-size droplets.* JOURNAL-AMERICAN CHEMICAL SOCIETY, 2003. 125(37): p. 11170-11171.

12. Roberge, D., et al., *Microreactor technology: A revolution for the fine chemical and pharmaceutical industries?* Chemical Engineering & Technology, 2005. 28(3): p. 318-323.

13. Bilitewski, U., et al., *Biochemical analysis with microfluidic systems.* Analytical and bioanalytical chemistry, 2003. 377(3): p. 556-569.

14. Shaikh, K., et al., *A modular microfluidic architecture for integrated biochemical analysis.* Proceedings of the National Academy of Sciences, 2005. 102(28): p. 9745-9750.

15. Marle, L. and G. Greenway, *Microfluidic devices for environmental monitoring.* Trends in Analytical Chemistry, 2005. 24(9): p. 795-802.

16. Sequeira, M., et al., *Towards autonomous environmental monitoring systems.* Talanta, 2002. 56(2): p. 355-363.

17. Madou, M., et al., *Design and fabrication of CD-like microfluidic platforms for diagnostics: microfluidic functions.* Biomedical Microdevices, 2001. 3(3): p. 245-254.

18. Yager, P., et al., *Microfluidic diagnostic technologies for global public health.* Nature, 2006. 442: p. 412-418.

19. Andersson, H. and A. Van den Berg, *Microfluidic devices for cellomics: a review.* Sensors & Actuators: B. Chemical, 2003. 92(3): p. 315-325.

20. Helene, A., *Lab-on chips for cellomics: micro & nanotechnologies for life science.*

21. Sanders, G. and A. Manz, *Chip-based microsystems for genomic and proteomic analysis.* Trends in Analytical Chemistry, 2000. 19(6): p. 364-378.

22. Lion, N., et al., *Microfluidic systems in proteomics.* Electrophoresis, 2003. 24(21).

23. Jain, K., *Applications of biochip and microarray systems in pharmacogenomics.* pgs, 2000. 1(3): p. 289-307.

24. Ahn, C., et al., *Disposable smart lab on a chip for point-of-care clinical diagnostics.* Proceedings of the IEEE, 2004. 92(1): p. 154-173.

25. Srinivasan, V., V. Pamula, and R. Fair, *An integrated digital microfluidic lab-on-a-chip for clinical diagnostics on human physiological fluids.* Lab on a Chip, 2004. 4(4): p. 310-315.

26. Daw, R. and J. Finkelstein, *Lab on a chip.* Nature, 2006. 442(7101): p. 367-367.

27. Erickson, D. and D. Li, *Integrated microfluidic devices.* Analytica Chimica Acta, 2004. 507(1): p. 11-26.

28. Lao, A., et al., *Precise temperature control of microfluidic chamber for gas and liquid phase reactions.* Sensors & Actuators: A. Physical, 2000. 84(1-2): p. 11-17.

29. Marentis, T., et al., *Microfluidic sonicator for real-time disruption of eukaryotic cells and bacterial spores for DNA analysis.* Ultrasound in Medicine & Biology, 2005. 31(9): p. 1265-1277.

30. Ko, J., et al., *A polymer-based microfluidic device for immunosensing biochips.* Lab on a Chip, 2003. 3(2): p. 106-113.

31. McDonald, J. and G. Whitesides, *Poly (dimethylsiloxane) as a material for fabricating microfluidic devices.* Accounts of chemical research, 2002. 35(7): p. 491-500.

32. Quake, S. and A. Scherer, *From micro-to nanofabrication with soft materials.* Science, 2000. 290(5496): p. 1536-1540.

33. Beebe, D., et al., *Functional hydrogel structures for autonomous flow control inside microfluidic channels.* Nature a-z index, 2000. 404(6778): p. 588-590.

34. Eteshola, E. and D. Leckband, *Development and characterization of an ELISA assay in PDMS microfluidic channels.* Sensors & Actuators: B. Chemical, 2001. 72(2): p. 129-133.

35. Bhansali, S., H. Thurman Henderson, and S. Hoath, *Probing human skin as an information-rich smart biological interface using MEMS sensors.* Microelectronics Journal, 2002. 33(1-2): p. 121-127.

36. Gascoyne, P., J. Satayavivad, and M. Ruchirawat, *Microfluidic approaches to malaria detection.* Acta tropica, 2004. 89(3): p. 357-369.

37. Wolf, M., et al., *Simultaneous detection of C-reactive protein and other cardiac markers in human plasma using micromosaic immunoassays and self-regulating microfluidic networks.* Biosensors and Bioelectronics, 2004. 19(10): p. 1193-1202.

38. Chung, Y., et al., *Microfluidic chip for high efficiency DNA extraction.* Lab on a Chip, 2004. 4(2): p. 141-147.

39. Yeung, S. and I. Hsing, *Manipulation and extraction of genomic DNA from cell lysate by functionalized magnetic particles for lab on a chip applications.* Biosensors and Bioelectronics, 2006. 21(7): p. 989-997.

40. Gattiker, G., K. Kaler, and M. Mintchev, *Electronic Mosquito: designing a semi-invasive Microsystem for blood sampling, analysis and drug delivery applications.* Microsystem Technologies, 2005. 12(1): p. 44-51.

41. Newman, J. and A. Turner, *Home blood glucose biosensors: a commercial perspective.* Biosensors and Bioelectronics, 2005. 20(12): p. 2435-2453.

42. Tsuchiya, K., et al., *Development of blood extraction system for health monitoring system.* Biomedical Microdevices, 2005. 7(4): p. 347-353.

43. Ertl, P., et al., *Development of a Lab-on-a-Chip for the Characterization of Human Cells.*

44. Medoro, G., et al., *A lab-on-a-chip for cell detection and manipulation.* IEEE Sensors Journal, 2003. 3(3): p. 317-325.

45. Sabounchi, P., et al., *Sample concentration and impedance detection on a microfluidic polymer chip.* Biomedical Microdevices, 2008. 10(5): p. 661-670.

46. Khanna, P., et al., *Microneedle-Based Automated Therapy for Diabetes Mellitus.* Journal of Diabetes Science and Technology, 2008. 2(6): p. 1122-1129.

47. Zafar Razzacki, S., et al., *Integrated microsystems for controlled drug delivery.* Advanced Drug Delivery Reviews, 2004. 56(2): p. 185-198.

48. Dreher, F., et al., *Interaction of a lecithin microemulsion gel with human stratum corneum and its effect on transdermal transport.* Journal of Controlled Release, 1997. 45(2): p. 131-140.

49. Bashir, S., et al., *Physical and physiological effects of stratum corneum tape stripping.* Official Journal of International Society for Bioengineering and the Skin (ISBS) International Society for Digital Imaging of Skin (ISDIS) International Society for Skin Imaging (ISSI), 2001. 7(1): p. 40-48.

50. Marttin, E., et al., *A critical comparison of methods to quantify stratum corneum removed by tape stripping.* Skin pharmacology: the official journal of the Skin Pharmacology Society, 1996. 9(1): p. 69.

51. Gebhart, S., et al., *Glucose Sensing in Transdermal Body Fluid Collected Under Continuous Vacuum Pressure Via Micropores in the Stratum Corneum.* Diabetes Technology & Therapeutics, 2003. 5(2): p. 159-166.

52. Brazzle, J., I. Papautsky, and A. Frazier, *Micromachined needle arrays for drug delivery or fluid extraction.* IEEE Engineering in Medicine and Biology Magazine, 1999. 18(6): p. 53-58.

53. Kaushik, S., et al., *Lack of pain associated with microfabricated microneedles*. 2001, IARS. p. 502-504.

54. Elias, P.M., *The stratum corneum revisited.* J Dermatol, 1996. 23(11): p. 756-8.

55. Elias, P.M., *Stratum corneum architecture, metabolic activity and interactivity with subjacent cell layers.* Exp Dermatol, 1996. 5(4): p. 191-201.

56. Hoath, S.B., M.M. Donnelly, and R.E. Boissy, *Sensory transduction and the mammalian epidermis.* Biosens Bioelectron, 1990. 5(5): p. 351-66.

57. Kell, D., *The principles and potential of electrical admittance spectroscopy: an introduction.* Biosensors: fundamentals and applications, 1987: p. 427–468.

58. Nicander, I., et al., *Correlation of impedance response patterns to histological findings in irritant skin reactions induced by various surfactants.* British Journal of Dermatology, 1996. 134(2): p. 221.

59. Rawlings, A.V., et al., *Stratum corneum moisturization at the molecular level.* J Invest Dermatol, 1994. 103(5): p. 731-41.

60. Sinclair, B., *Everything's great when its sits on a chip - A bright future for DNA arrays.* Scientist, 1999. 13(11): p. 18-20.

61. *Structure of Skin*, in *Microsoft(r) Encarta(r) Encyclopedia*. (c) 2004 -2004, Microsoft Corporation. All Rights Reserved.

62. Swanson, J.R. *Epidermis*. 1996 [cited 2009 10 Feb]; Available from: <http://www.meddean.luc.edu/lumen/MedEd/medicine/dermatology/melton/skinlsn/epider.htm>.

63. Marks, R. and J.-L. Leveque, *The Essential Stratum Corneum: Introduction*: Martin Dunitz Ltd.

64. Fujii, T., *PDMS-based microfluidic devices for biomedical applications.* Microelectronic Engineering, 2002. 61: p. 907-914.

65. Konrad, R., et al., *Towards disposable lab-on-a-chip: poly (methylmethacrylate) microchip electrophoresis device with electrochemical detection.* Electrophoresis, 2002. 23: p. 596-601.

66. Johnson, T.J., D. Ross, and L.E. Locascio, *Rapid Microfluidic Mixing.* Analytical Chemistry, 2002. 74(1): p. 45-51.

67. Chandrasekaran, S. and A. Frazier, *Characterization of surface micromachined metallic microneedles.* Microelectromechanical Systems, Journal of, 2003. 12(3): p. 289-295.

68. Davis, S., et al., *Hollow metal microneedles for insulin delivery to diabetic rats.* IEEE Transactions on Biomedical Engineering, 2005. 52(5): p. 909-915.

69. Kim, K., et al., *A tapered hollow metallic microneedle array using backside exposure of SU-8.* Journal of Micromechanics and Microengineering, 2004. 14(4): p. 597-603.

70. Lee, S., W. Jeong, and D. Beebe, *Microfluidic valve with cored glass microneedle for microinjection.* Lab on a Chip, 2003. 3(3): p. 164-167.

71. Rajaraman, S. and H. Henderson, *A unique fabrication approach for microneedles using coherent porous silicon technology.* Sensors & Actuators: B. Chemical, 2005. 105(2): p. 443-448.

72. Rodriguez, A., et al., *Fabrication of silicon oxide microneedles from macroporous silicon.* Sensors & Actuators: B. Chemical, 2005. 109(1): p. 135-140.

73. Park, J., M. Allen, and M. Prausnitz, *Biodegradable polymer microneedles: fabrication, mechanics and transdermal drug delivery.* Journal of Controlled Release, 2005. 104(1): p. 51-66.

74. Park, J., M. Allen, and M. Prausnitz, *Polymer microneedles for controlled-release drug delivery.* Pharmaceutical Research, 2006. 23(5): p. 1008-1019.

75. Sung, J.-H., S.-J. Kim, and K.-H. Lee, *Fabrication of microcapacitors using conducting polymer microelectrodes.* Journal of Power Sources, 2003. 124(1): p. 343-350.

76. Gardeniers, H., et al., *Silicon micromachined hollow microneedles for transdermal liquid transport.* Microelectromechanical Systems, Journal of, 2003. 12(6): p. 855-862.

77. Paik, S., et al., *In-plane single-crystal-silicon microneedles for minimally invasive microfluid systems.* Sensors & Actuators: A. Physical, 2004. 114(2-3): p. 276-284.

78. Wilke, N., et al., *Silicon microneedle electrode array with temperature monitoring for electroporation.* Sensors & Actuators: A. Physical, 2005. 123: p. 319-325.

79. Wilke, N., et al., *Process optimization and characterization of silicon microneedles fabricated by wet etch technology.* Microelectronics Journal, 2005. 36(7): p. 650-656.

80. Chandrasekaran, S. and A.B. Frazier. *Mechanical Characterization of Surface Micromachined Hollow Metallic Microneedles*. in *IEEE EMBS Special Topic Conference on Microtechnologies in Medicine & Biology*. May 2002. Madison, WI.

81. Stoeber, B. and D. Liepmann, *Arrays of hollow out-of-plane microneedles for drug delivery.* Microelectromechanical Systems, Journal of, 2005. 14(3): p. 472-479.

82. Morrow, T., *Transdermal patches are more than skin deep.* Managed Care April 2004.

83. Marks, R. and J.-L. Leveque, *The Essential Stratum Corneum : Crossing the Barrier*: Martin Dunitz Ltd.

84. Stoeber, B. and D. Liepmann. *Fluid injection through out of plane micro needles*. in *1St annual international IEEE-EMBS, special topic conference on micro technologies in medicine and Biology*. 2000. LYON, France: IEEE.

85. D.V.McAllister, et al., *Micro Needles for Transdermal Delivery of Molecules.* IEEE 1999: p. 836.

86. J.G.E.Gardeniers, et al., *Silicon micro machined hollow micro needles for transdermal liquid transfer.* IEEE 2002: p. 141-144.

87. K.Liu, et al. *Electroplated micro needle array for BIO medical applications*. in *Proceedings of SPIE - The International Society for Optical Engineering*. 2001.

88. S.Henry, et al., *Micromachined Needles for the Transdermal Delivery of Drugs, .* IEEE 1998: p. 494-498.

89. Griss, P. and G. Stemme, *Novel, Side Opened Out-of-Plane Micro Needles For Microfluidic Transdermal Interfacing.* IEEE 2002: p. 467-470.

90. Brazzle, J., I. Papautsky, and A.B. Frazier., *Micro Machined Needle Array For Drug Delivery or Fluid Extraction.* IEEE, 1999: p. 53- 58.

91. D.Zahn, J., D. Trbotich, and D. Liepmann., *Microfabricated MicroDialysis Microneedles for Continuous Medical Monitoring.* IEEE 2000: p. 375-380.

92. V.McAllister, D., M. G.Allen, and M. R.Prausnitz., *Microfabricated MicroNeedles for Gene and Drug Delivery.* Annual Review of BioMedical Engg., 2000: p. 289-313.

93. Friedl, K.E., *Analysis: optimizing microneedles for epidermal access.* Diabetes Technol Ther, 2005. 7(3): p. 546-8.

94. Davis, S.P., et al., *Insertion of microneedles into skin: measurement and prediction of insertion force and needle fracture force.* Journal of Biomechanics, 2004. 37(8): p. 1155-1163.

95. Wijaya Martanto, S.M.B., Elizabeth A. Costner, Mark R. Prausnitz, Marc K. Smith,, *Fluid dynamics in conically tapered microneedles.* AIChE Journal, 2005. 51(6): p. 1599-1607.

96. Mukerjee, E., et al., *Microneedle array for transdermal biological fluid extraction and in situ analysis.* Sensors & Actuators: A. Physical, 2004. 114(2-3): p. 267-275.

97. Collison, M., et al., *Analytical characterization of electrochemical biosensor test strips for measurement of glucose in low-volume interstitial fluid samples.* Clinical Chemistry, 1999. 45(9): p. 1665-1673.

98. Wang, P., M. Cornwell, and M. Prausnitz, *Minimally invasive extraction of dermal interstitial fluid for glucose monitoring using microneedles.* Diabetes Technology & Therapeutics, 2005. 7(1): p. 131-141.

99. Brazzle, J., I. Papautsky, and A.B. Frazier, *Micromachined needle arrays for drug delivery or fluid extraction.* Engineering in Medicine and Biology Magazine, IEEE, 1999. 18(6): p. 53-58.

100. Moon, S. and S. Lee, *A novel fabrication method of a microneedle array using inclined deep x-ray exposure.* Journal of Micromechanics and Microengineering, 2005. 15(5): p. 903-911.

101. Martanto, W., et al., *Microinfusion using hollow microneedles.* Pharmaceutical Research, 2006. 23(1): p. 104-113.

102. Perennes, F., et al., *Sharp beveled tip hollow microneedle arrays fabricated by LIGA and 3D soft lithography with polyvinyl alcohol.* Journal of Micromechanics and Microengineering, 2006. 16(3): p. 473-479.

103. Griss, P. and G. Stemme, *Novel, Side Opened Out-of-Plane Micro Needles For Microfluidic Transdermal Interfacing.* IEEE, 2002: p. 467-470.

104. Zhang, P. and G. Jullien. *Microneedle arrays for drug delivery and fluid extraction*. 2005.

105. Zahn, J., et al., *Microfabricated polysilicon microneedles for minimally invasive biomedical devices.* Biomedical Microdevices, 2000. 2(4): p. 295-303.

106. Khanna, P., et al., *The Challenge of Human Skin - Engineering the Biotic/Abiotic Interface*, in *Smart Biosensor Technology*, G.K. Knopf and A.S. Bassi, Editors. 2007, CRC Press. p. 249-268.

107. Melin, J. and S. Quake, *Microfluidic large-scale integration: the evolution of design rules for biological automation.* 2007.

108. Nisisako, T. and T. Torii, *Microfluidic large-scale integration on a chip for mass production of monodisperse droplets and particles.* Lab on a Chip, 2008. 8(2): p. 287-293.

109. Spencer, V., et al., *Chromatin immunoprecipitation: a tool for studying histone acetylation and transcription factor binding.* Methods, 2003. 31(1): p. 67-75.

110. Wang, S., et al., *Optical properties of nano-crystalline diamond films deposited by MPECVD.* Optical Materials, 2003. 24(3): p. 509-514.

111. Müller, R., et al., *Elements for surface microfluidics in diamond.* Diamond & Related Materials, 2004. 13(4-8): p. 780-784.

112. Björkman, H., et al., *Diamond replicas from microstructured silicon masters.* Sensors & Actuators: A. Physical, 1999. 73(1-2): p. 24-29.

113. Guillaudeu, S., X. Zhu, and D.M. Aslam, *Fabrication of 2-[mu]m wide poly-crystalline diamond channels using silicon molds for micro-fluidic applications.* Diamond and Related Materials, 2003. 12(1): p. 65-69.

114. Massi, M., et al., *Plasma etching of DLC films for microfluidic channels.* Microelectronics Journal, 2003. 34(5-8): p. 635-638.

115. Hartl, A., et al., *Protein-modified nanocrystalline diamond thin films for biosensor applications.* Nat Mater, 2004. 3(10): p. 736-742.

116. Lasseter, T., et al. *8th International Conference on Applications of Diamond and Related Materials*. 2005.

117. Nebel, C., et al., *Photochemical attachment of amine linker molecules on hydrogen terminated diamond.* Diamond & Related Materials, 2006. 15(4-8): p. 1107-1112.

118. OkrÛj, W., et al., *Blood platelets in contact with nanocrystalline diamond surfaces.* Diamond and Related Materials, 2006. 15(10): p. 1535-1539.

119. Xu, Z., A. Kumar, and A. Kumar, *Amperometric detection of glucose using a modified nitrogen-doped nanocrystalline diamond electrode.* Journal of Bioscience and Nanotechnology, 2005. 1: p. 416-420.

120. Xu, Z., et al. *Synthesis and Characterization of Nanocrystalline Diamond Film and Its Biomedical Applications*. in *MRS Symposium Proceeding*. 2004.

121. Björkman, H., et al., *Diamond microchips for fast chromatography of proteins.* Sensors & Actuators: B. Chemical, 2001. 79(1): p. 71-77.

122. Christiaens, P., et al., *EDC-mediated DNA attachment to nanocrystalline CVD diamond films.* Biosensors and Bioelectronics, 2006. 22(2): p. 170-177.

123. Karczemska, A. and A. Sokolowska. *Wide Bandgap Layers, 2001. Abstract Book*. 2001.

124. Takahashi, K., et al., *DNA preservation using diamond chips.* Diamond & Related Materials, 2003. 12(3-7): p. 572-576.

125. Belgrader, P., et al., *A Minisonicator To Rapidly Disrupt Bacterial Spores for DNA Analysis.* Analytical Chemistry, 1999. 71(19): p. 4232-4236.

126. Mello, A.J.d. and N. Beard, *Dealing with real samples: sample pre-treatment in microfluidic systems.* Lab on a Chip, 2003. 3: p. 11N - 20N.

127. Dong Woo, L. and C. Young-Ho. *A Continuous Cell Lysis Device Using Focused High Electric Field and Self-Generated Electroosmotic Flow*. in *Micro Electro Mechanical Systems, 2006. MEMS 2006 Istanbul. 19th IEEE International Conference on*. 2006.

128. Lee, S.W., H. Yowanto, and Y.C. Tai. *A micro cell lysis device*. in *Micro Electro Mechanical Systems, 1998. MEMS 98. Proceedings., The Eleventh Annual International Workshop on*. 1998.

129. Kim, J., et al., *Cell lysis on a microfluidic CD (compact disc).* Lab on a Chip, 2004. 4(5): p. 516-522.

130. Martanto, W., et al., *Mechanism of fluid infusion during microneedle insertion and retraction.* Journal of Controlled Release, 2006. 112(3): p. 357-361.

131. Elias, P.M., *The stratum corneum as an organ of protection: old and new concepts.* Curr Probl Dermatol, 1989. 18: p. 10-21.

132. Schmidt, R.F. and G. Thews, *Human physiology*. 2nd completely rev. ed. 1989, Berlin ; New York: Springer-Verlag. xviii, 825 p.

133. Yang, M. and J.D. Zahn, *Microneedle Insertion Force Reduction Using Vibratory Actuation.* Biomedical Microdevices, 2004. 6(3): p. 177-182.

134. Sebastien Henry, D.V.M., Mark G. Allen, Mark R. Prausnitz,, *Microfabricated microneedles: A novel approach to transdermal drug delivery.* Journal of Pharmaceutical Sciences, 1998. 87(8): p. 922-925.

135. Hillis, D.M., C. Moritz, and B.K. Mable, *Molecular systematics*. 2nd ed. 1996, Sunderland, Mass.: Sinauer Associates. p. 231.

136. Khanna, P., et al., *Use of nanocrystalline diamond for microfluidic lab-on-a-chip.* Diamond and Related Materials, 2006. 15(11-12): p. 2073-2077.

137. Kulisch, W., et al., *Mechanical properties of nanocrystalline diamond/amorphous carbon composite films prepared by microwave plasma chemical vapour deposition.* Diamond & Related Materials, 2004. 13(11-12): p. 1997-2002.

138. Chambers, A.A., *Selectivity/etch rate trade-offs in deep and high A/R oxide etching.* Solid State Technology, 2005. 48(2).

139. Hwang, G.S. and K.P. Giapis, *Pattern-dependent charging in plasmas.* Ieee Transactions on Plasma Science, 1999. 27(1): p. 102-103.

140. Mise, N., et al. *Pattern-size effect on electron shading*. in *Plasma Process-Induced Damage, 2000 5th International Symposium on*. 2000.

141. Kamata, T. and H. Arimoto, *Charge build-up in Si-processing plasma caused by electron shading effect.* Journal of Applied Physics, 1996. 80(5): p. 2637-2642.

142. Dixit, P. and J. Miao, *Effect of Clamping Ring Materials and Chuck Temperature on the Formation of Silicon Nanograss in Deep RIE.* Journal of The Electrochemical Society, 2006. 153(8): p. G771-G777.

143. Karola Richter, C.K., Johann-Wolfgang Bartha,, *Micro-Patterned Silicon Surfaces for Biomedical Devices.* Plasma Processes and Polymers, 2007. 4(S1): p. S411-S415.

144. Pereira, B.P., P.W. Lucas, and T. SweeHin, *Ranking the fracture toughness of thin mammalian soft tissues using the scissors cutting test.* Journal of Biomechanics, 1997. 30(1): p. 91-94.

145. Purslow, P.P., *Measurement of the Fracture-Toughness of Extensible Connective Tissues.* Journal of Materials Science, 1983. 18(12): p. 3591-3598.

146. Plummer, J.D., M.D. Deal, and P.B. Griffin, *Silicon VLSI technology : fundamentals, practice, and modeling*. Prentice Hall electronics and VLSI series. 2000, Upper Saddle River, NJ: Prentice Hall. p. 333-335.

APPENDICES

Appendix A: Microneedle Gauge Sizes

33 gauge: Inner Diameter - 100 micron; Outer Diameter 200 micron

34 gauge: Inner Diameter - 85 micron; Outer Diameter 160 micron

35 gauge: Inner Diameter - 65 micron; Outer Diameter 130 micron

36 gauge: Inner Diameter - 30 micron; Outer Diameter 100 micron

Appendix B: Photolithography Recipe for AZ4620

Step 1: Spin HMDS at 3500 rpm for 30 seconds.

Step 2: Spin photoresist AZ4620 at 500 rpm for 10 seconds followed by 2500 rpm for 60 seconds.

Step 3: Soft bake in oven at 90°C for 20 minutes.

Step 4: Leave wafer at ambient temperature for 1 hour to rehydrate resist.

Step 5: Expose in Karl-Suss aligner for 55 seconds at 25 mW/cm^2 intensity.

Step 6: Develop in 1:1 AZ400K:H_2O for 4 minutes.

Step 7: Hard bake in oven at 90°C for 20 minutes.

Result: Photoresist thickness obtained is approximately 6.6 to 7 micron.

Appendix C: Silicon DRIE Recipe

Etch step gases	SF_6 and 300 sccm with 3 second cycle.
Passivation step gases	C_4F_8 at 200 sccm with 1.4 second cycle, and O_2 at 20 sccm with 1.4 seconds cycle
Pressure:	5.25×10^{-1} mTorr
Source generator power:	2400 W
Substrate holder power:	Used in pulsed mode High cycle at 100 W for 25 millisecond Low cycle at 0 W for 75 millisecond
Substrate holder He pressure:	9.75×10^{-3} mTorr
Bias Voltage:	-185 V (negative)

ABOUT THE AUTHOR

Puneet Khanna received his BE degree in Electronics Engineering from Nagpur University, India in 2001 and MS in Electrical Engineering from University of South Florida (USF), Tampa, FL in 2004 with specialization in microelectronics. He is currently pursuing a PhD in Electrical Engineering at USF with specialization in Bio-MEMS. As part of the Bio-MEMS and Microsystems Laboratory and Nanomaterials and Nanomanufacturing Research Center, his research includes fabrication of microneedles and lab-on-a-chip devices.